Università degli Studi di Pavia

Facoltà di Ingegneria
Dipartimento di Ingegneria Industriale e dell'Informazione

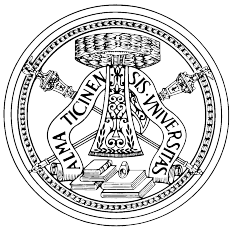

Doctoral Thesis in Microelectronics
XXXI Ciclo

A SAW-Less FDD Receiver with TX Leakage Cancellation in Receive and Transmit Bands

Supervisor:
Chiar.mo Prof. Danilo Manstretta
Coordinator:
Chiar.mo Prof. Guido Torelli

Author:
Daniele Montanari

A thesis submitted in fulfillment of the requirements for the degree of Doctor of Philosophy.

January 2019

Declaration of Authorship

I, Daniele MONTANARI, declare that this thesis titled, 'A SAW-Less FDD Receiver with TX Leakage Cancellation in Receive and Transmit Bands' and the work presented in it are my own. I confirm that:

- This work was done wholly or mainly while in candidature for a research degree at this University.
- Where any part of this thesis has previously been submitted for a degree or any other qualification at this University or any other institution, this has been clearly stated.
- Where I have consulted the published work of others, this is always clearly attributed.
- Where I have quoted from the work of others, the source is always given. With the exception of such quotations, this thesis is entirely my own work.
- I have acknowledged all main sources of help.
- Where the thesis is based on work done by myself jointly with others, I have made clear exactly what was done by others and what I have contributed myself.

Signed: _____

Date: _____

UNIVERSITÀ DEGLI STUDI DI PAVIA

Abstract

Facoltà di Ingegneria
Dipartimento di Ingegneria Industriale e dell'Informazione

Doctor of Philosophy

A SAW-Less FDD Receiver with TX Leakage Cancellation in Receive and Transmit Bands

by Daniele MONTANARI

In modern mobile communication standards such as 4G LTE, the implementation of multi-band transceivers as well as the increasing channel bandwidth are the main need for high data-rate communications. However, close proximity of the Receiving (RX) and Transmitting (TX) antennas causes part of the transmitted signal to be coupled to the RX, bringing it to desensitization. To reduce this effect, Self-Interference Cancellation (SIC) techniques are a promising solution that avoids the use of bulky, costly and not tunable SAW-filters. However, antenna coupling group delay in the order of 2-3 ns limits the cancellation bandwidth of conventional SIC thus making it difficult to ensure good isolation over both TX and RX bands. In this thesis, a diversity receiver with SI cancellation over both bands is presented: a highly linear receiver is aided by an RF SIC that reduces the main TX signal power at the RX input; an auxiliary path (AUX) implements a notch filter in the TX band followed by a digital equalizer whose output is employed to reduce the TX noise leakage in the RX band. The diversity and auxiliary receivers were fabricated in 28 nm TMSC CMOS technology and operate between 1 and 2 GHz while the equalizer performing the Digital TX-Noise Reduction (DNR) algorithm was implemented on FPGA. The stand-alone RX has a Noise Figure (NF) of 4-5 dB and an out-of-band IIP3 of 18 dBm. Thanks to the SIC, the effective IIP3 is improved up to 25-29 dBm with a NF degradation of only 0.8 dB. Due to its high dynamic range, the AUX is able to reduce the TX noise by more than 29 dB degrading only by 1 dB the RX NF at full TX power (23 dBm).

Contents

List of Figures

List of Tables

A mio padre.

Chapter 1

Introduction

Mobile communications are evolving toward the new generation of wireless standard (5G) demanding an increased data rate, greater flexibility and lower cost. The current fourth-generation (4G) Long Term Evolution (LTE) standard has already introduced lots of novelties with respect to the previous one (3G) such as different modulation formats, multiple antennas for both transmission and reception, flexible channel bandwidths and several operating bands. These requirements open new challenges in the transceivers design pushing the research toward the development of completely new architectures. In this Chapter, the typical mobile communication system is presented highlighting its main drawbacks together with an overview of the different systems proposed in literature.

1.1 4G Mobile Communication Systems

A typical block diagram of a communication system for mobile terminals is shown in Fig.1.1 where multiple transceivers (TRXs) as well as diversity receivers (RXs) are integrated on the same chip. While the main transmitter (TX) and main receiver share the same antenna through an off-chip duplexer, each diversity RX has a dedicated one. The use of multiple antennas in mobile devices was introduced to increase the capacity of the wireless communication channel [1] evolving the simple Single-Input Single-Output (SISO) system made of a single transceiver into the more complex Multiple-Input Multiple Output (MIMO) system. Known as antenna or spatial diversity, this approach is a way to add redundancy to the transmission or reception of the signal, improving the performance of the interference-limited wireless communication systems. Different combination of transmitting and receiving antennas are compatible with the 4G standard up to a maximum of 8 antennas (4x4 MIMO system).

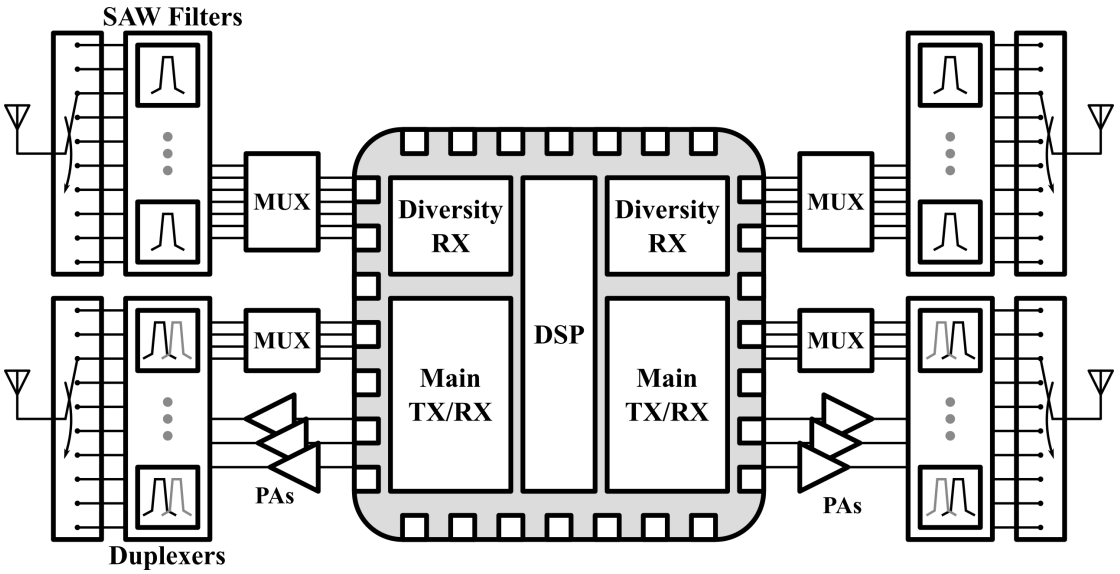

FIGURE 1.1: Block diagram of a typical mobile communication system with SAW filters and duplexers.

The 4G LTE wireless communication standard [2] sets stringent requirements on the transmitter out-of-band (OOB) emissions and on the capability of the receiver to withstand strong OOB blockers. For this reason, an off-chip Surface Acoustic Wave (SAW)-based duplexer is typically used in the main transmission/reception path, providing more than 45 dB of OOB filtering. In a similar way, each diversity RX has a SAW filter in front of it. The lack of tunability of these off-chip components forces the use of one of them for each band that has to be covered and hence switches and multiplexer are used to select the right filter/duplexer. Due to their bulky structure, the large number of off-chip components increases the complexity of the signal routing and the area of the system as well as the overall cost. All these drawbacks are in contrast to the demand of the new generations of mobile communication standards asking for high flexibility and low cost. For this reason, the research is looking forward different kind of solutions to replace these off-chip components facing all the problems related to the lack of filtering in front of the transceivers.

1.2 The SAW-Less Challenge

Two different possibilities for point-to-point communication are available in 4G systems: the Time-Division Duplexing (TDD) and the Frequency-Division Duplexing (FDD). In the former, the transmission and the reception happen on different time interval over the same band. On the opposite, in FDD, different bands are used for the concurrently TX and RX functioning. While reducing the system complexity and cost, removing the

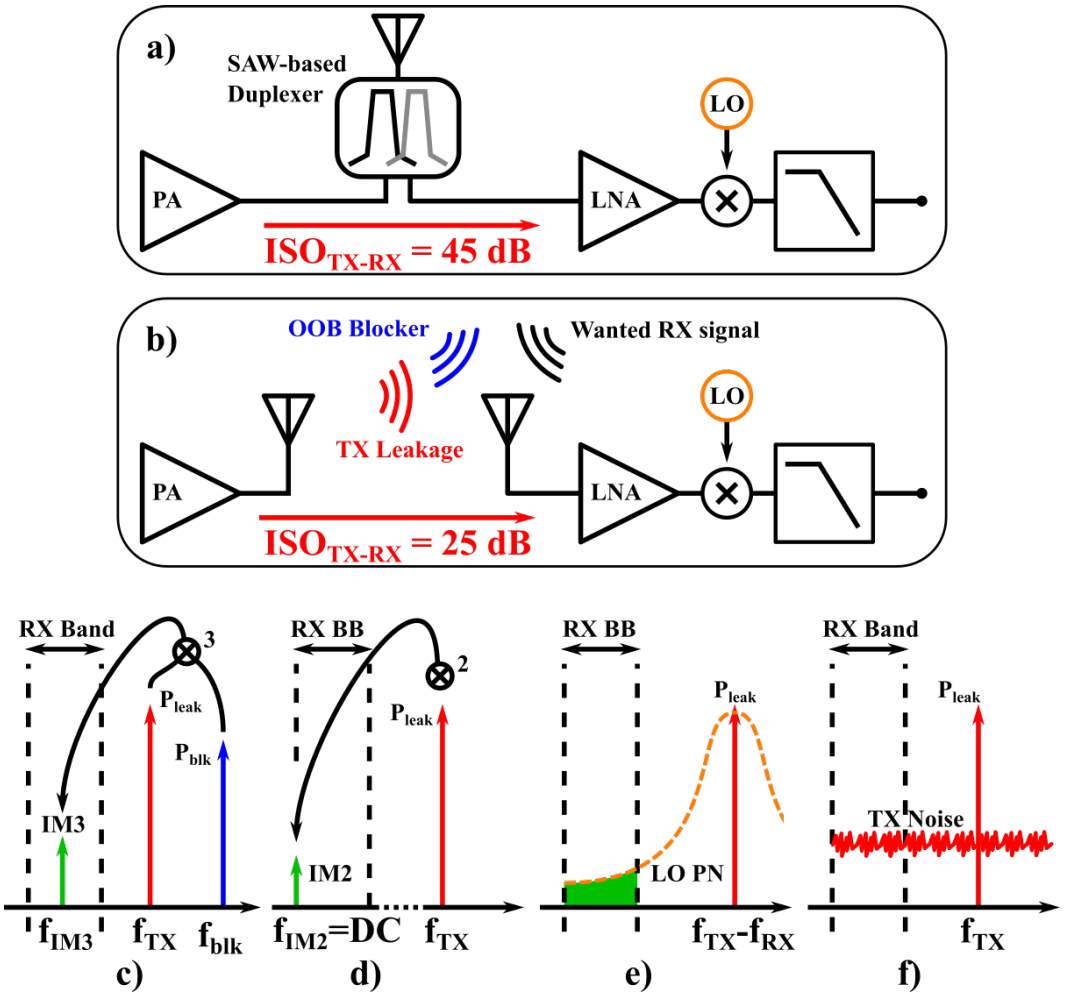

FIGURE 1.2: Simplified block diagram of the self-interference mechanism with (a) and without (b) SAW-based duplexer. The RX sensitivity is degraded through c) 3^{rd} order intermodulation of the TX leakage with OOB blocker, d) 2^{nd} order itermodulation, e) reciprocal mixing and f) TX noise that directly falls into the RX band.

SAW-filters means that the TX and the RX have to work with 45 dB less of OOB filtering. The lack of filtering is particularly critical in the FDD scenario because, due to the close proximity of the two antennas in a mobile platform, part of the transmitted signal can be coupled to the receiver (Fig.1.2b). While the TX-RX coupling is strongly mitigated with SAW-based duplexer and filters (Fig.1.2a), typically only a poor isolation is provided from the distance between the antennas [1]. Assuming for sake of simplicity that the TX output consists of a strong Continuous Wave (CW) signal and of a broadband noise component, the TX leakage degrades the RX performance through:

- 3^{rd} order itermodulation with OOB blocker (Fig.1.2c);
- 2^{nd} order itermodulation (Fig.1.2d);

[1]Notice that integrated solutions that replace the off-chip duplexers in single-antenna systems suffer of the same poor isolation problem.

- reciprocal mixing (Fig.1.2e);
- TX broadband noise (Fig.1.2f).

To understand the toughness of the design of an FDD SAW-less system, the receiver linearity and noise requirements for a 4G mobile communication systems are computed in this section.

1.2.1 Receiver Sensitivity and Noise Figure

The minimum signal that a receiver is able to detect with a given Signal-to-Noise Ratio (SNR) is called sensitivity and is defined as [3]:

$$P_{sens} = -174[dBm/Hz] + \mathrm{NF} + 10\log_{10} B + \mathrm{SNR} \tag{1.1}$$

where NF is the receiver noise figure and B is the bandwidth. In the 4G standard, the REFerence SENSitivity (REFSENS) for an LTE-20 MHz bandwidth is between -94 and -90.5 dBm. These values has to be referred to a dual antenna system (i.e. main receiver plus one diversity) when a QPSK signal with a 1/3-rate code[2] is received. The SNR in this condition is -1 dB but usually an extra Implementation Margin (IM) is used to take into account any degradation from the digital processing of the signal [4]. The IM mainly depends on the modulation format and for a QPSK signal is 2.5 dB. Therefore, the effective SNR required is:

$$\mathrm{SNR}_{tot,QPSK} = \mathrm{SNR}_{QPSK} + IM = -1 + 2.5 = 1.5\,dB \tag{1.2}$$

and the equation Eq.(1.1) for the 4G standard becomes :

$$REFSENS = -174[dBm/Hz] + \mathrm{NF}_{RX} + 10\log_{10} B + \mathrm{SNR}_{tot,QPSK} - 3\,[dB] \tag{1.3}$$

where the NF_{RX} is the noise figure of each receiver and -3 is the diversity gain. From Eq.(1.3), the maximum receiver NF_{RX} is between 8.5 and 12 dB. Even if state-of-the-art receivers achieve typically lower noise figure, gain compression, reciprocal mixing and TX noise leakage can degrade the receiver NF.

1.2.2 Receiver Linearity

The blocking test defines the capability of the receiver to receive a wanted signal achieving $\geq 95\%$ of the maximum throughput (of the reference measurement channel [2]) at

[2]The code rate defines the ratio between the effective amount of information and the redundancy used for coding.

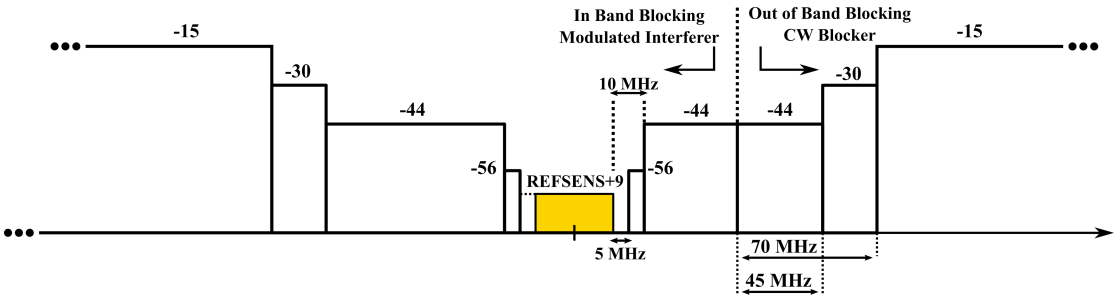

FIGURE 1.3: 4G LTE blocking profile [2].

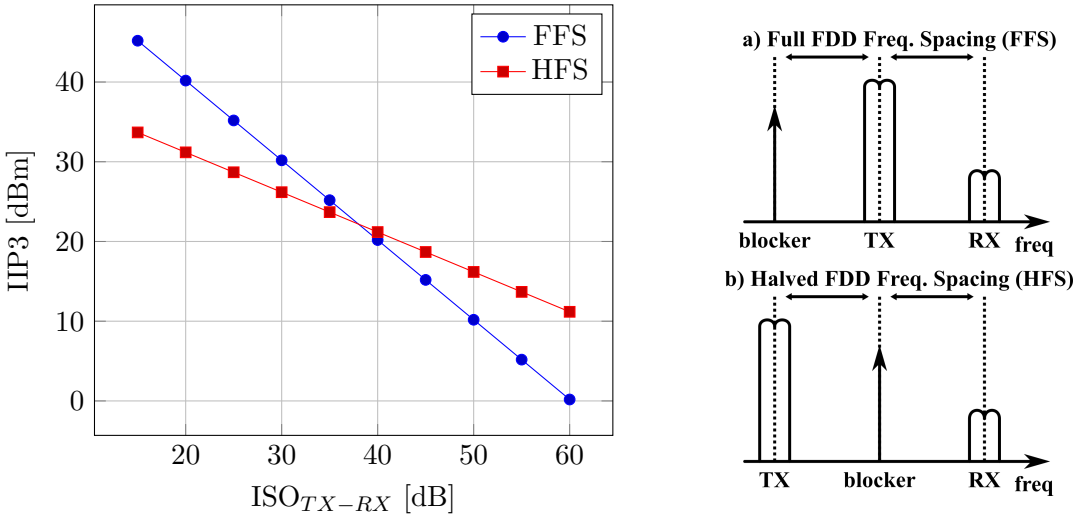

FIGURE 1.4: Required IIP3 versus TX-RX isolation level in FFS (a) and HFS (b) scenarios.

its assigned channel frequency in the presence of an interfering signal (i.e. blocker). The blocker power is defined as a function of the frequency spacing starting from -56 dBm at 5 MHz distance and reaching up to -15 dBm when the blocker falls 70 MHz far from the band edge (Fig.1.3). For the OOB blocking test, the wanted signal level is 9 dB above the REFSENS and during the test, the transmitter has to deliver an output power of $P_{TX} = 23$ dBm. Defining the isolation between the antennas as ISO [dB], the TX leakage power reaching the RX antenna is:

$$P_{leak}[dBm] = P_{TX}[dBm] - \mathrm{ISO}_{TX-RX}[dB] \tag{1.4}$$

Due to the receiver non-linearities, a Third-order Inter-Modulation product (IM3) will be produced from the inter-modulation between the OOB blocker and the TX leakage as shown in Fig.1.2b (f_{blk} and f_{TX} are the blocker and TX frequencies respectively). Given a certain receiver third-order linearity usually quantified with its Input-referred Third-order Intercept Point (IIP3), the IM3 power can be computed as:

$$\mathrm{IM3}_{FFS} = 2P_{leak} + P_{blk} - 2\mathrm{IIP3} \tag{1.5}$$

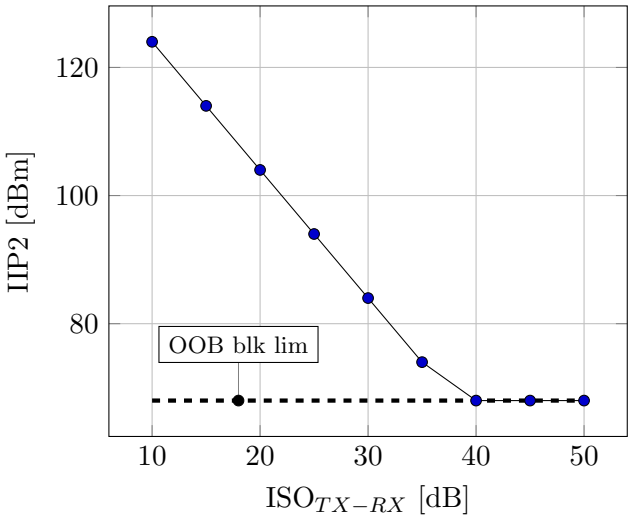

FIGURE 1.5: Required IIP2 value versus TX-RX isolation.

when the IM3 frequency is $f_{\text{IM3,FFS}} = 2f_{TX} - f_{blk}$ (Full Frequency Spacing FFS) and

$$\text{IM3}_{HFS} = 2P_{blk} + P_{leak} - 2\text{IIP3} \tag{1.6}$$

when the IM3 frequency is $f_{\text{IM3,FFS}} = 2f_{blk} - f_{TX}$ (Half Frequency Spacing HFS).

To correctly detect the wanted RX signal that is 9 dB above the reference sensitivity, the IM3 requirement is:

$$IM3_{FFS,HFS} \leq REFSENS + 9 - SNR_{tot,QPKS}. \tag{1.7}$$

In reality, the IM3 product adds up with the RX noise floor that is defined as:

$$N_{floor} = -174[dBm/Hz] + 10\log_{10} B + \text{NF}_{RX}. \tag{1.8}$$

However, since the receiver noise is than 10 dB below the wanted signal level, it can be neglected in Eq.(1.7). Combining Eq.(1.5) and Eq.(1.6) with Eq.(1.7), the IIP3 requirement for the FFS and HFS scenarios can be easily computed. Fig.1.4 shows the required IIP3 as a function of the antenna isolation ISO$_{TX-RX}$ with REFSENS $= -94$ dBm. Notice that the IIP3 requirement decreases by 1 dB for each added dB of isolation in the FFS case, while it decreases by only 0.5dB/1dB in the HFS case. Under reduced ISO$_{TX-RX}$ levels the TX leakage power is higher than the blocker one and the most challenging scenario is the FFS. When $P_{TX} - \text{ISO}_{TX-RX} = P_{blk}$ the two requirements are equal and with strong TX-RX isolation the worst scenario is the HFS one.

The same procedure can be applied to find the required Input-referred Second-Order Intercept Point (IIP2). Any second order non-linearity in the RX creates a DC (and

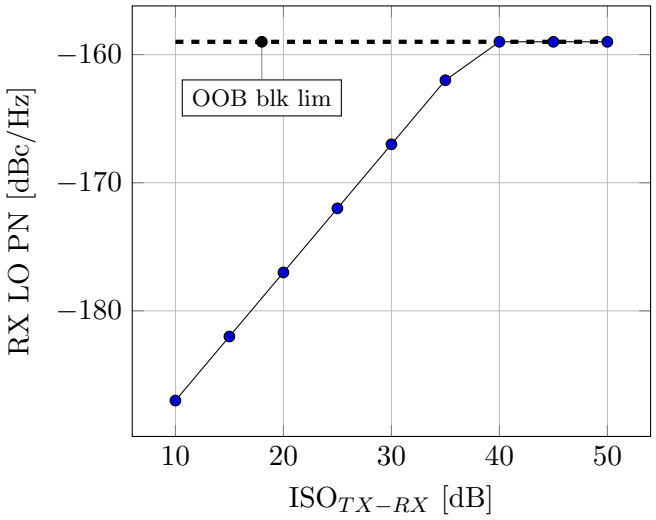

FIGURE 1.6: RX LO phase noise requirement versus TX-RX isolation.

$2f_{TX}$) component that is proportional to the TX leakage power. Even if it falls quite far from the RX band, asymmetries in the mixer or in the LO waveforms can bring part of the Second-order Intermodulation product (IM2) at the baseband input without being frequency translated (Fig.1.2c). To avoid the degradation of the RX signal, at first approximation, the IM2 product must remain below the receiver noise floor, obtaining:

$$\mathrm{IM2}_{DC} \leq N_{therm} = -174[dBm/Hz] + 10\log_{10} B. \tag{1.9}$$

With this result, the required IIP2 can be computed as:

$$IIP2 \geq 2(P_{TX} - \mathrm{ISO}_{TX-RX}) - (\mathrm{IM2}_{DC} + 3) \tag{1.10}$$

where the +3 term is added because it the TX leakage is modelled as a single tone. Fig.1.5 shows the required IIP2 value as a function of the TX-RX isolation: even if IIP2 requirement decreases by 2 dB for each dB of added isolation, reduced ISO_{TX-RX} brings it above 100 dBm. Moreover, when the TX leakage power is below -15 dBm, the IIP2 requirement is set by the OOB blocker and does not decreases as a function of the isolation.

1.2.3 Receiver LO Phase Noise

Another requirement is related to the receiver LO phase noise (Fig.1.2d). The cross modulation between the TX leakage and the noise skirt of the mixer LO brings part of the TX power in the RX band (i.e. reciprocal mixing). Assuming a flat phase noise power spectral density, also in this case, to avoid sensitivity degradation, the cross modulation product must remain below the RX noise floor. Therefore, the LO phase noise LO_{PN}

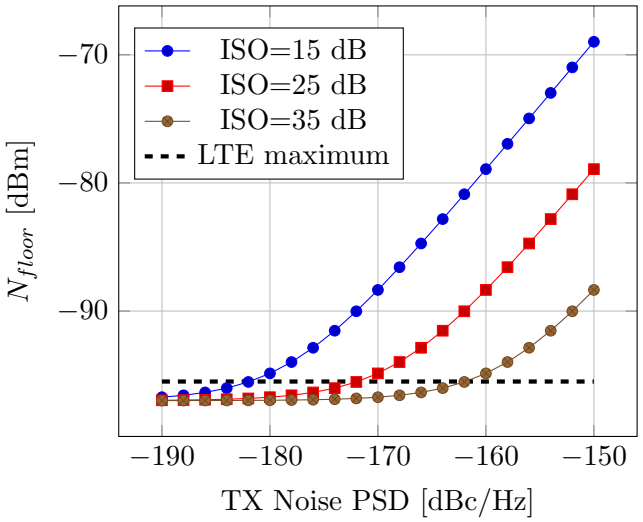

FIGURE 1.7: RX sensitivity versus TX noise in the RX band for different isolation levels with $P_{TX} = 23\,dBm$, B=20 MHz and NF_{RX}=5 dB.

requirement is:

$$LO_{PN} \leq -174[dBm/Hz] - P_{leak}. \tag{1.11}$$

Fig.1.6 shows the PN requirement as a function of the TX-RX isolation level. As in the IIP2 case, when the leakage power is below the strongest OOB blocker one (-15 dBm), the requirement is no more relaxed enhancing ISO_{TX-RX}.

1.2.4 Transmitter OOB Noise

While the other three requirements are related to the RX performance such as linearity and local oscillator (LO) phase noise, the amount of TX noise leakage depends only on the coupling between the antennas and on the transmitter performance. The TX noise leakage that falls in the RX band is directly added to the RX own noise increasing the RX noise floor (Fig.1.2e). Fig.1.7 shows the RX noise floor versus the TX broadband noise value for different isolation levels. The dashed line is the maximum allowed by the LTE standard with REFSENS=-94 dBm. As expected, the degradation is a strong function of the magnitude of the coupling: to fulfill the LTE requirement with an ISO between 15 and 35 dB the specs moves from -155 to -176 dBc/Hz. With a reasonable ISO level of 25 dB, to avoid RX sensitivity degradation, -170 dBc/Hz are required.

1.2.5 System Requirements Summary

Table 1.1 reports the summary of the SAW-less transceiver specifications computed in this section for different isolation levels. From these results, it is evident that removing

$\mathbf{ISO_{TX-RX}}$	**FFS IIP3**	**IIP2**	**RX LO PN**	**TX OOB Noise**
15 dB	44 dBm	114 dBm	-182 dBc/Hz	<-180 dBc/Hz
25 dB	34 dBm	94 dBm	-172 dBc/Hz	<-170 dBc/Hz
35 dB	24 dBm	74 dBm	-162 dBc/Hz	<-162 dBc/Hz

TABLE 1.1: SAW-Less transceiver specifications for different ISO_{TX-RX} levels.

the SAW-filter from a traditional architecture makes the system requirements hard to be fulfilled. This is mainly due to the strong coupling between the transmitter and the receiver (main or diversity) and for this reason several solutions have been proposed in literature to address this problem.

1.3 State of the Art

During years, several works were published about the self-interference problem in FDD wireless systems. In this section, they are divided into different categories:

- RF channel selection;
- Self-interference cancellers;
- Hybrid transformers.

Finally, another section is dedicated to the transmitter noise shaping where the authors tackles the problem of the TX noise in the RX band looking at the transmitter side.

1.3.1 RF Channel Selection

The frequency spacing in FDD systems can be exploited to implement RF filtering at the RX input improving the receiver linearity and compression. N-Path filters are a promising solution [6–8] since they are linear, tunable and highly selective (i.e high quality factor)[3]. In [6], the frequency response of two different N-Path filter is exploited to provide channel selectivity and TX leakage filtering: a band-pass and a band-stop filters are tuned at the receiver and transmitter frequencies respectively, enabling a maximum rejection of 41 dB, close to the one provided by an off-chip SAW (i.e. 45 dB). High linearity (OOB IIP3 is 29 dBm) and compression point (>10 dBm) are the main features of this implementation. However, to reach these incredible values the power consumption raises dramatically up to 400 mW mainly because of the power dissipated by the dividers that drive the N-Path switches. Moreover, since the switches are directly

[3]The theory and analysis of the N-Path filters is reported in Appendix B.

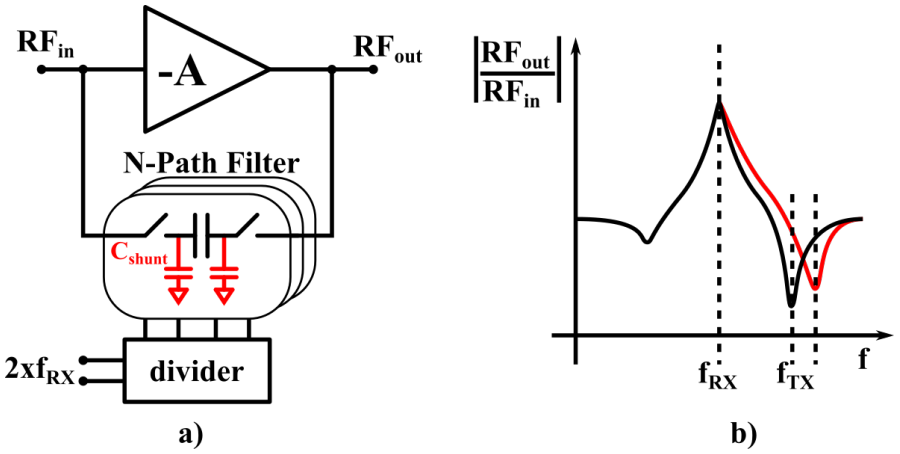

FIGURE 1.8: Channel selectivity is achieved through an N-Path filter in the feedback loop (a). Frequency response of the proposed implementation (b): the additional C_{shunt} adds rejection at a programmable frequency offset [5] (©2016 IEEE).

connected to the antenna port, LO leakage is in the order of -55 dBm, which is too high for the 4G LTE standard.

Another option is to embed the N-Path filter into the receiver front end [5, 9–14]. In [5] the authors present a Low Noise Transconductance Amplifier (LNTA) made of a main amplifier with a feedback network implemented through N-Path filters, as shown in Fig.1.8. The feedback path shows a high impedance at the LO frequency while it sharply decreases far from it. This creates a band-pass shape at the input of the receiver enabling the reception of a small signal in presence of large OOB blocker and TX leakage. Moreover, to increase the rejection at small frequency offset, an additional shunt capacitor is used increasing the OOB IIP3 of the receiver up to 36 dBm and the 1 dB compression point with a 100 MHz spaced blocker to 17 dBm. Also in this case, the power consumption is a problem: more than 200 mW are dissipated by the LO dividers.

Even if these are promising solutions, they does not solve all the problem related to a SAW-less implementation since the TX noise in the RX band cannot be reduced by means of filtering on the receiver side.

1.3.2 Self-Interference Canceller

The knowledge of the self-interference signal enables a completely different approach that relies on cancellation-based architectures. The basic idea is that the TX signal can be sensed at the transmitter output and injected at the receiver input attenuated and phase shifted in such a way that it cancels out with the one coming from the coupling between the antennas (Fig.1.9). The block performing the cancellation is typically called Self-Interference Canceller (SIC) and different topologies have been proposed.

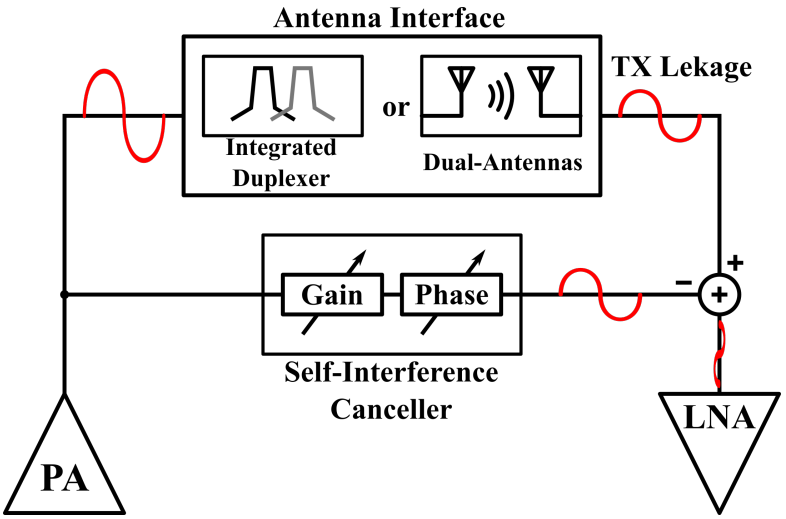

FIGURE 1.9: Simplified SIC block diagram where the SIC injects a copy of the TX signal at the RX input. With proper attenuation and phase shift, the copy cancels out the TX leakage.

Variable attenuation and phase shift can be provided through a vector modulator [15–17]. In [16], two quadrature versions of the TX signal are generated through a poli-phase filter and processed through two variable gain amplifiers independently tunable. The two signal are then added up before a buffer injects them at the RX input. While providing 20 dB of TX leakage cancellation, the active circuitry limits the power that can be handled by the canceller meaning that this solution can be implemented only in system where TX-RX coupling is reduced. This drawback is solved using passive topologies in which only passive components and NMOS switches are present. In [18], the authors propose to use multiple parallel paths to achieve wide cancellation bandwidth needed for modern mobile standards. Implemented through N-Path filters, the proposed solution is able to achieve 25 MHz of SIC bandwidth with a maximum TX leakage at the RX input of -4 dBm. The main difference between the two architectures is the shape of the SIC frequency response: while the vector modulator has a flat response, the second one shows a band-pass shape. In Chapter 2, a comparison between them is proposed taking into account the effects of a real antenna interface.

Different approaches were proposed in [19–21] where the SIC are implemented through RF DAC or analog FIR filters. In the former, the DAC injects a copy of the TX leakage at the RX input. Moreover, using the TX LO to drive the DAC, also the TX close in phase noise is reduced. In [20, 21] an analog FIR filter process the TX copy before the cancellation at the RX input. However, both implementations suffer from the group delay introduced in the TX-RX coupling that degrades significantly the system performance.

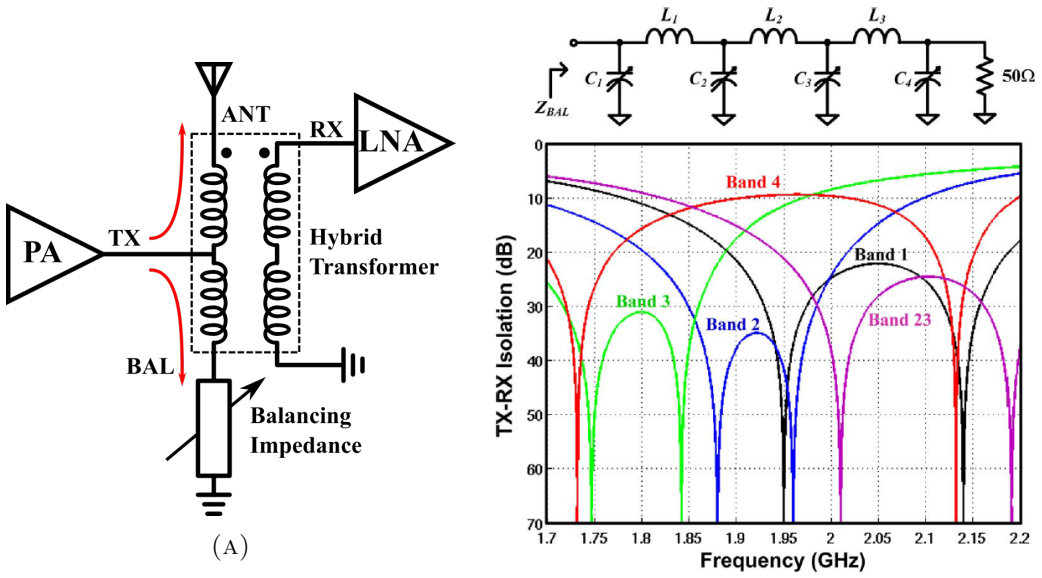

FIGURE 1.10: a) Hybrid transformed used as an integrated duplexer and b) dual-notch HT proposed in [22] (©2014 IEEE).

1.3.3 Hybrid Transformer

A different way to approach this problem is replacing the external duplexers with passive on-chip solutions such as the hybrid transformer (HT) [22–26]. As shown in Fig.1.10, the HT is a four ports network that provides good isolation between the TX and RX ports if the balancing impedance match the antenna one. In this condition, the signal coming from the Power Amplifier (PA) is equally divided by the ANT and BAL ports and no signal is coupled to the RX side. In an ideal 50 Ω antenna environment, the balancing impedance would be a simple 50 Ω resistor. However, due to complex antenna impedance different balancing networks have been proposed in literature. In [24], a parallel RC network is used; the main drawback of this solution is the limited isolation bandwidth because the impedance of the network is matched with the antenna one only at a single frequency and the isolation degrades rapidly in frequency if a real antenna is used[4]. However, the simplicity of the network allowed to implement an efficient tuning algorithm to select the right RC combination [27]. In [22] the authors implemented a complex balancing impedance made of an LC ladder achieving a good isolation over both TX and RX bands at the cost of high complexity, large area and difficult tuning.

[4]This aspect is deeply analyzed in Chapter 2.

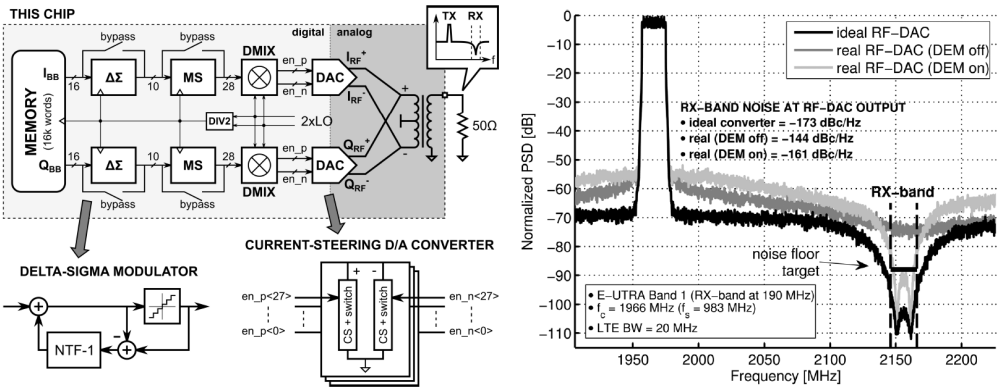

(A) (B)

FIGURE 1.11: a) Block diagram of the all-digital TX with TX noise shaping and b) RF spectra of the TX output signal [29] (©2014 IEEE).

1.3.4 TX Noise Shaping

The development of digital intensive TX architectures has always had to face the problem of OOB spurious emissions (i.e. TX broadband noise) that are mostly determine by the RF-DAC quantization noise. While an Effective Number of Bit (ENOB) equal to 10 is sufficient to fulfill the 3G/4G requirements, it is not enough to avoid the RX sensitivity degradation due to the self-interference mechanism. For this reason, in [28–30] the authors proposed different techniques to reduce the TX OOB noise in the RX band. In particular, in [28] through a $\Sigma\Delta$ modulator and mismatch shaping techniques the TX noise in the RX band is shaped and it is reduced down to -161 dBc/Hz. Even if it is an excellent value, this value could be not enough for high transmitter power as shown in Fig.1.7.

1.4 Thesis Structure

In this chapter, the typical 4G mobile platform has been presented and the challenges behind the SAW-less implementation have been described. A literature overview presents the architectures that have been proposed during years. However, none of them fully solve all the challenges related to a SAW-less implementation. In this thesis, a diversity receiver[5] with self-interference cancellation over TX and RX bands that addresses the SAW-less requirements is presented. The dual-cancellation path is needed because of the limited cancellation bandwidth of integrated canceller topologies. This aspect is deeply analyzed in Chapter 2, where the antenna interface is studied through simulations and

[5]The reference to the diversity path is related to the fact that the proposed architecture is tailored to dual-antenna systems.

measurements. In Chapter 3 the proposed system architecture and the circuit implementation are described while in Chapter 4 measurement results are reported. Finally, the conclusions of this work are reported in Chapter 5.

Chapter 2

Antenna Coupling and Self-Interference Cancellation

In Chapter 1, the typical mobile communication system has been introduced. The interface with the external environment determines the amount and the frequency behavior of the TX-RX coupling. In this chapter, the antenna coupling is analyzed and experimentally measured using a couple of antennas that were designed and manufactured for this purpose. The cancellation bandwidth is then computed considering different self-interference cancellers topologies. The reported data were published in [31] and the copyright belongs entirely to IEEE (©2016 IEEE).

2.1 TX-RX Antenna Coupling

To investigate the antenna coupling in a real working condition, two Planar Inverted F-Antennas (PIFAs) [32] were designed and manufactured. This kind of antenna was chosen because of its interesting properties that make it suitable for modern mobile wireless systems. In particular, due to its low cost, low profile, small size, easy fabrication and low specific absorption rate (SAR), it has been intensively used in different frequency bands such as GSM 850,900, UMTS and 4G LTE. While the operating principle is the same of the half-wavelength resonant patch antenna, a reduction in size is obtained short-circuiting one side of the patch to the ground with a pin. The PIFA drawbacks are a low gain and a reduced bandwidth with respect to the half-wavelength resonant patch antenna.

The designed antenna is shown in Fig.2.1. The substrate is a 0.8 mm thick FR-4 with a single copper layer and its nominal permittivity is 4.4. The resonant frequency of the

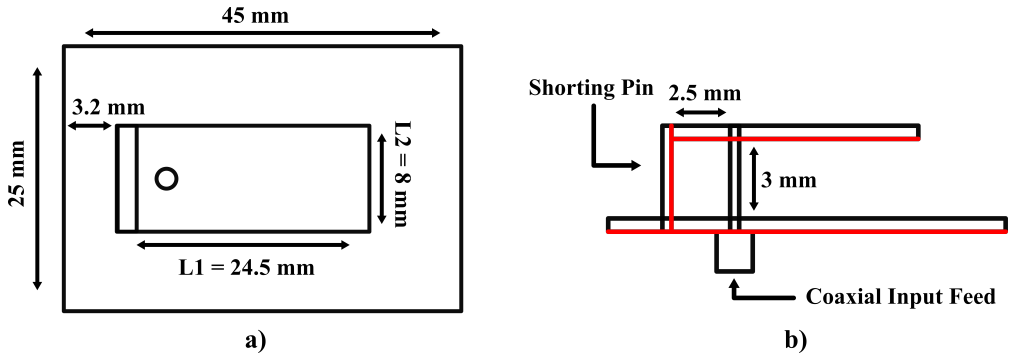

FIGURE 2.1: PIFA design: a) top view; b) side view.

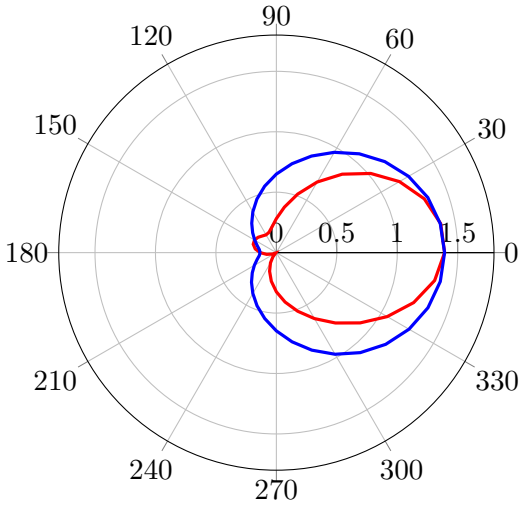

FIGURE 2.2: Radiation pattern for $\varphi = 0°$ (red line) and for $\varphi = 90°$ (blue line).

antenna was chosen to be 2.45 GHz and by designing the shorting pin as wide as L2, the resonance is defined by the width of the patch antenna. While the length defines the resonance, the height is designed as 3 mm to obtain a 100 MHz bandwidth. To feed the signal, a coaxial cable is used and its position with respect to the shorting pin was selected to obtain the right 50 Ohm input matching. Simulations were performed through Ansys Electronic Desktop (HFSS). Fig.2.2 shows the simulated radiation pattern of the designed antenna having a maximum gain of 1.4 dB while the simulated antenna S11 parameter is shown in Fig.2.4.

2.1.1 Dual-Antenna Configuration

In a typical LTE mobile platform, the main and diversity antennas are located one near to each other spaced only few centimeters, meaning that they are in their respective near field region. For this reason, a strong coupling between them is present and the transmitted signal from the main antenna can be sensed from the diversity one. As can

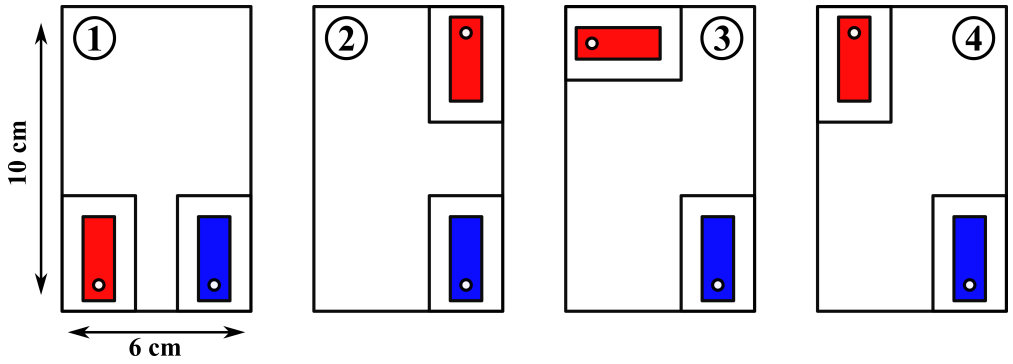

FIGURE 2.3: Dual-antenna configurations: dispositions from 1 to 4

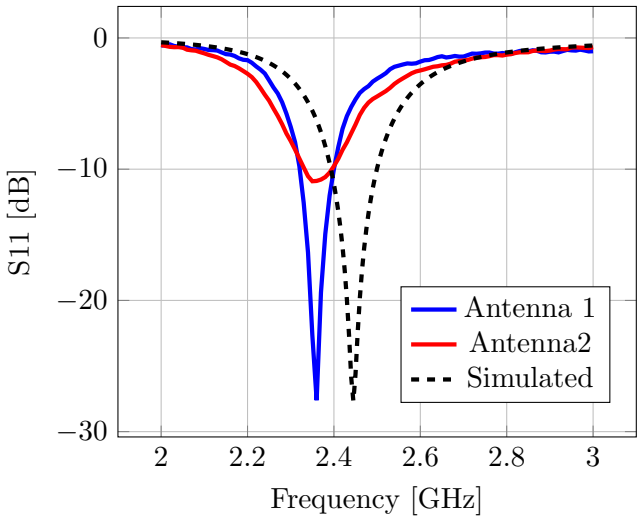

FIGURE 2.4: Simulated and measured s11 parameters of the two antenna prototypes.

be intuitively understood, the coupling is a strong function of the board and antenna design, of the external environment and of the relative position of the two antennas. To evaluate the antenna coupling in realistic conditions, a platform sized 6 cm by 10 cm emulating a typical smartphone was considered for simulations and measurements with four different antenna dispositions were done. Fig.2.3 shows that the first antenna (main antenna) was kept in the lower right corner while the second one (diversity antenna) was moved in all the other corners parallel to the main one (disposition 1,2,4) or rotated by 90° (disposition 3). In all cases, no particular counter measurement was taken in order to reduce the coupling. Simulations performed through HFSS software show that the S21 is maximized near the antenna resonant frequency and goes from -19 dB (disposition 1) to -26 dB (disposition 4). Simulation results were validated through measurements as reported in the next section.

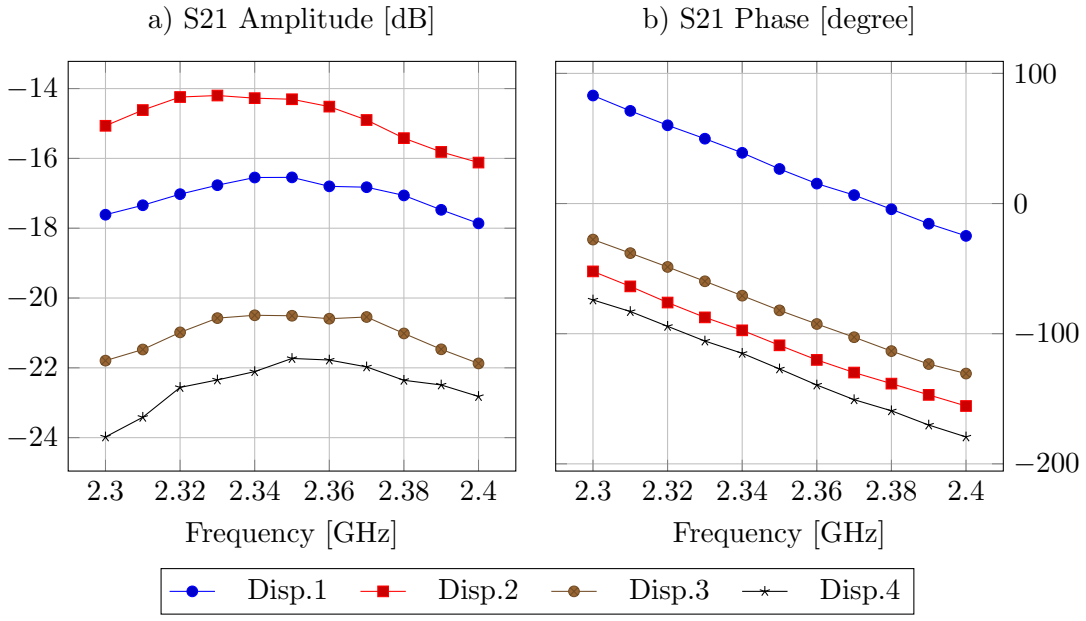

FIGURE 2.5: Measured antenna coupling amplitude (a) and phase (b) vs frequency for different placements.

2.1.2 Measurement Results

The two manufactured antennas were first characterized one by one to verify their functioning. Measured S11 is reported in Fig.2.4: while the first antenna shows a good matching around 2.345 GHz, the other one has a smaller resistive input impedance mainly due to imperfections during the manufacturing process. With respect to the simulations, in both cases, a small reduction in the resonant frequency is present due to the variation of the substrate permittivity. The bandwidth is almost equal for both of them and it is 100 MHz. In Fig.2.5 the S21 amplitude and phase are reported. Measurement results are in good agreement with the simulations and show that the magnitude of the coupling varies between -14 dB and -24 dB and it is almost flat (2 dB maximum variation) over 100 MHz bandwidth. Another important result is that the phase varies linearly over the bandwidth and the group delay (GD) is almost constant (3 ns with 200 ps of maximum variation) in the four placements as shown in Fig.2.6.

2.2 Self-Interference Cancellation

A self-interference canceller (SIC) is a circuit that injects a copy of the TX output signal at the input of the RX. Providing the proper attenuation and phase shift, the copy recombines destructively with the TX leakage, reducing the amount of self-interference. Several SIC topologies have been proposed in literature and here two main categories are discussed:

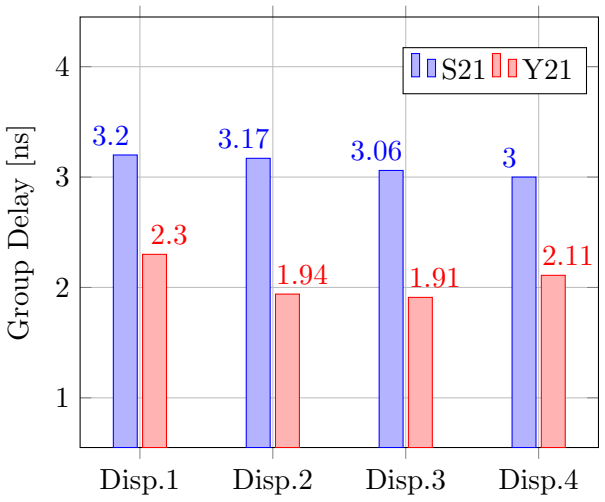

FIGURE 2.6: Antenna coupling group delay.

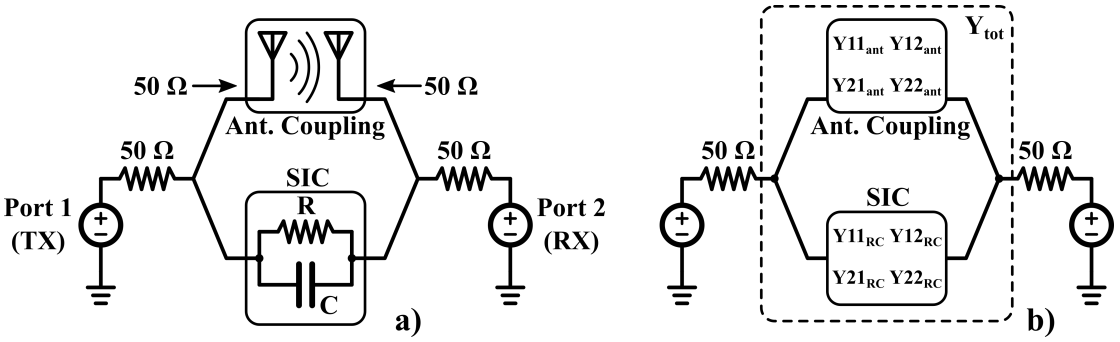

FIGURE 2.7: a) Simplified TX-RX interface schematic and b) its matrix representation.

- **broadband cancellers**: magnitude and phase are constant over frequency;
- **narrowband cancellers**: magnitude and phase change over frequency.

In this section the measured antenna coupling (Disp.4) is combined with an ideal SIC frequency responses to evaluate the cancellation bandwidth through Matlab and Spectre simulations.

2.2.1 Broadband Canceller

One of the easiest way to perform self-interference cancellation is through a simple canceler that provides constant attenuation and phase shift over a wide (w.r.t. the band of interest) frequency range. A passive RC parallel network can be used for the purpose: the resistance (R) and capacitance (C) can be sized to obtain the right attenuation and phase shift. To evaluate the SIC performance, the schematic shown in Fig.2.7a is simulated in Cadence/Spectre environment: the canceller is connected in parallel to a

n-port block containing the measured S-parameters of the antenna coupling (Disp.4); to simplify the computation, both TX and RX were modeled as matched ports and R-C values can be chosen with ideal infinite precision.

Since the input impedance of the canceler is typically much greater than the antenna one [1] and the receiver is matched to 50Ω , the canceler can be considered as a transconductor. The admittance parameters of the RC network ($\mathbf{Y}_{RC}$) can be computed as:

$$\begin{aligned} Y11_{RC} = Y22_{RC} = \frac{1}{R} + i2\pi fC; \\ Y21_{RC} = Y12_{RC} = -Y11_{RC} \end{aligned} \tag{2.1}$$

where f is the frequency. To obtain a perfect cancellation, meaning that no TX signal is coupled to the RX side, the total TX-RX transfer function ($S21_{tot}$) must be zero. Therefore:

$$S21_{tot} = -\frac{2Z_0 Y21_{tot}}{\Delta_Y} = 0 \tag{2.2}$$

where $Z_0 = 50\Omega$, $Y21_{tot}$ is the total admittance and ΔY is the total admittance matrix determinant. This equation leads to the intuitive result:

$$Y21_{tot} = 0. \tag{2.3}$$

As shown in Fig.2.7b, the canceler acts in parallel with the coupling between the antennas and the total transconductance of the system is simply $\mathbf{Y}_{tot} = \mathbf{Y}_{ant} + \mathbf{Y}_{RC}$. Therefore, perfect cancellation is achieved if $Y21_{RC} = -Y21_{ant}$. For a certain frequency f_{canc}, the R and C values can be computed from Eq.(2.1) as:

$$\begin{aligned} R = \frac{1}{real[Y21_{ant}(f_{canc})]} \\ C = \frac{imag[Y21_{ant}(f_{canc})]}{2\pi f_{canc}} \end{aligned} \tag{2.4}$$

As shown in Fig.2.5a, the S21 magnitude is almost flat over 100 MHz bandwidth. This result can lead to the wrong conclusion that the 20 dB cancellation bandwidth using a broadband SIC would be around 100 MHz since both of them have a flat frequency response. However, as it is shown in Fig.2.8, while the SIC Y21 magnitude closely matches the antenna one (only few dB of difference over 100 MHz), the coupling phase rapidly changes (almost 80°) in the same bandwidth leading to a 20 dB cancellation bandwidth of only 14 MHz as reported in Fig.2.9a. This aspect can be intuitively understood considering that the RC SIC is operating a vector summation and its result strongly depends on the matching between the phases. For example, assuming perfect

[1] Only a small fraction of the TX signal is coupled to the RX side, leading to a low transconductance for the canceller and hence a high input impedance.

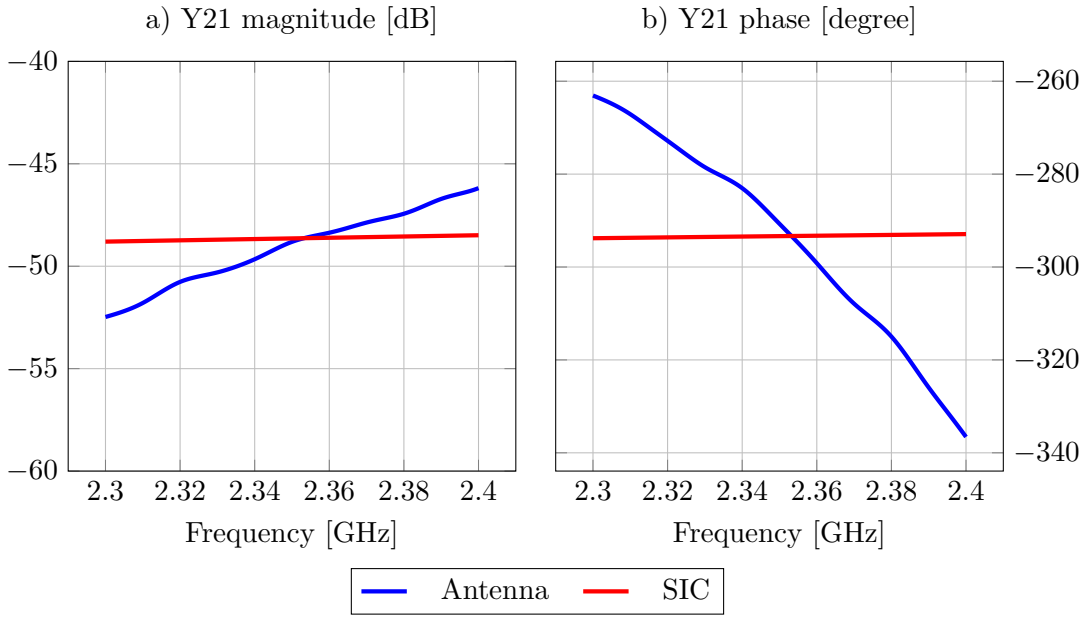

FIGURE 2.8: SIC and antenna coupling Y21 magnitude (a) and phase (b) vs frequency.

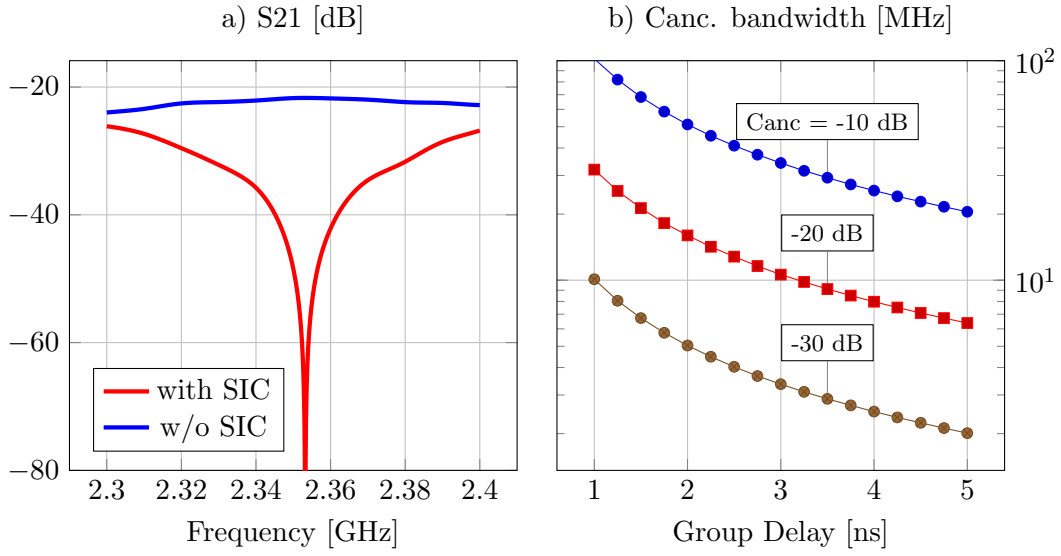

FIGURE 2.9: a) Antenna coupling with and without SIC and b) estimated cancellation bandwidth vs group delay.

matching between the amplitudes, for 20 dB cancellation the maximum allowable phase error is 5.7°. This reasoning can be generalized knowing that the coupling phases varies in a linear way (Fig.2.5b) with a slope that is proportional to the group delay if a small frequency range is considered. The cancellation bandwidth as a function of the group delay for different cancellation levels (10, 20 and 30 dB) is computed assuming no magnitude error. The results are reported in Fig.2.9b: with a group delay of 2 ns, 20 dB cancellation is achieved only over 14 MHz bandwidth which is in good agreement with the simulations results. However, with higher group delay, the cancellation bandwidth

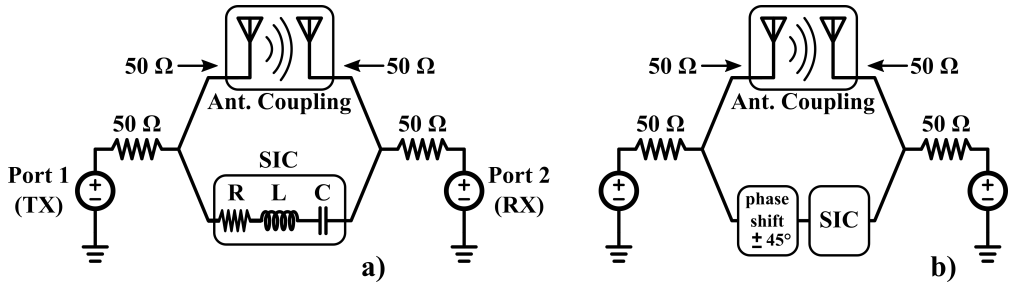

FIGURE 2.10: a) Simplified TX-RX interface schematic with narrowband SIC and b) additional coarse phase shifter.

rapidly decreases reaching only 6 MHz at GD = 5 ns.

2.2.2 Narrowband Canceler

The measurement and simulation results of the previous section suggest that the transfer function of the coupling between the antennas must be taken into account if large cancellation bandwidth has to be achieved. For this reason, the use of a narrowband SIC seems to be the right step toward a bandwidth improvement. A RLC series network is implemented as shown in Fig.2.10a: the SIC admittance is no more flat but has a bandpass shape around the LC resonant frequency. Also in this case, the RLC values can be tuned to obtain perfect cancellation (i.e. no TX-RX coupling) at a certain frequency f_{canc}:

$$\begin{aligned} R &= real\Big[\frac{1}{Y21_{ant}(f_{canc})}\Big] \\ L &= \frac{QR}{2\pi f_{canc}} \\ C &= \frac{-1}{2\pi f_{canc} imag[1/Y21_{ant}(f_{canc})] - (2\pi f_{canc})^2 L} \end{aligned} \tag{2.5}$$

where $Q = 1/2\pi f_{canc}$ is the filter quality factor. This last parameter is the main difference with respect to the broadband SIC because adds one more degree of freedom to the system: the slope of the phase, or better the group delay, can be adjusted through the Q factor.

Fig.2.11 shows the results combining the RLC SIC to the measured S-parameters of the fourth disposition of Fig.2.3. Both magnitude and phase are matched over a wide frequency range leading to a -20 dB cancellation bandwidth of around 80 MHz (Fig.2.12). However, when the SIC phase approaches $-90°$ or $-270°$ changing the quality factor does not affect the slope significantly. In these cases, the narrowband SIC acts as a broadband one, providing a cancellation bandwidth of only 16 MHz. To guarantee the group delay control, the SIC phase at f_{canc} should remain between $-135°and-235°$.

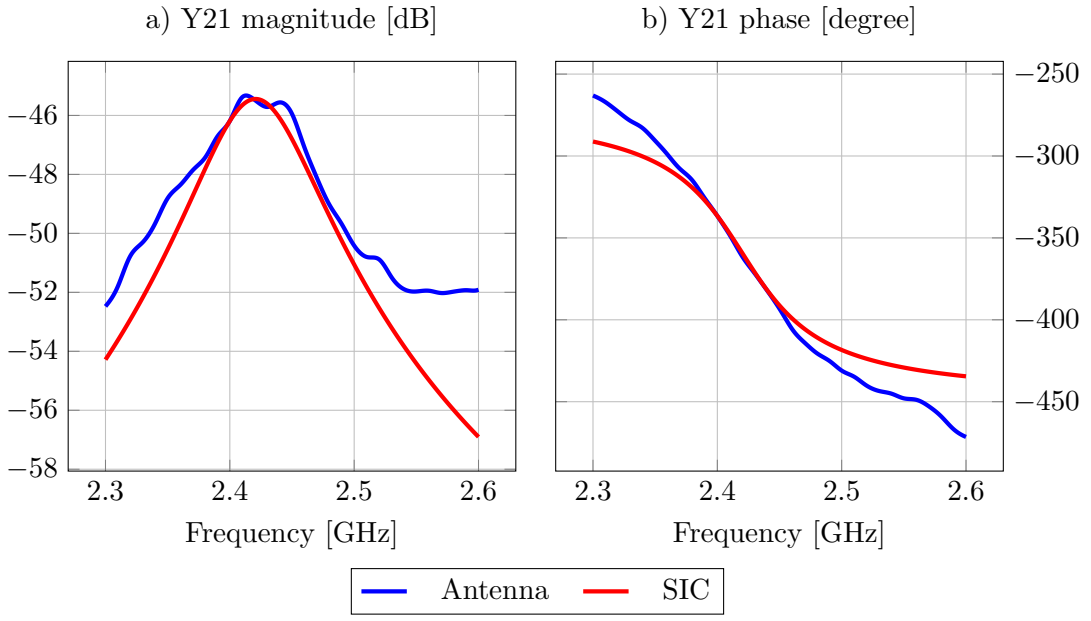

FIGURE 2.11: SIC and antenna coupling Y21 amplitude (a) and phase (b) vs frequency.

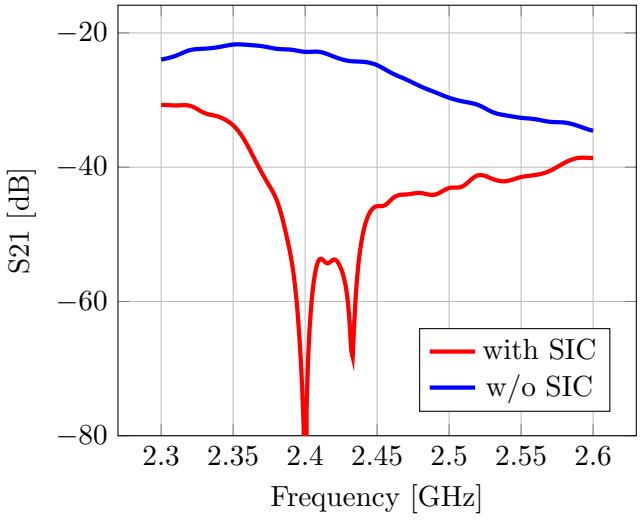

FIGURE 2.12: Antenna coupling with and without SIC.

Therefore, a coarse phase shifter that provides ±45° must be added in series with the SIC, as shown in Fig.2.10b.

2.2.3 Conclusion: SIC comparison

Table 2.1 summarizes the canceller bandwidth together with the advantages and disadvantages of each topology. Looking at the cancellation bandwidth, the narrowband SIC seems to be the best choice. However, other parameters such as the feasibility and the tunability must be taken into account. For what concern the former, the narrowband SIC presents a design challenge related to the Q factor needed for the cancellation. In

Topology	Cancellation BW [MHz]		Advantages	Disadvantages
RC-based (wideband)	14		Easy design Simple tuning	Small canc. bandwidth
RLC-based (narrowband)	Min 16	Max 80	Wide canc. bandwidth	Limited slope control
RLC + Coarse phase shifter	80		Wide canc. BW for any phase	Difficult tuning High Q factor

TABLE 2.1: Summary of the comparison between different canceller topologies.

Appendix A the relationship between the RLC quality factor and the group delay around its resonant frequency (τ_0) is computed as:

$$Q = \frac{\omega_0 \tau_0}{2} \tag{2.6}$$

where $\omega_0 = 1/\sqrt{LC}$. With the measured data reported in Fig.2.6, to obtain a delay of 2-3 ns required for the cancellation, the filter quality factor falls between 15 and 25 for $\omega_0 = 2.5$ GHz. These values are difficult to obtain through integrated component especially passive inductors. Moreover, since the antenna interface changes with time because of the interactions with external environment, the SIC must be tunable. These requirements and the relative simplicity of the design, make the broadband SIC one of the most used topologies despite its limited cancellation bandwidth.

In 4G LTE standard, the duplex spacing (i.e. the frequency spacing between the TX and RX channels) varies between 30 and 400 MHz. In the extreme case (400 MHz), none of the analyzed canceller topologies is able to cover both TX and RX bands, meaning that the TX leakage cannot be cancelled with a single SIC. For this reason, in the architecture that is presented in this thesis, a dual cancellation path is adopted, with a broadband RF SIC for the main TX signal leakage and an auxiliary path for the TX broadband noise reduction.

Chapter 3

FDD Wireless Diversity Receiver with TX Leakage Cancellation in Transmit and Receive Bands

The works described in this thesis consist of a diversity receiver for Frequency Division Duplexing (FDD) mobile communication systems with TX leakage cancellation in both TX and RX bands. In this chapter, the system is described in detail starting from the system requirements and explaining the trade-off related to the proposed architecture. The reported data and text were published in [33] and the copyright belongs entirely to IEEE (©2018 IEEE).

3.1 Proposed System

Fig.3.1 shows the complete system block diagram of the proposed FDD transceiver. The diversity receiver is directly connected to the antenna and receives a strong TX leakage. The RF self interference canceller (SIC) block taps the TX output signal and injects it at the LNA input to reduce the TX leakage signal power and hence non-linear and reciprocal mixing effects on the diversity RX. However, antenna-antenna coupling has a typical group delay of 2-3 ns (Chapter 2) limiting the SIC bandwidth and, since the SIC is optimized for the TX band, it is not effective in cancelling the receive-band TX noise. However, while the main TX signal has to be reduced at the RX input because it could bring the diversity receiver to compression, the TX noise can be reduced also in the digital domain. For this reason, an auxiliary (AUX) receiver senses the receive-band TX noise at the transmitter output and provides this information to a digital equalizer that subtracts it from the diversity path. Since the antenna-coupling varies with time,

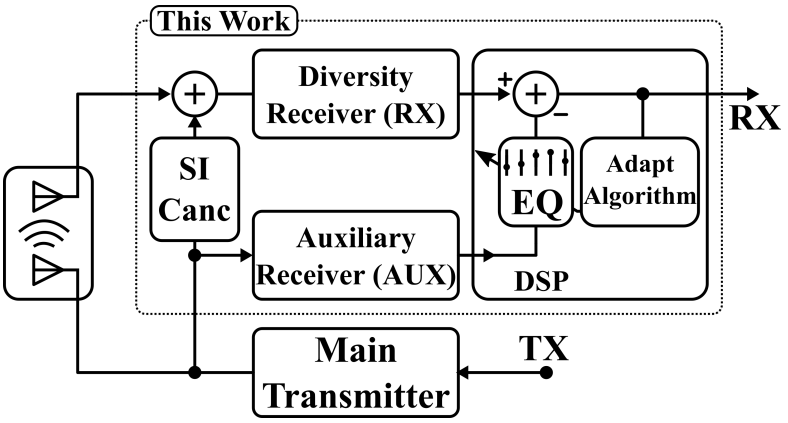

FIGURE 3.1: Simplified block diagram of the proposed system architecture([33]©2018 IEEE).

an adaptation algorithm keeps track of the environmental variations. In this thesis, the noise reduction process is referred as Digital Noise Reduction (DNR).

This chapter is divided as follows: in the rest of this section, the system requirements related to the diversity RX and to the DNR algorithm are computed; the diversity and auxiliary receiver are then described in Section 3.2 and 3.3. The theory and simulation on which the DNR process is based on are then presented in Section 3.4.

3.1.1 System and Building Blocks Requirements

As extensively discussed in Chapter 1, for a 20 MHz LTE channel, the required sensitivity is -94 to -90.5 dBm [2], which corresponds to a maximum noise figure (NF) of 8.5-12 dB. In practice, state-of-the-art LTE transceivers achieve lower noise figure but gain compression, reciprocal mixing and receive-band TX noise leakage can degrade the NF. Receiver LO phase noise requirements are dictated by reciprocal mixing with the largest OOB blocker of -15 dBm. To avoid performance degradation, SIC must lower the TX leakage below -15 dBm. Considering a maximum TX power of 23 dBm and 25 dB of ISO_{TX-RX}, a minimum RF cancellation of 13 dB is required.

For intermodulation tests, the most stringent IIP3 requirements are set by the intermodulation between OOB blocker and the TX leakage and depend on the relative frequencies of the blocker with respect to the TX and RX ones. In Chapter 1, Fig.1.4 reports the required IIP3 as a function of the TX-RX isolation for the FFS and HFS cases. Notice that, when SIC is used, the values reported in Fig.1.4 correspond to the effective IIP3, that is the IIP3 of a receiver without SIC that gives the same third-order distortion (IM3). The required RX IIP3 is more relaxed and can be inferred from the same plot when the cancellation in dB is added to the ISO_{TX-RX} on the x-axis. If no counter-measurements were taken to reduce the TX leakage, the isolation between

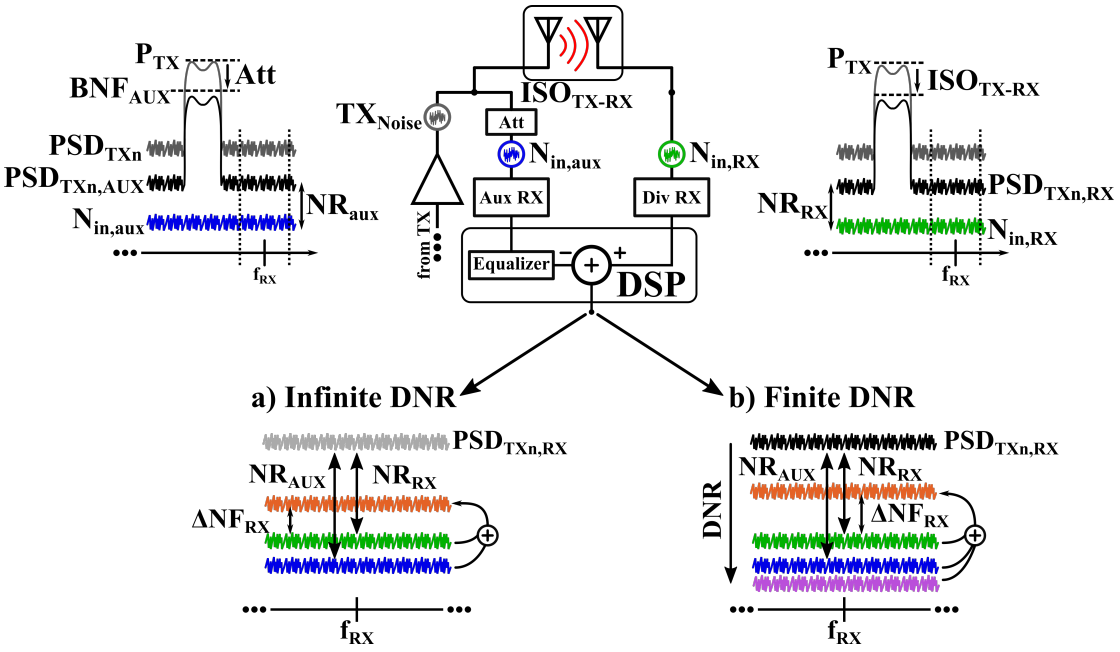

FIGURE 3.2: Simplified block diagram showing the noise levels in different point of the system considering (a) infinite DNR and (b) finite DNR (©2018 IEEE).

TX and RX would be determined only by the antennas' interface (around 25 dB from Chapter 2). Under this assumption, the required IIP3 would be more than 30 dBm in the FFS scenario and around 28 dBm in the HFS one.

3.1.2 TX Noise in the RX Band

Fig.3.2 shows a simplified block diagram of the receiver with TX noise reduction where the noise levels in different point of the system are indicated. To simplify the computation, the TX output is assumed to be a modulated signal with power P_{TX} [dBm] at frequency f_{TX} and a white noise with power spectral density (PSD) normalized to the TX power PSD_{TXn} [dBc/Hz]. Due to the limited ISO_{TX-RX}, part of the TX output is coupled to the diversity receiver, degrading its sensitivity. We define the ratio between the TX noise leakage and the diversity RX own input referred noise as the RX Noise Ratio (NR_{RX}). The diversity receiver noise figure (NF_{RX}) increases due to the presence of the TX noise[1] and its degradation ΔNF_{RX} can be easily computed as:

$$\Delta\text{NF}_{RX} = 10\log(1 + \text{NR}_{RX}) \tag{3.1}$$

Assuming a ISO_{TX-RX} of 25 dB[2], $\text{PSD}_{TXn} = -154$ dBc/Hz and a NF_{RX} of 5.5 dB when no TX is present, in Fig.3.3a the diversity receiver NF degradation is computed

[1] In this computation, only RX NF degradation due to TX noise is taken into account, RX non-linear effect are not considered.

[2] This value was chosen considering the simulation and measurements reported in Chapter 2.

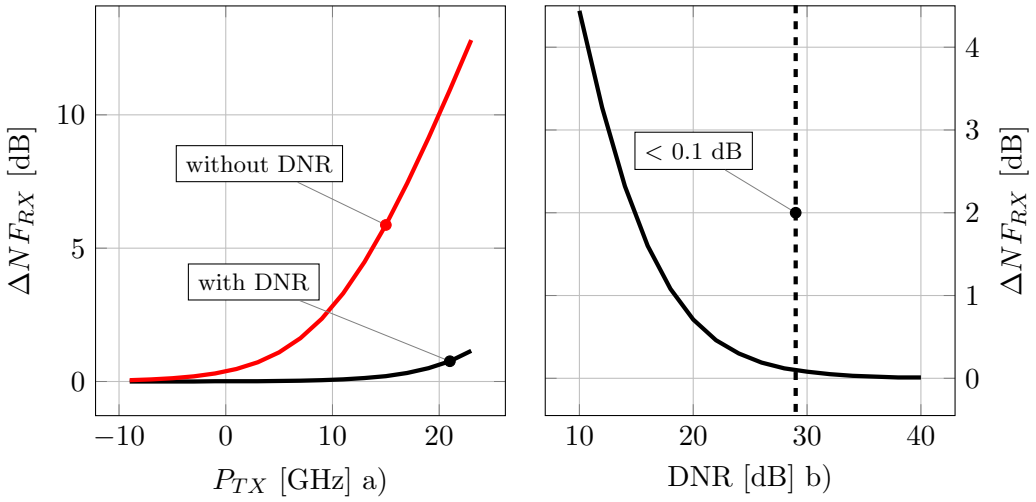

FIGURE 3.3: a) Simulated NF_{RX} degradation vs transmitter power with (black) and without (red) DNR (a) and versus DNR level (b).

as a function of P_{TX}. ΔNF_{RX} is not negligible when P_{TX} exceeds 5 dBm and it reaches 12 dB with the TX at full power ($P_{TX} = 23$ dBm).

Sensitivity degradation can be strongly reduced by sensing the TX noise through the auxiliary and subtracting it out from the RX signal. Digital equalization is necessary in order to maximize the correlation between the AUX and RX signals, therefore minimizing the difference (error) signal. While the noise sources of the RX and AUX are uncorrelated, the TX noise in the RX band appears at the output of the two paths as a correlated component and it is strongly suppressed. The amount of suppression in dB is defined in this thesis as DNR. Even assuming an infinite DNR, the NF_{RX} is degraded due to the noise added by the auxiliary receiver. To quantify this additional noise contribution, we can observe that the equalizer has to match the TX noise levels at the output of the AUX to the one at the RX output to minimize ΔNF_{RX}. Hence, after the equalization, the TX noise levels at the output of the two paths are both equal to PSD_{TXn} when referred to the RX input ($\text{PSD}_{TXn,RX}$ in Fig.3.2). If the ratio between the TX noise at the AUX input and the AUX own input-referred noise is defined as the AUX noise ratio (NR_{AUX} in Fig.3.2), ΔNF_{RX} depends only on the ratio between NR_{RX} and NR_{AUX} following the formula:

$$\Delta\text{NF}_{RX} = 10\log\left(1 + \frac{\text{NR}_{RX}}{\text{NR}_{AUX}}\right). \tag{3.2}$$

For example, if NR_{RX} and NR_{AUX} were equal, ΔNF_{RX} would be 3 dB.

Finite correlation between the TX noise at the AUX and RX outputs limits the final DNR value, as will be explained in Section 3.4. For this reason, the residual TX noise after the digital equalization process contributes to the final ΔNF_{RX} too Fig.3.2b.

DNR	$\mathbf{P}_{TX}$	$\mathbf{ISO}_{TX-RX}$	$\mathbf{PSD}_{TXn}$	$\mathbf{NF}_{RX}$	$\mathbf{NF}_{AUX}$	$\mathbf{BNF}_{AUX}$	$\mathbf{\Delta NF}_{RX}$
0 dB	23 dBm	25 dB	-154 dBc/Hz	5.5 dB	7 dB	5 dBm	**12.8** dB
30 dB	23 dBm	25 dB	-154 dBc/Hz	5.5 dB	7 dB	5 dBm	**1.15** dB
30 dB	23 dBm	25 dB	-144 dBc/Hz	5.5 dB	7 dB	5 dBm	**1.87** dB

TABLE 3.1: Summary of the system parameter used for theoretical computation for different DNR/PSD_{TXn} values.

Therefore, the total ΔNF_{RX} can be computed as:

$$\Delta\text{NF}_{RX} = 10\log\left(1 + \frac{\text{NR}_{RX}}{\text{NR}_{AUX}} + \frac{\text{NR}_{RX}}{DNR}\right). \tag{3.3}$$

Since NR_{RX} is a given, DNR and NR_{AUX} should be maximized. To ensure less than 0.1 dB of ΔNF_{RX} due to the residual TX noise, more than 28 dB of DNR is required, as shown in Fig.3.3b. To maximize NR_{AUX} and avoid compression in the AUX, a broadband attenuator (with gain Att[dB]) is placed in front of it and the minimum required Att is determined by the maximum blocker handling capability of the AUX, that is the power in dBm that degrades its NF by 1 dB (blocker NF BNF_{AUX}). The calculated ΔNF_{RX} with DNR for different TX power levels is shown in Fig.3.3a for an AUX NF (AUX_{NF}) of 7 dB and $\text{BNF}_{AUX} = 5$ dBm: ΔNF_{RX} is lower than 1 dB up to the full TX power of 23 dBm. In Table 3.1 a summary of the results and the system parameter used for the computation is reported. Notice that, even if PSD_{TXn} was raised to -144 dBc/Hz, ΔNF_{RX} would increase by less than 1 dB.

3.2 Diversity Receiver

In this section, an highly linear broadband current-mode receiver is introduced. To further improve its linearity without increasing power dissipation, a passive RF canceller is used. The complete diversity RX schematic is reported in Appendix C while only single block schematics are shown in this chapter.

3.2.1 Low-Noise Transconductance Amplifier (LNTA) Design

In [24], a highly linear common-gate LNTA was presented. The LNTA, reported in Fig.3.4a, has complementary p-n cross-coupled CG amplifiers working in class-AB for high 1-dB gain compression point. Gate cross coupling lowers the CG amplifier noise factor to $1+\gamma/2$ and rejects the third-order intermodulation product (IM3) due to the MOS second-order non-linear transconductance, improving IIP3. Better noise and IIP3 can be obtained if the CG LNTA source impedance is increased above its input impedance

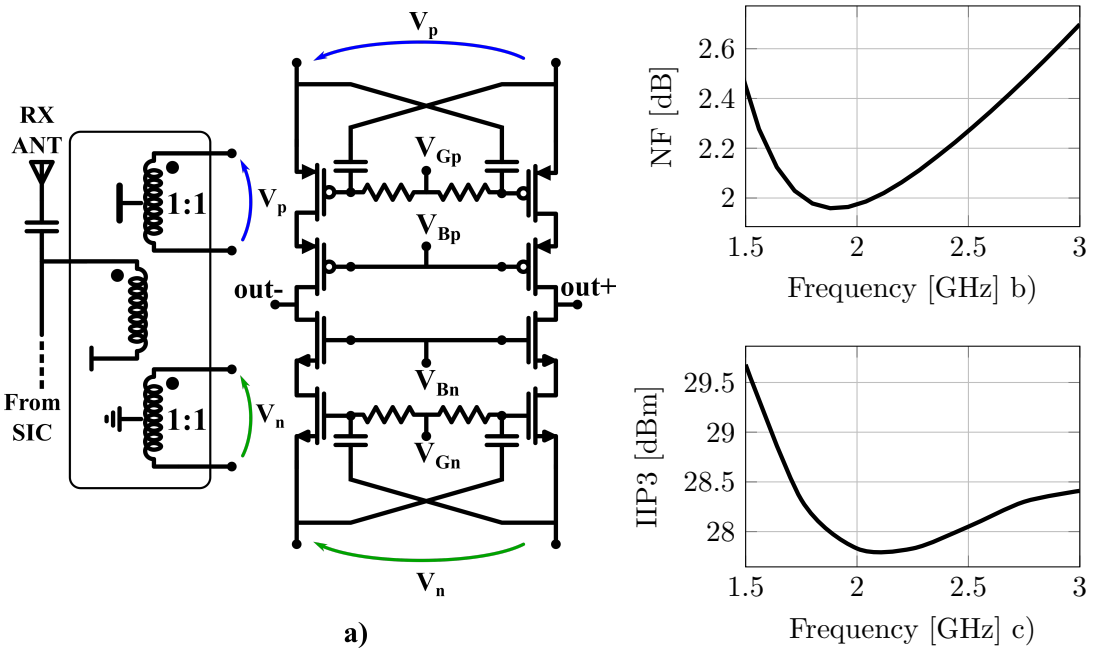

FIGURE 3.4: a) LNTA schematic. Simulated NF (b) and IIP3 (c) versus frequency.

[24] by making noise and distortion terms recirculate within the transistor that creates them. In a loss-less network, this also lead to impedance mismatch but, considering losses together with RF canceller loading impedance, acceptable impedance matching is reached.

A transformer with one primary and two secondaries with $k = 0.7$ implements the balun and broadband source impedance boosting on the secondary. The inductive impedance seen at the transformer primary resonates with the 3.2 pF series capacitor and the canceller capacitor to attain input impedance matching. The three-winding transformer was optimized for minimum overall noise when the antenna impedance is 50 Ω. LNTA simulation results are reported in Fig.3.4b) and c). The LNTA IIP3 is 28 dBm and its NF, including transformer losses, is below 2.5 dB between 1.5 and 2.5 GHz while drawing only 8 mA from the 1.8 V supply. Notice that the NMOS and PMOS input transistors are sized to obtain a $g_m/I_D = 10$ mS/mA and no derivative superposition is used to improve linearity.

3.2.2 Mixer and Transimpedance Amplifier (TIA)

The LNTA is ac coupled to a passive mixer driven by a 25% duty-cycle LO, followed by a transimpedance amplifier (TIA) with a real pole at 20 MHz. The TIA three stage amplifier is compensated exploiting the passive feedback network to achieve 1.6 GHz unity-gain loop bandwidth while drawing 3 mA from 1.8 V supply [34]. At the output

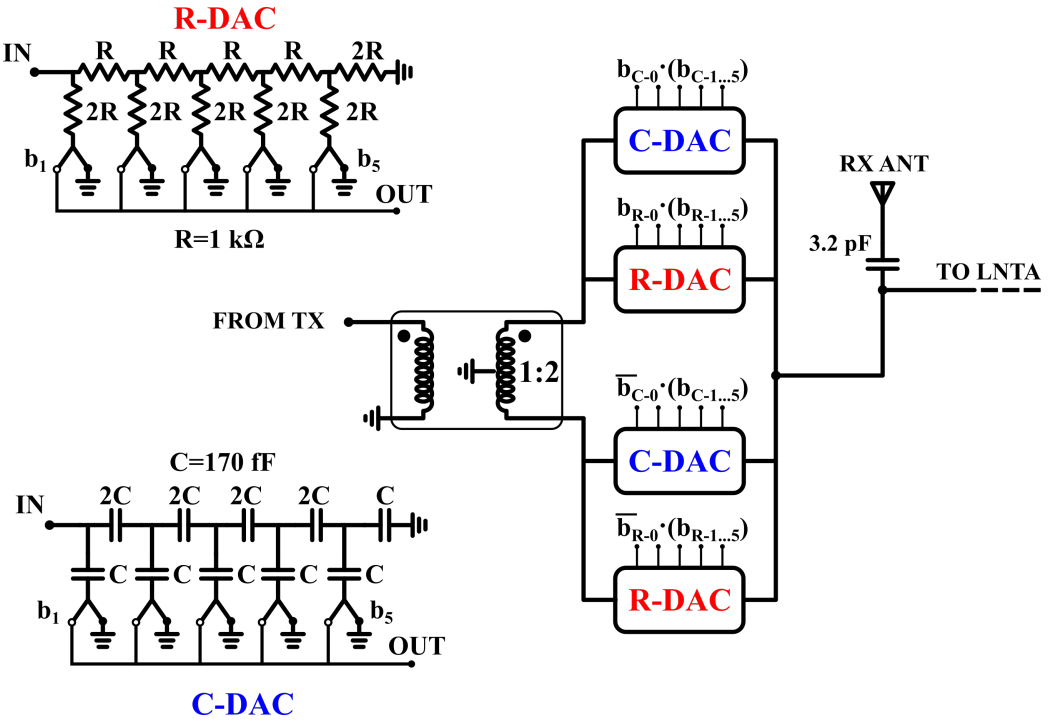

FIGURE 3.5: RF self-interference canceller schematic.

of the mixer, 20 pF capacitors to ground provide low impedance at frequencies above 600 MHz.

3.2.3 RF Self-Interference Canceller

Passive cancellers enable low power and high linearity [15]. Without internal amplification, minimization of fixed losses is key, especially at low ISO_{TX-RX}, in order to maximize the input impedance and minimize the noise injected in the RX. For this reason, in the proposed canceller, instead of cascading a magnitude control and stage and a phase control stage, two parallel variable attenuators are used (R-DAC and C-DAC) that generate quadrature output currents to be injected directly at the LNTA input as shown in Fig.3.5. This is advantageous also in term of precision: with the chosen topology, 5-bit precision in the two DACs is sufficient to ensure 27 dB of cancellation. Alternatively, error less than 4% and a phase error less than 2° would be required. In the test chip, a transformer is used to convert the canceller input signal to differential. In a fully integrated solution, the transformer is not needed since the TX signal is typically available in differential form at the output of the transmitter as in [20] and [35]. Moreover, since a relatively low-cancellation level is target, it is not crucial to fully capture Power Amplifier (PA) non-linearity. Hence, the canceller may be tapped at the output of the transmitter before the PA, where a large voltage swing is available [36], which would greatly simplify system integration. R-DAC and C-DAC are independently

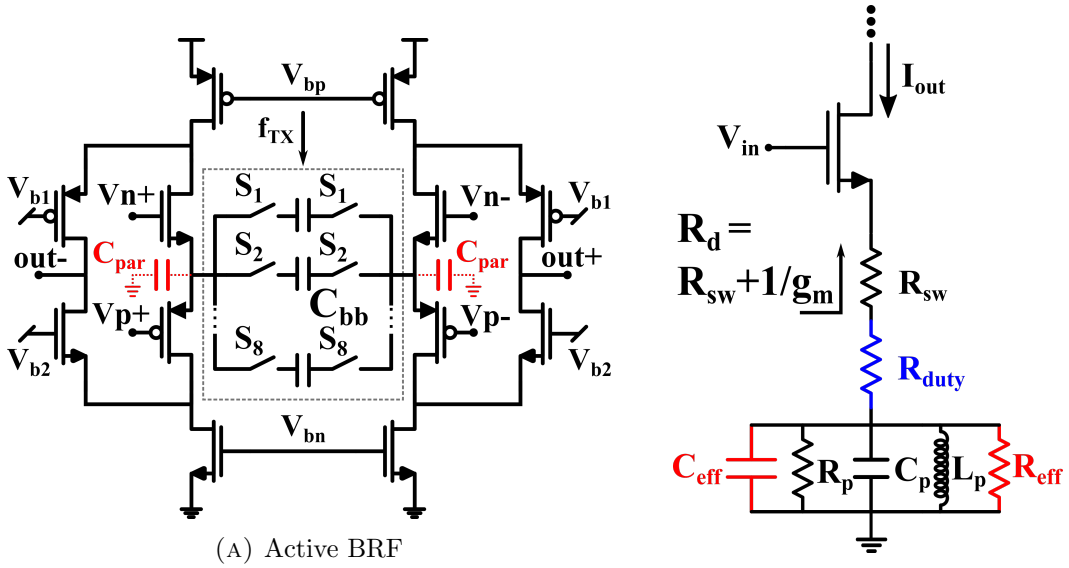

(A) Active BRF

(B) Equivalent model

FIGURE 3.6: a) Active band-reject filter and b) equivalent SE N-Only RLC model.

controlled with 6 bits (5 bits for modulus plus one for sign). The high impedance of the R/C latter protects the NMOS control switches from the large TX input signal, ensuring reliability and good linearity. Each switch is implemented with L=28 nm and floating gate control through a large (10 kΩ) resistor to distribute the residual voltage swing across the gate-source and gate-drain [37]. The differential input impedance of the DACs is 1 kΩ in parallel to 170 fF.

3.3 Auxiliary Receiver

The aim of the auxiliary path is to provide a baseband replica of the TX noise that falls into the RX band. This signal is then converted into the digital domain, processed through the digital equalizer and subtracted from the diversity output to reduce the TX noise in the diversity path. As explained before, the auxiliary receiver dynamic range needs to be as high as possible to reduce the ΔNF_{RX}. For this reason, an input band reject filter (BRF) based on a N-Path architecture is proposed with a very high dynamic range, thus reducing the requirements of the following blocks. Moreover, the N-Path filter is embedded in an active circuit thus reducing the LO leakage and loading effects since it is not power matched to the source. The complete auxiliary receiver schematic is reported in Appendix C while only single block schematics are shown in this chapter.

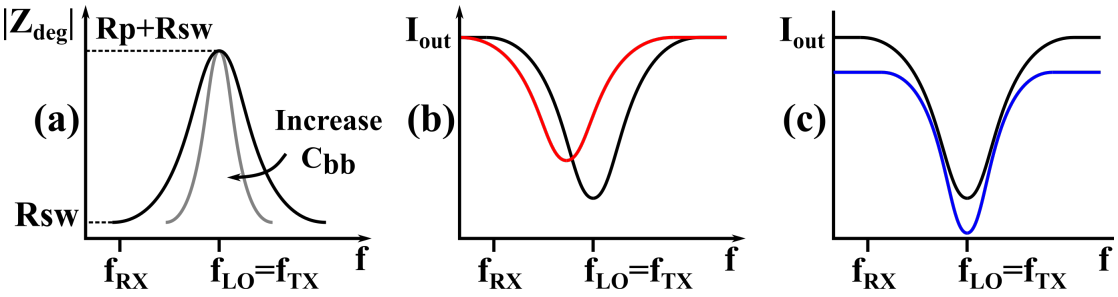

FIGURE 3.7: a) Ideal degeneration impedance versus frequency. b) Output current versus frequency with (red) and without (black) parasitic capacitance effects. c) Output current with (blue) and without (black) reduced duty cycle effects.

3.3.1 Active Band-Reject Filter

The schematic of the active BRF is shown in Fig.3.6a. The fully differential P-N common source input stage is degenerated through a N-Path filter. The filter can be modeled as an RLC tank (Fig.3.6b) as explained in detail in the Appendix B providing a large degeneration impedance at the frequency of the LO and a much smaller one far away from it (Fig.3.7a). Employing the TX LO, the transconductance gain of the band-reject filter is:

$$G_m = \frac{g_m}{1 + g_m R_{deg}} \tag{3.4}$$

where R_{deg} is equal to R_{sw} in the RX band and $R_{sw} + R_p$ at f_{TX}. The value of the parallel resistance R_p is determined by the driving impedance of the N-Path filter ($R_d = 1/g_m + R_{sw}$), the number of clock phases (N) and clock duty cycle, following the formula [7]:

$$R_p = \frac{N \sin^2(\pi D) + (1 - ND)D\pi^2}{N((D\pi)^2 - \sin^2(\pi D))} \cdot (1/g_m + R_{sw}). \tag{3.5}$$

With N=8, the rejection is 26 dB. As explained in the Appendix B, as N increases, R_p and thus filter rejection (TX_{rej}) increases, relaxing the dynamic range requirement of the following blocks. However, as the number of parallel paths increases, the parasitic capacitances (C_{par} in Fig.3.6a) also grow, down shifting the resonant frequency and degrading the peak rejection (Fig.3.7b). This is modeled by C_{eff} and R_{eff} [38] in Fig.3.6b. For N=8, $C_{eff} \approx C_{par}$, hence increasing the number of phases beyond eight does not significantly improve the rejection. To avoid the degradation of the in-band gain for a TX-RX spacing of 50 MHz or higher, the size of the baseband capacitance C_{bb} was set to 8 pF. The input transistors are biased at 2 mA each giving a single-ended transconductance of 40 mS. The filtered output signal current is absorbed by two folded cascode transistors biased at a reduced current of 0.5 mA and is then fed to a four-phases passive down-conversion mixer.

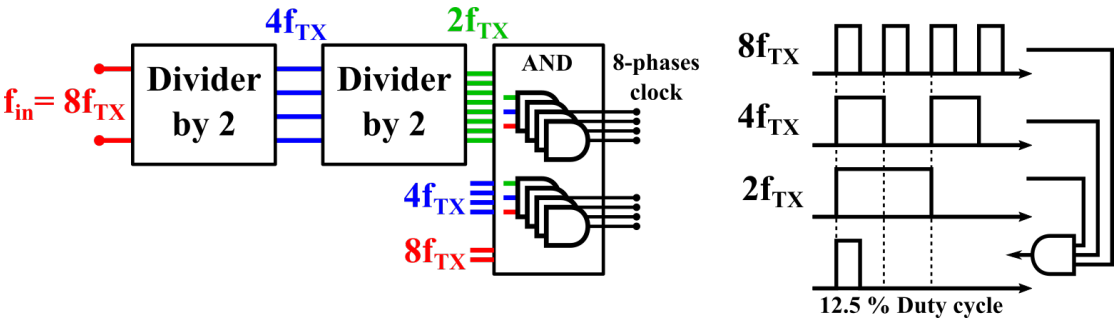

FIGURE 3.8: 8-phases LO generator block diagram [9].

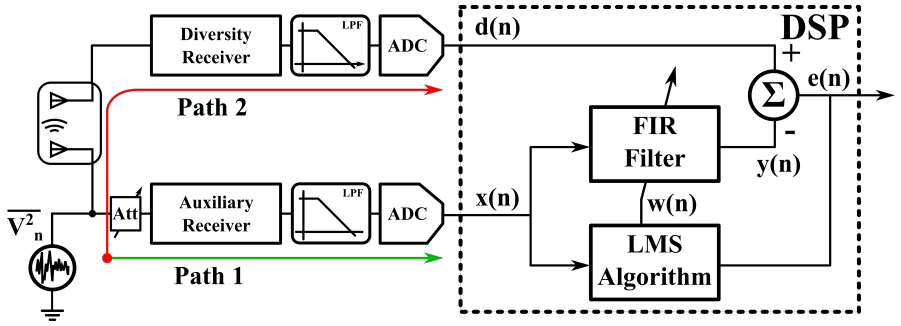

FIGURE 3.9: Simplified system model. The digital path must equalize the difference between Path1 and Path2 to reduce the TX noise in the RX band ([33] ©2018 IEEE).

3.3.2 Baseband TIA and LO Phase Generators

The baseband TIA provides a first-order filtering with a pole at 15 MHz. The TIA OpAmps have the same structure of the RX ones but, thanks to the reduced blocking requirements, the DC current is reduced to 2 mA. The clock for the passive mixers is obtained through on-chip dividers clocked from external generators at $4f_{TX}$ and $2f_{RX}$, respectively. The eight phases at f_{TX} are generated as shown in Fig.3.8 [9]: the first frequency divider by two drives the second one with 50% duty-cycle waveforms. The final 12.5% duty-cycle clocks are generated ANDing three 50% duty-cycle waveforms at $4f_{TX}$, $2f_{TX}$ and f_{TX}, so that the edges of the output clock are determined by the input signal ones, minimizing phase noise and consequentially reciprocal mixing in the BRF. Increasing the TX frequency, the finite BRF clock rise and fall time lower the duty cycle [7]. This can be modeled as an additional resistance (R_{duty} in Fig.3.6b) that increases the TX rejection but also lowers the gain and increases the auxiliary path NF (Fig.3.7c).

3.4 Digital Algorithm

To understand the digital algorithm working principle in an intuitive way, a simplified block diagram of the system (Fig.3.9) is used. The TX noise in the RX band is modelled as a white noise generator, connected to the auxiliary receiver input through an

attenuator and coupled to the diversity receiver. The receivers down-convert a signal located in a frequency range of 20 MHz around the RX carrier and the analog-to-digital converters (ADCs) converts it to digital. In this scenario, the FIR filter must equalize the difference between Path1 and Path2 referred in Fig.3.9. Although the receivers provide unequal in-band gain, the real asymmetry comes from the transfer function of the coupling between the antennas: as already explained in Chapter 2, while showing almost flat magnitude over the working bandwidth, a delay in the order of 2-3 ns introduces a sharp phase variation in the leakage path. Therefore, the equalizer main task is to provide delay control of the signal coming from the auxiliary receiver. Moreover, the interaction of the antennas with the external environment changes the coupling transfer function over time, requiring an adaptive equalization mechanism.

The relative simplicity of the coupling model between the antennas, the moderate desired cancellation[3] and the need to implement a low-cost digital path suitable for a mobile application suggest designing an equalizer based on an adaptive Least-Mean-Square (LMS) finite impulse response (FIR) filter. The LMS algorithm is a recursive method belonging to the Wiener filtering theory that gives a good compromise between computational requirements, rate of convergence, steady state error and robustness. In order to generalize the discussion, all the theory will be formulated in complex form and the signals are assumed to wide-sense stationary and zero-mean.

3.4.1 LMS-FIR Equalizer

An adaptive equalizer based on the LMS algorithm is characterized by two basic processes, filtering and coefficients adaptation, defined in matrix form as follows:

$$\begin{aligned} y(n) &= \mathbf{w}^H(n)\mathbf{x}(n) \\ \mathbf{w}(n+1) &= \mathbf{w}(n) + \mu e^*(n)\mathbf{x}(n) \end{aligned} \tag{3.6}$$

where ^{H} is the Hermitian transposition, $\mathbf{w}$(n) the filter coefficients vectorm μ the step-size and e(n) the error defined as:

$$e(n) = d(n) - y(n) = d(n) - \mathbf{w}^H(n)\mathbf{x}(n). \tag{3.7}$$

In the proposed architecture, the unknown signal d(n) is the output of the diversity receiver, the equalizer input x(n) is the signal at the auxiliary path output and y(n) is the FIR filter output(Fig.3.9). The final output of the system is the instantaneous error that, from Eq.(3.7), is the difference between the signal coming from the diversity

[3]With the system model proposed in **Chapter:TXNoise**, 28 dB of TX noise reduction are sufficient to obtain less than 0.1 dB of $\Delta\mathrm{NF}_{RX}$.

receiver and the equalized auxiliary output. It can be demonstrated [39] that, when the step-size μ is properly chosen, the Wiener filter represents the optimal solution[4] to which the LMS algorithm converges in an iterative way. From the Wiener theory, the minimum mean-square-error (MSE) is:

$$\begin{aligned} \xi_{min} = E[e(n)e(n)^*] = E[|d(n)|^2] - E[|y(n)|^2] = \\ = \sigma_d^2 - \mathbf{p}^H \mathbf{w}_0 = \sigma_d^2 - \mathbf{p}^H \mathbf{R}^{-1} \mathbf{p} \end{aligned} \tag{3.8}$$

where E indicates the expected value, σ_d^2 the variance (i.e. power) of d(n), $\mathbf{w}_0$ the vector of the optimum filter coefficients, $\mathbf{p}$ the cross-correlation vector of the two receivers' outputs and $\mathbf{R}$ the autocorrelation matrix of x(n). The DNR was defined as the ratio between the TX noise power at the output of the RX (i.e. σ_d^2) and the TX noise power after the digital equalization (i.e. ξ_{min}). Therefore, the DNR can be found normalizing the steady-state MSE over the input signal power, obtaining:

$$\mathrm{DNR}[dB] = 10log_{10}(1 - \mathbf{p}_n^H \mathbf{R}_n^{-1} \mathbf{p}_n) \tag{3.9}$$

where $\mathbf{p}_n$ and $\mathbf{R}_n$ are the cross correlation vector and correlation matrix normalized to the input signal power. This expression highlights that the power of the residual signal after the equalization depends only on the statistical parameters of the input signals: the higher is the correlation, the lower is the steady-state MSE. Since the TX noise bandwidth is inherently much larger than the RX channel, the resulting poor correlation is the main DNR limitation.

However, the analog filters in the two paths limit the bandwidth of the TX noise, spreading the signals autocorrelation (and cross correlation) over a larger time interval. For an ideal low pass filter with cutoff frequency f_c and transfer function $H_{id} = \mathrm{rect}(f/2f_c)$, the computed DNR with a fourth-order Wiener filter versus the normalized antenna group-delay (δ/t_s) for different frequency ratios [5] (f_s/f_c) is reported in Fig.3.10a. From these results, it can be noticed that the main limitation comes from the fact that the group delay between the antennas is only a fraction of the sampling period, limiting the DNR for low f_s/f_c to 10-20 dB. Moreover, the finite analog low pas filter order affects the DNR, lowering the correlation between the sampled signals with respect to the ideal low pass filter case. For example, setting f_s=40 MHz, f_c=15 MHz (f_s/f_c=8/3), and δ=3 ns ($\delta/t_s = 0.12$), the total DNR is 5 dB with a first order Butterworth low-pass filter and converges to the value previously computed when the filter order becomes very large (Fig.3.10).

[4] The optimal solution is the one that minimizes the error e(n).

[5] The frequency ratio between the sampling frequency f_s and the filter cut-off frequency f_c is simply the ADCs oversampling ratio.

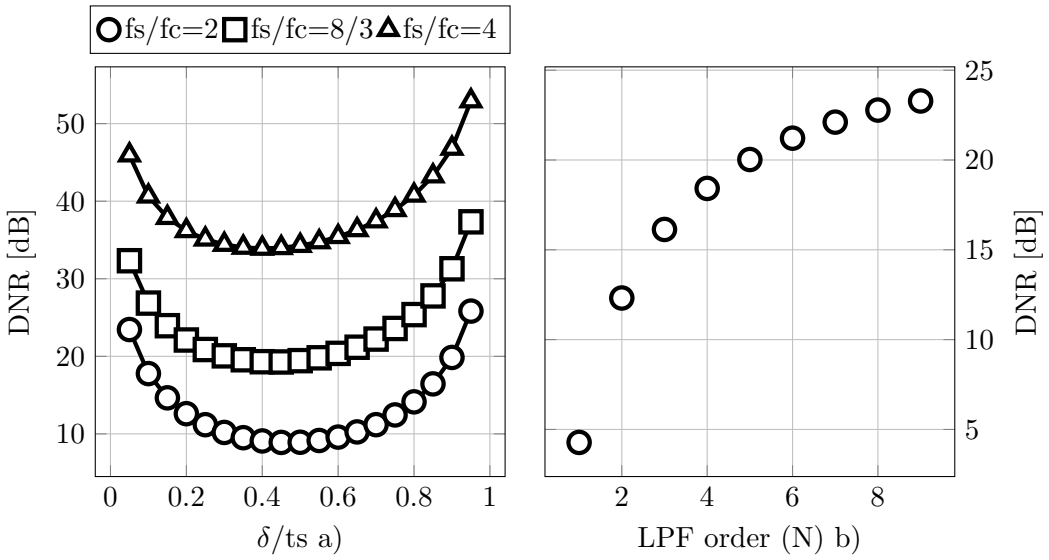

FIGURE 3.10: Computed DNR versus (a) normalized group delay δ/ts for different sampling/cutoff frequency ratios and (b) LPF order N.

3.4.2 System Simulations

A combined MATLAB-Simulink model was developed to simulate the performance of the digital path. The antenna's coupling is modelled as a broadband attenuation of 25 dB and a constant group delay of 3 ns. The cut-off frequency of the baseband low-pass filters is set to $f_c = 15$ MHz considering the LTE 20 RF channel bandwidth. To minimize the power consumption, ADCs oversampling ratio of 2 is used ($f_s = 40$ MHz). As shown in the previous section, the correlation between the sampled signal at the receivers output is what determines the amount of DNR. For this reason, the lowpass filter order N is chosen equal to 5 to guarantee enough correlation and a minimum DNR of 20 dB. To understand better where this value comes from, referring to Fig.3.10a, this corresponds to the case of $f_s/f_c = 8/3$ with $\delta/t_s = 0.12$ that gives a DNR of $\approx 25dB$ with ideal LPFs. The final DNR is the one shown in Fig.3.10 that is 20 dB with LPFs order equal to 5. As digital equalizer, a fourth-order complex LMS-FIR filter is implemented. The FIR filter order is set considering the delay in the antenna coupling, the sampling frequency and the signal correlation resulting from the analog filtering. Since the sampling frequency is only twice the RF bandwidth, only few samples show a significant correlation and hence increasing the number of filter taps over four does not significantly improve the DNR.

Fig.3.11 shows the spectra at the output of the system with the digital algorithm turned on and off: the noise is reduced by 20 dB over the whole frequency range [-20:20 MHz] and by ≈25 dB in-band [-10:10 MHz] where the signal is stronger. However, the DNR depends on the group delay between the antennas. In Fig.3.12, the simulated DNR

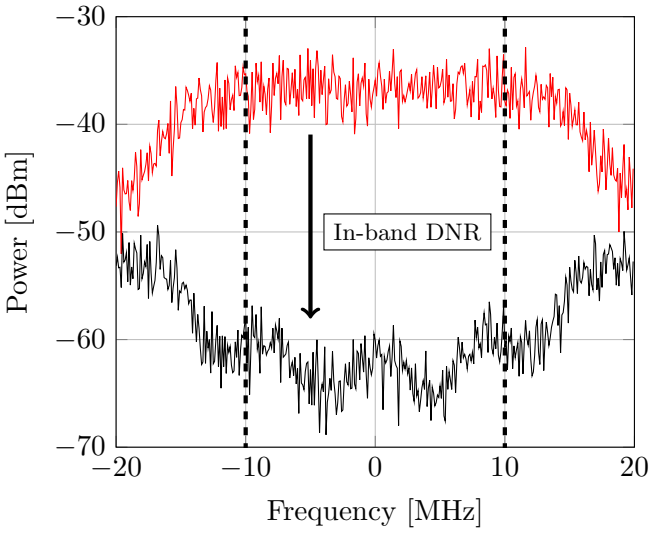

FIGURE 3.11: Simulated spectra before (red) and after (black) DNR with $\delta = 3$ ns.

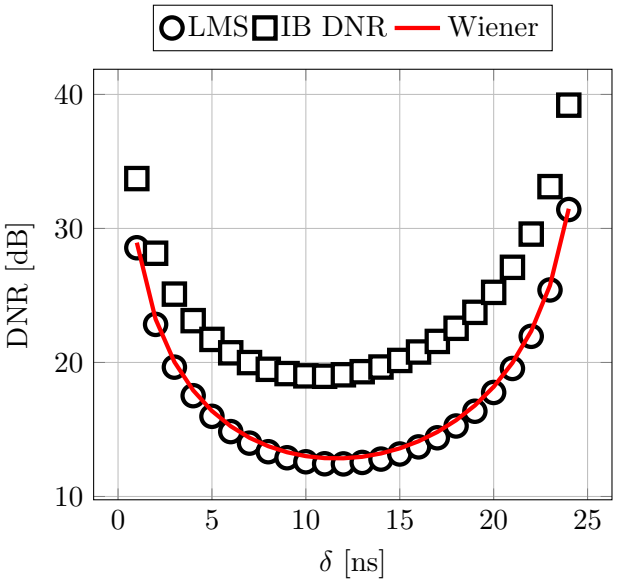

FIGURE 3.12: DNR versus antenna group delay. The in-band DNR considers only the noise power within -10/10 MHz.

versus δ is reported for different cases; the LMS equalizer (circles) is compared with the Wiener implementation (red continuous line) showing that the performance degradation introduced by the LMS approximation is essentially negligible. The other curve (squares) refers to the in-band [-10:10 MHz] power reduction, that is the real DNR of interest for the intended application. Moreover, it can be notice that the DNR is maximized when the group delay δ is zero or a multiple of the sampling period since the auxiliary output signal is equal to the diversity RX one simply delayed by a multiple of the sampling time (i.e. fully correlated). This suggest that the trend of the DNR is periodic with respect to δ, as shown in Fig.3.13. When δ is between t_s and $2t_s$ the noise reduction is higher because the FIR filter can exploit also the correlation of the signal with the previous

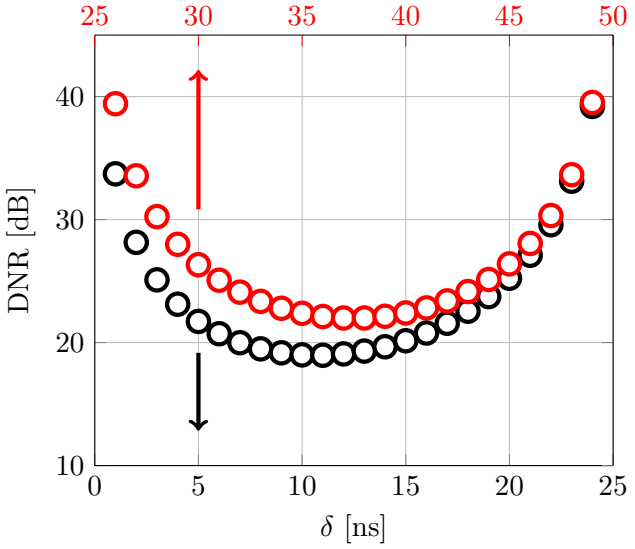

FIGURE 3.13: DNR versus antenna group delay for δ between 0 and t_s (black circles) and δ between t_s and $2t_s$ (red circles).

RF BW [MHz]	**f_s [MHz]**	**LMS-FIR Taps**	**Delay Taps**	**In-Band DNR [dB]**
20	40	4	1	**30**
40	80	8	2	**39**
80	160	16	4	**42**

TABLE 3.2: DNR performance versus RF bandwidth.

more correlated sample. For this reason, in the final implementation of the LMS-FIR filter (Fig.3.14), an additional delay tap is added in the RX path, improving the DNR for small δ in the range of 0-10 ns.

Additional simulations were performed for wider signal bandwidths, up to 80 MHz, to evaluate the applicability of the technique to future systems and the results are reported in Table 3.2. For the same antenna delay, with a small increase in the number of FIR filter taps, improved DNR would be achieved since the ratio δ/t_s is approaching to zero when sampling frequency is increased.

Up to now, only direct coupling between the antennas has been considered. To take into account also a possible reflection of the TX signal, a second path with attenuation $|\mathrm{ISO}_R|$ and group delay δ_R was added in parallel to the main one (Fig.3.15a). Fig.3.15b) shows the DNR degradation ΔDNR considering different delay/attenuation levels. In all cases, ΔDNR remains between -7 and -2 dB, corresponding to an additional $\Delta\mathrm{NF}_{\mathrm{RX}}$ of 0.35-0.06 dB with respect to the value showed in Fig.3.3 for $P_{\mathrm{TX}} = 23$ dBm.

The above considerations have been done assuming noise-less receivers. However, the simulations confirm that the noise generated by the two down-conversion paths does not

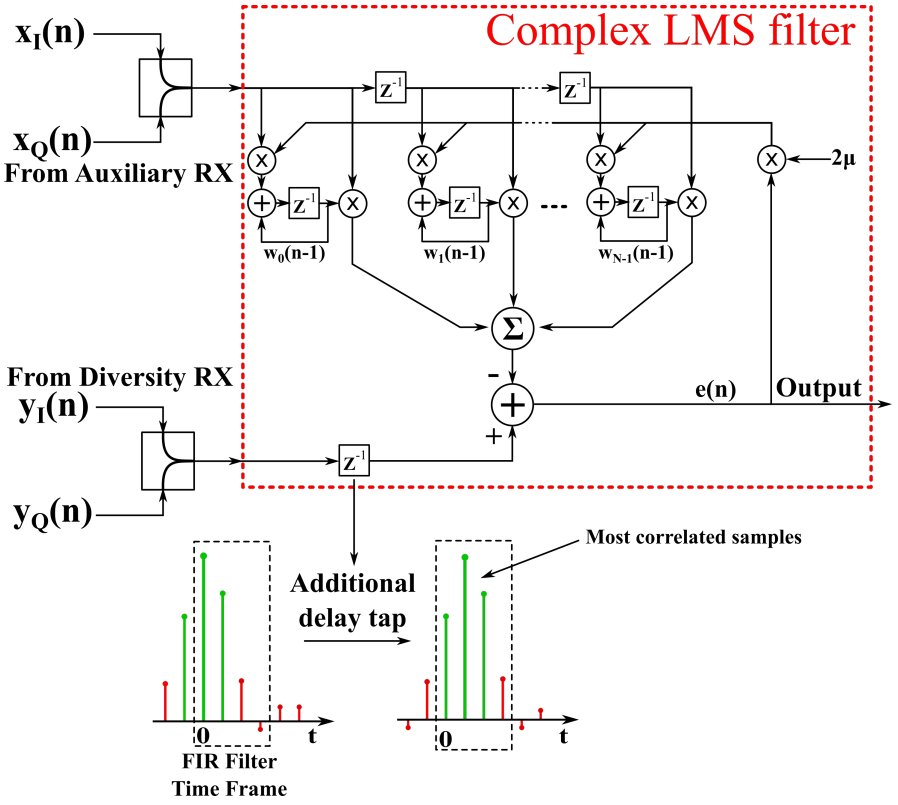

FIGURE 3.14: Block diagram of the digital path. The added delay tap improves the DNR exploiting the most correlated samples of the noise signal.

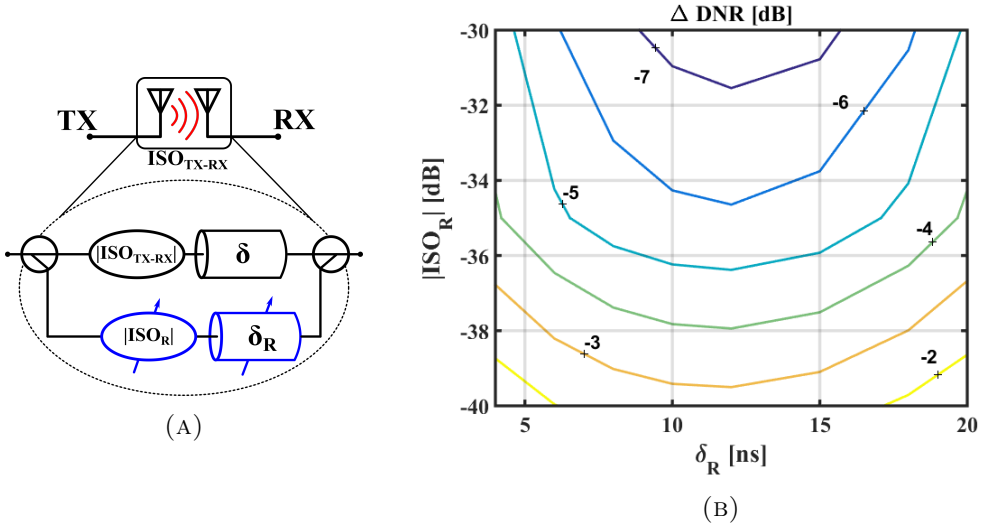

FIGURE 3.15: a) Antenna coupling model with main (black) and reflected (blue) paths. b) ΔDNR versus attenuation $|\mathrm{ISO}_R|$ and delay δ_R.

limit the final value of the DNR, since it is uncorrelated with the TX one. For the same reason, the algorithm is able to restore the RX sensitivity also in presence of a modulated RX signal coming from the diversity antenna, without performance degradation.

Chapter 4

System Performance

The measured results of the proposed system are provided in this chapter. To give a complete system overview, the two receivers were first characterized individually before measuring the overall performance. The reported data and text were published in [33] and the copyright belongs entirely to IEEE (©2018 IEEE).

4.1 Measurement Results

The diversity and auxiliary receiver were fabricated in 28 nm CMOS technology thanks to *Marvell Technology Group Ltd* while the digital algorithm performing the digital noise reduction was implemented on a field-programmable gate array (FPGA). Fig.4.1 shows the chip micro-photographs: the active area of the diversity receiver is 0.51 mm^2 while the auxiliary receiver occupies 0.12 mm^2. This section is divided as follows: in Section

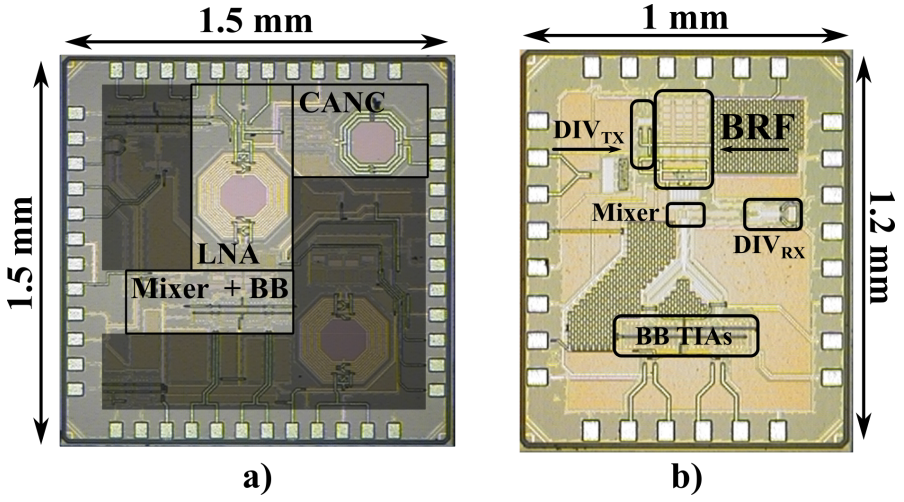

FIGURE 4.1: a) Diversity and b) auxiliary chip microphotogtraph ([33]©2018 IEEE).

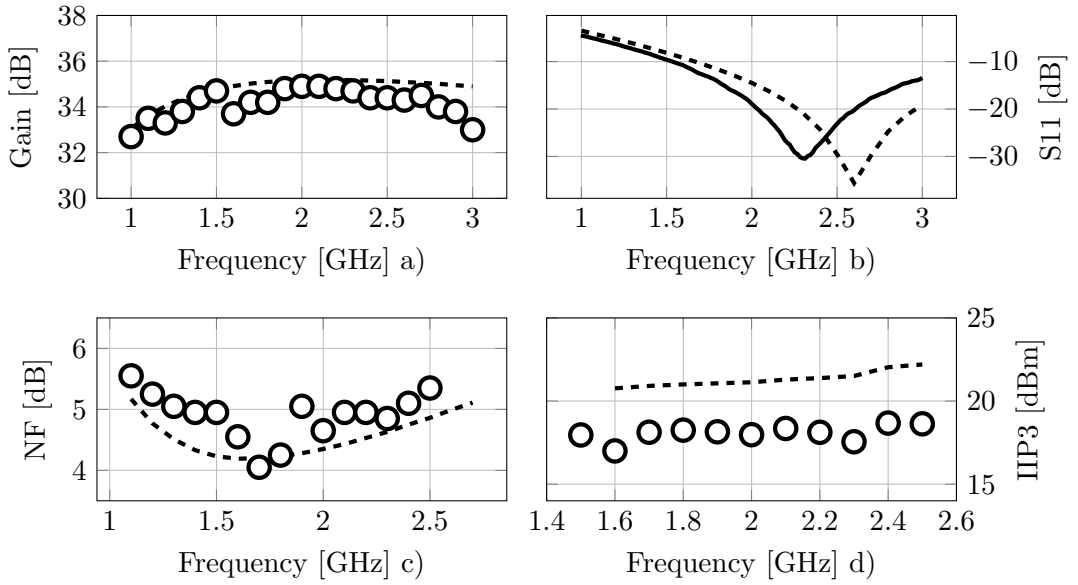

FIGURE 4.2: a) Measured (dots) and simulated (dashed line) diversity RX downconversion gain (a), NF (c) and IIP3 (d) versus input frequency. b) Measured (continuous line) and simulated (dashed line) S11 versus input frequency.

4.2 and 4.3 the diversity and auxiliary receiver measurements are reported respectively. Finally, in Section 4.4, the measured DNR performance and the results of the whole system are shown.

4.2 Diversity Receiver Performance

To characterized the main receiver, at first, the canceller was turned off. To achieve better accuracy, gain, return loss (S11) and noise measurements were carried out with an RF probe. The main measurement results are collected in Fig.4.2, proving good agreement with simulations. In particular, Fig.4.2a shows that the measured downconversion gain varies between 32.8 and 34.9 dB. The S_{11} is below -10 dB from 1.5 to more than 3 GHz (Fig.4.2b) and the RX double-sideband NF is 4.6 dB at 2 GHz and varies from 4 to5.4 dB between 1.2 and 2 GHz (Fig.4.2c). Turning on the canceller, the NF is degraded only by 0.4-0.8 dB depending on the canceller phase setting[1]. For what concern the linearity, the receiver IIP3 is 9 dBm IB and 18 dBm OOB at two GHz and it varies versus frequency as shown in Fig.4.2d. While the measured OOB IIP3 is close to the post layout simulation results, it is significantly lower than the LNA IIP3 reported in Fig.3.4c. The difference is related to two different effects: first, the TIA inter-modulation is not negligible at very large frequency offset; second, the LNA requires a very low load

[1]When only the canceller capacitances are turned on (90° or 270° phase shifting) only the switches add noise at the RX input. On the opposite, when also the in-phase portion of the canceller is turned on, the resistors contribute to the SIC noise, degrading more the RX NF.

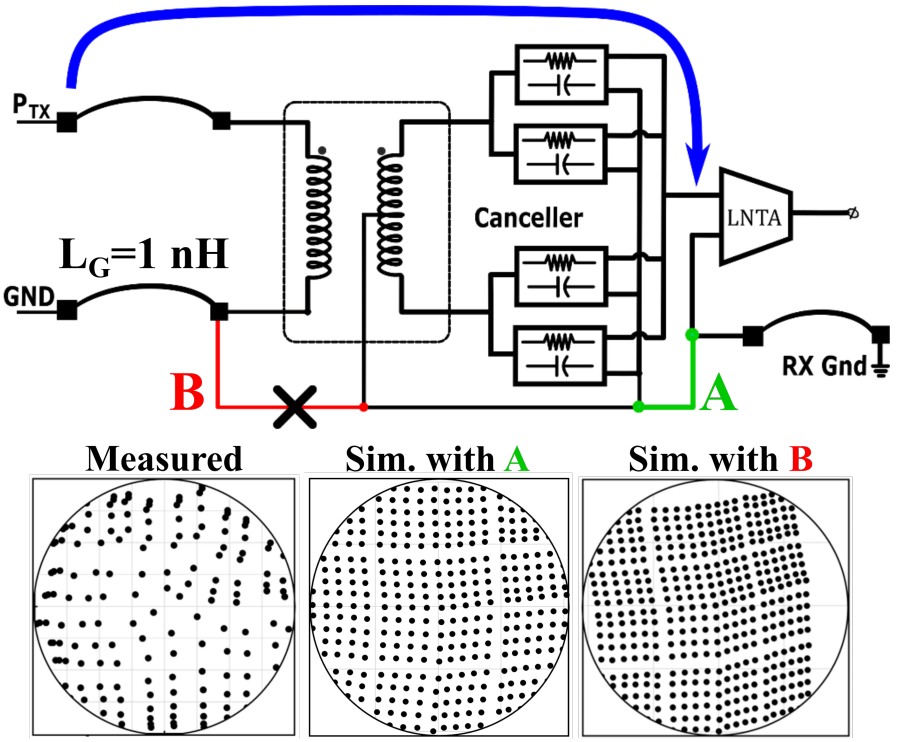

FIGURE 4.3: Measured and simulated effect of the different grounding schemes on canceller constellation. Measurements are referred to the configuration B ([33]©2018 IEEE).

impedance. Even though the mixer switches were designed for 10 Ω on-resistance, due to poor layout, the parasitic resistance coming from the interconnections increases the LNA load to over 40 Ω.

Fig.4.3 shows the normalized vector gain for all configurations of sign bit plus three MSBs for R-DAC and C-DAC. A significant constellation distortion is noticeable in the measured data. This issue was traced back to the signal unbalancing due to the connection of the canceller balun secondary winding center-tap to the primary ground (configuration B in Fig.4.3). However, if the secondary center-tap was connected to the receiver common ground (configuration A in Fig.4.3), the correct canceller gain is restored, as shown by the simulations in Fig.4.3.

To evaluate the SIC cancellation bandwidth, the pair of antenna PIFA described in Chapter 2 was used. The TX-RX coupling with this interface is around -25 dB with a group delay of 2.8 ns. The measurement result is reported in Fig.4.4: a minimum of 20 dB cancellation is achieved over 15 MHz bandwidth. The measurements confirm the theoretical analysis developed in Chapter 2 with a broadband SIC.

When the canceller is disabled, the input referred 1 dB compression point (P_{1dB}) for the IB gain was measured with an IB and OOB continuous wave (CW) blocker. The results are reported in Fig.4.5: when the canceller is disabled, the P_{1dB} is -15 dBm

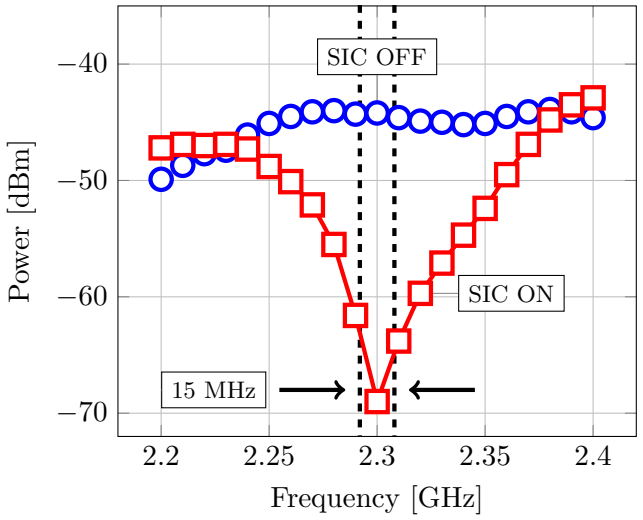

FIGURE 4.4: SI power measured using the pair of antenna PIFA from [31] with (red) and without (blue) SI cancellation.

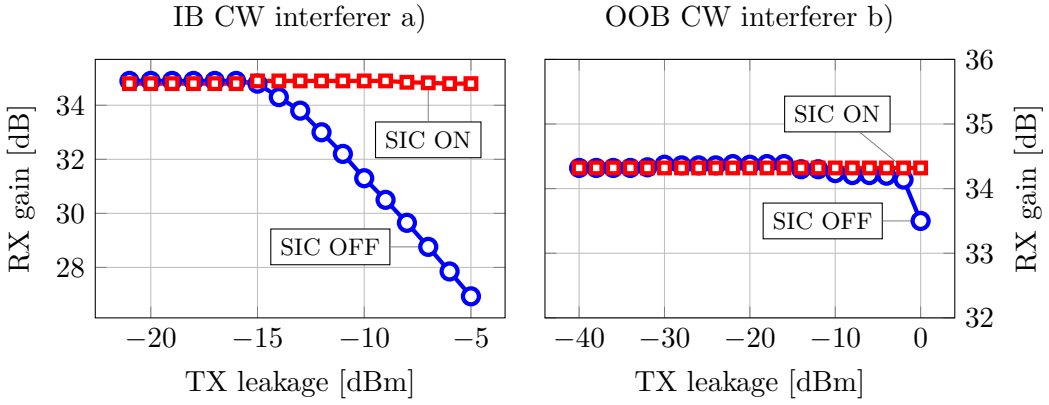

FIGURE 4.5: Measured in-band gain compression with (red) and without (blue) SIC with (a) IB CW interferer and (b) OOB CW interferer.

and 0 dBm with an in-band and OOB blocker respectively. Turning on the canceller, the in-band P_{1dB} goes to -5 dBm (Fig.4.5a) while no compression was observed with OOB TX leakage up to the maximum available power level of 0 dBm (Fig.4.5b).
Due to the self-interference cancellation mechanism, the TX leakage reaching the RX input is reduced. To evaluate the performance improvement given by the canceller, an effective IIP3 can be defined as the IIP3 of a receiver without SIC having the same third inter-modulation product (IM3). It has to be noticed that the IM3 is reduced proportionally to the amount of SI cancellation and it depends on the TX and the CW blocker relative frequency. As already pointed out in Chapter 1, there are two different scenarios: when the blocker appears at a frequency offset from the desired signal equal to $|1/2f_{TX} - f_{RX}|$ (HFS) and when the blocker is at $|2f_{TX} - f_{RX}|$ frequency offset (FFS). Since only the TX leakage is reduced by the SIC, this difference translates in a different IIP3 improvement: it improves by 1/2 dB for every dB of cancellation in HFS

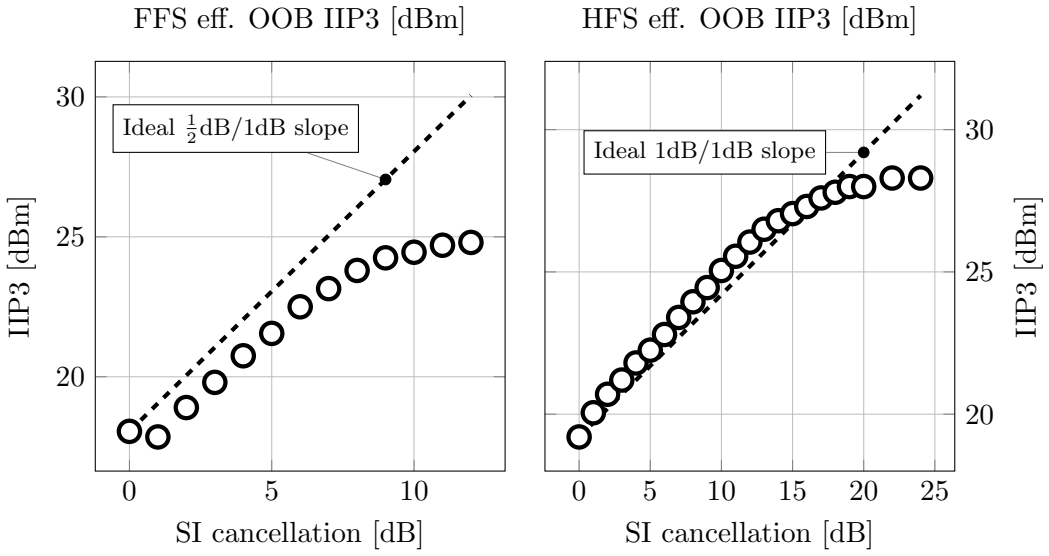

FIGURE 4.6: Measured effective OOB IIP3 in HFS/FFS scenarios.

scenario and by 1 dB/1 dB in the FFS case. Fig.4.6 shows the measurement results: in the HFS case the OOB IIP3 improves up to 25/29 dBm in HFS/FFS scenario. Beyond these values, IIP3 saturates due to canceller nonlinearity. The same measurement were repeated with in-band interferers showing that the IB IIP3 goes from 9 dBm without cancellation to 25 dBm with 16 dB of cancellation. Beyond this point, the effective IIP3 is again limited by the canceller. Simulations indicate that canceller linearity is limited by the chosen grounding scheme. In fact, the large signal present at the canceller primary modulates the switches on-resistance leading to distortion. From simulations, connecting canceller ground to the receiver ground, where ground bounce due to TX is much lower, the effective IIP3 in FFS for 20-dB cancellation reaches 35 dBm.

4.3 Auxiliary Receiver Performance

As for the diversity receiver, the main measurements were performed on the standalone auxiliary receiver. To provide the differential input signal, an external balun with 50-Ω on-chip resistors are used. Since they are used only for measuring purposes and they would not be present in a fully integrated solution (with the main TX), the losses of the balun and of the matching network are de-embedded from the measurements. To avoid confusion with the terminology, Fig.4.7 shows the measurement setup with frequency value of the signals in various point of the system. From now on, the LO frequency of the auxiliary receiver mixer is defined as f_{XR} while the one driving the N-Path filter of

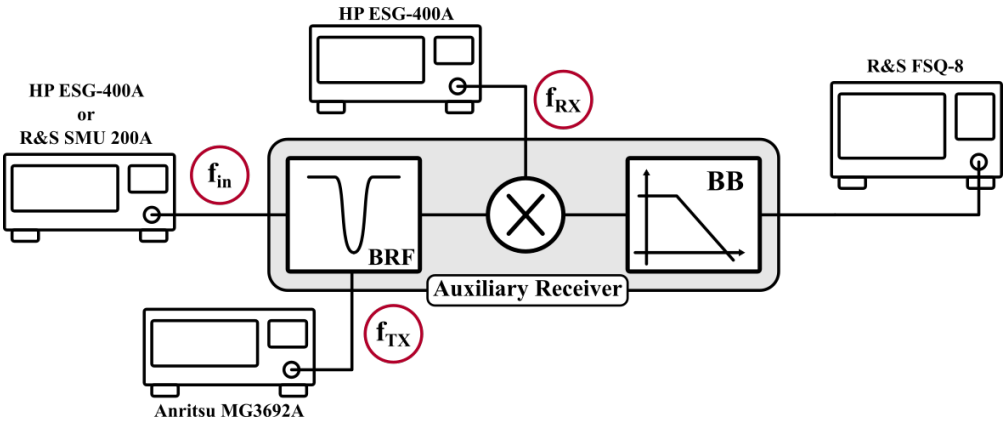

FIGURE 4.7: Auxiliary receiver measurement setup.

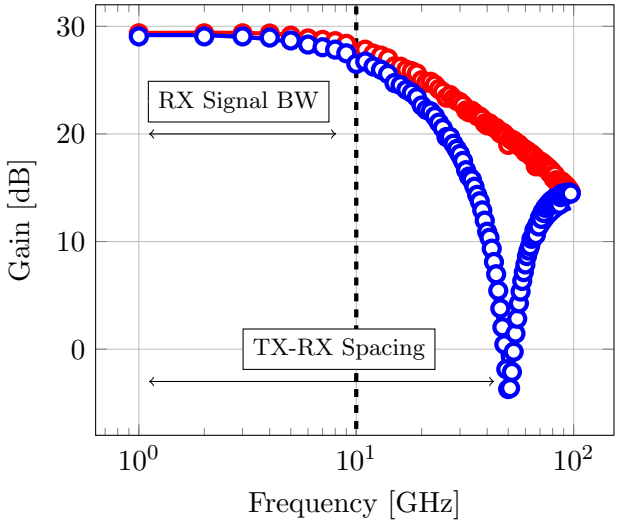

FIGURE 4.8: Measured (dots) and simulated (lines) BRF attenuation versus baseband output frequency for a fixed RX frequency offset (50 MHz).

the active band-reject filter is f_{TX}[2].

Setting $f_{TX} = 1.15$ GHz and $f_{RX} = 1.1$ GHz, the AUX downconversion gain was measured and the results are shown in Fig.4.8: the in-band gain is 30 dB and the active BRF provides additional 24.5 dB of attenuation at f_{TX} while not degrading the RX in-band gain. As reported in Fig.4.9, the BRF rejection is measured over a wide frequency range showing that the peak attenuation goes from 26 to 20 dB at high frequency due to the parasitic capacitances effect as explained in Appendix B. For the same reason, a negative frequency shift in the peak attenuation is present and it goes from 4 MHz at $f_{TX} = 750$ MHz to 10 MHz at $f_{TX} = 2$ GHz.

To test the effective enhancement of the active BRF to the large signal handling capability of the auxiliary receiver, the 1-dB compression point was measured in two

[2]This terminology comes from the fact that, in the complete system, the LO driving the AUX mixer is the same of the diversity RX while the BRF is tuned at the TX frequency to reject the main TX signal.

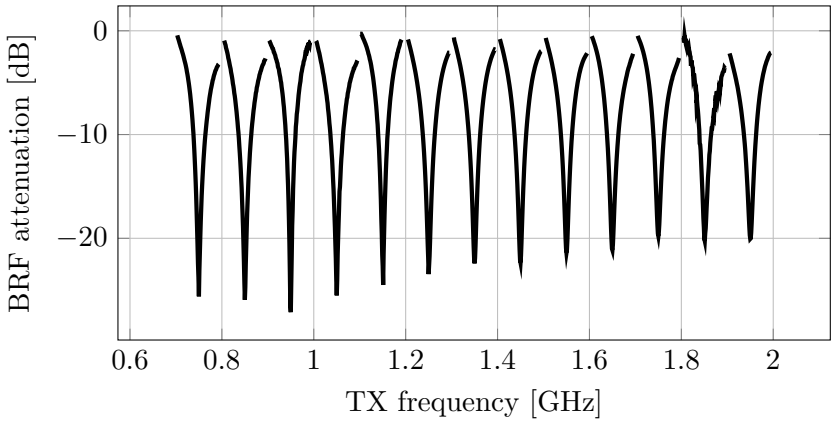

FIGURE 4.9: Measured active BRF attenuation versus f_{TX} for a fixed duplex spacing (50 MHz).

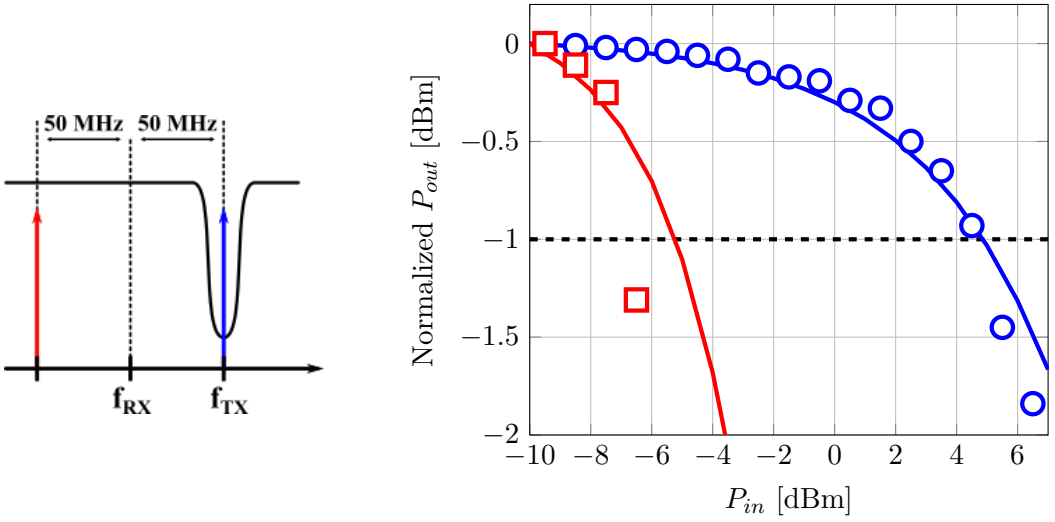

FIGURE 4.10: Simulated (continuous line) and measured (dots) in-band gain compression with a CW blocker placed at $f_{RX}+50$ MHz (circles) and at $f_{RX}-50$ MHz (squares) with $f_{RX} = 1$ GHz and $f_{TX} = 1.05$ GHz.

different cases (Fig.4.10) a CW signal was placed 50 MHz below and above the RX frequency ($f_{RX} = 1$ GHz), setting the TX frequency $f_{TX} = 1.05$ GHz. In the first case, the blocker passes unfiltered through the first stage, resulting in a P_{1dB} of -7 dBm; in the other case, the signal is filtered by the active BRF and the P_{1dB} is improved up to 5 dBm. The enhancement is not equal to the BRF attenuation because two different compression mechanism are involved: when the blocker is unfiltered, the compression comes mostly from the baseband TIA stage, while limited LO swing driving the BRF switches causes the compression when the blocker is at f_{TX}. For the same reason, as long as the attenuation is kept above 19 dB, the P_{1dB} is nearly constant at 5 dBm. This allows to achieve a high compression point even with modulated TX signals and to accomodate for the unavoidable frequency shift caused by parasitic capacitances. When a 20 MHz QPSK modulated signal is applied at the AUX input, the BRF provides an

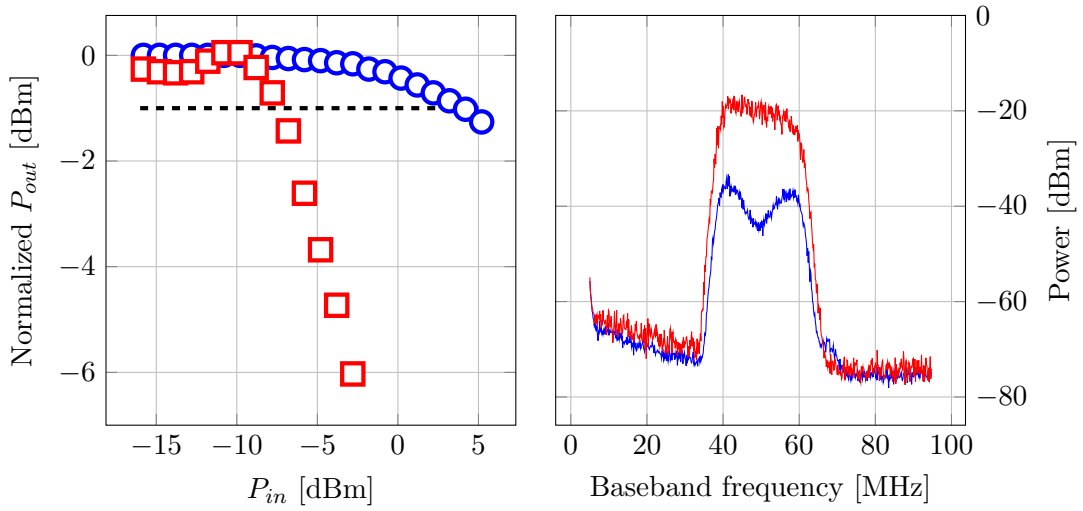

FIGURE 4.11: a) AUX in-band gain compression with a 20 MHz QPSK modulated signal versus input power and (b) baseband spectra with (blue) and without (red) active BRF.

average attenuation of 18 dB over the signal bandwidth and the P_{1dB} is equal to 4 dBm, as shown in Fig.4.11.

The in-band gain and NF were measured versus RX frequency for a fixed $f_{TX} = 800$ MHz (Fig.4.12a). The NF is nearly constant at 6.8 dB and the gain is 29.6 dB. Keeping constant the RX frequency ($f_{RX} = 1.95$ GHz), the TX frequency was swept between 0.7 and 2 GHz. The simulation results with ideal TX clock divider show a constant NF and gain around 6.2 and 30 dB, respectively. However, the effect of the reduced duty cycle at high frequencies degrades both NF and gain measurements. In fact, NF goes from 6.2 to 9.6 dB and the gain varies between 30 and 27 dB.

The measured and simulated NF degradation due to a blocker at f_{TX} is reported in Fig.4.13. To perform this measurement, SAW filter and duplexers were used to filter out the generators noise floor. With $f_{TX} = 950$ MHz and $f_{RX} = 1.05$ GHz, the NF degrades by only 1.1 dB when the blocker power reaches 5 dBm thanks to the conservative design of the clock generation circuits. In a fully integrated solution, the BRF would be clocked with the same noisy LO as the TX. Based on the analysis in [40], it is easy to show that this introduces an additional noise due to the reciprocal mixing in the BRF that will not be cancelled in the digital domain. Considering f_{TX} between 1 and 2 GHz, with the Class-B oscillator proposed in [41] for a power of 10 mW, a phase noise below -173 dBc/Hz at 50 MHz offset is expected. With reference to Fig.3.3, this contribution would increase ΔNF_{RX} by 0.7 dB at $P_{TX} = 23$ dBm.

Finally, the measured LO leakage is shown in Fig.4.14a: thanks to the active stage in front of the BRF, the LO leakage coming from the downconversion mixer at the RX

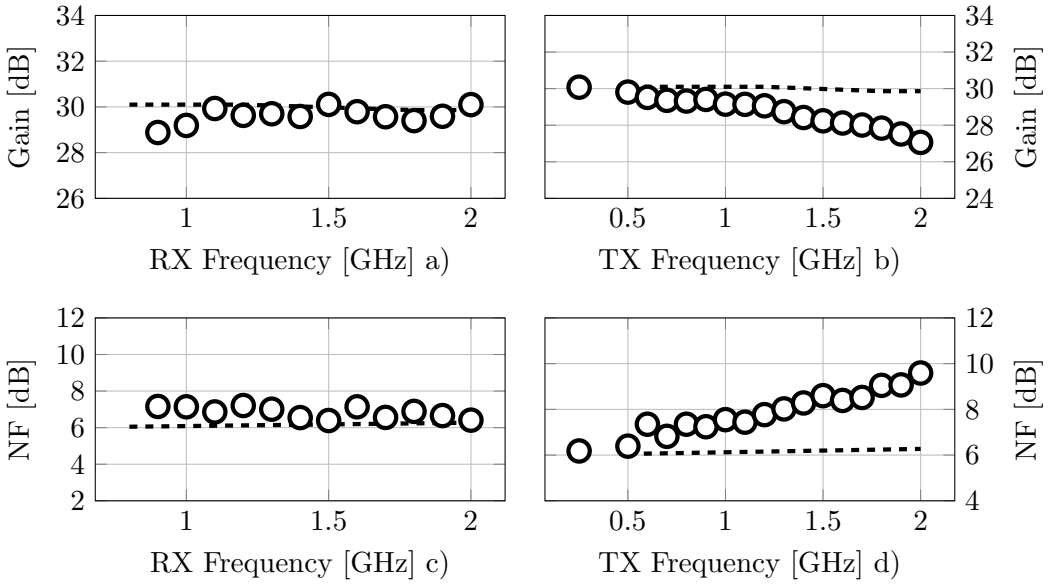

FIGURE 4.12: Measured (dots) and simulated (dashed lines) gain and NF versus f_{RX} for fixed $f_{TX} = 0.8$ GHz (a,c) and versus f_{TX} with $f_{RX} = 1.95$ GHz (b,d).

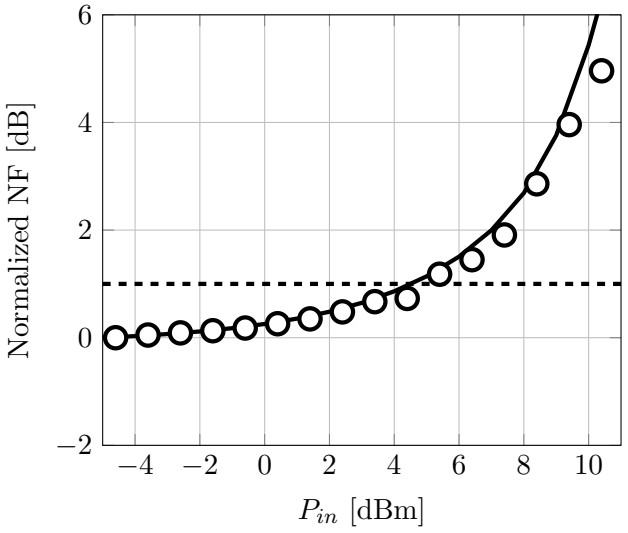

FIGURE 4.13: Simulated (continuous line) and measured (circles) NF degradation versus CW blocker power.

frequency remains always below -90 dBm while the N-Path LO is kept below -80 dBm. Fig.4.14b reports an example of a spectrum with $f_{RX} = 1.91\,GHz$ and $f_{TX} = 1.99\,GHz$.

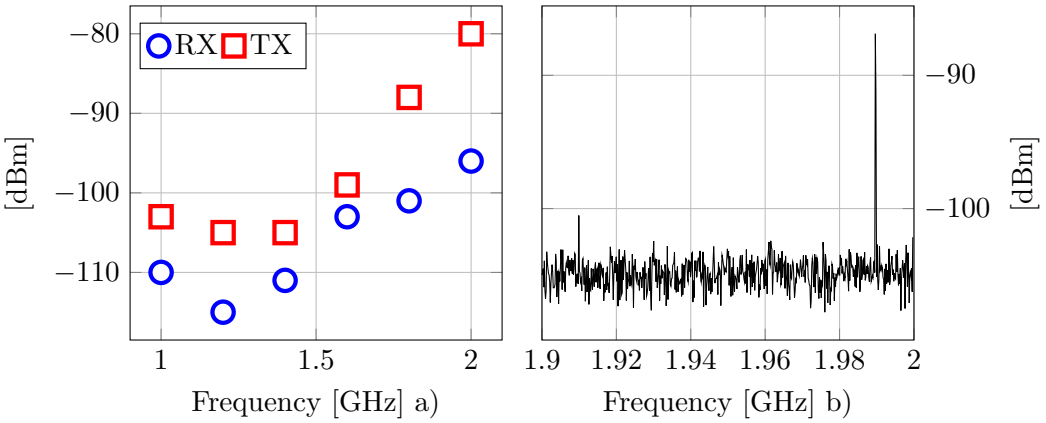

FIGURE 4.14: a) Measured LO leakage vs RX/TX LO frequency and b) measured spectrum with $f_{RX} = 1.91\,GHz$ and $f_{TX} = 1.99\,GHz$.

4.4 Digital Noise Reduction Performance

4.4.1 Measurement Setup

The block diagram of the complete system measurement setup is shown in Fig.4.15. The diversity and auxiliary receiver prototype chips are bonded on two dedicated printed circuit boards (PCBs), and they are biased through a National Instrument CRio-9014. A HP ESG-400A signal generator provides the RX clock to both chips while an Anritsu MG3692A signal generator is used for the TX clock. A QPSK/16-QAM 20 MHz modulated RX signal is produced through a R& S SMU 200A Vector Signal Generator and the broadband white noise is generated through a HP 364B noise source. The coupling between the antennas is emulated using a delay line that provides a group delay of 2-3.2 ns in the frequency range between 1 and 2 GHz. The output of the diversity and auxiliary receiver is connected to the input of two separate PCBs that are used to implement additional filtering and analog-to-digital conversion. Each board includes two fourth-order Butterworth low-pass filters (one for I and one for Q path) implemented with off-the-shelf components and two commercial 10-bit ADC (Analog Devices AD9215). Finally, the DNR algorithm is implemented on a Cyclone IV EP4CE115F29C7 Altera FPGA, which also provides the clock for the ADCs. The processed data are then acquired from the FPGA through the SignalTap II logic analyzer tool of Quartus.

4.4.2 Measurement Results

To test the digital algorithm performance, a broadband white noise source is used and its output is sent to both receivers, as shown in Fig.4.15. For this preliminary test, the RX signal generator is disconnected, meaning that in the RX band only the TX noise

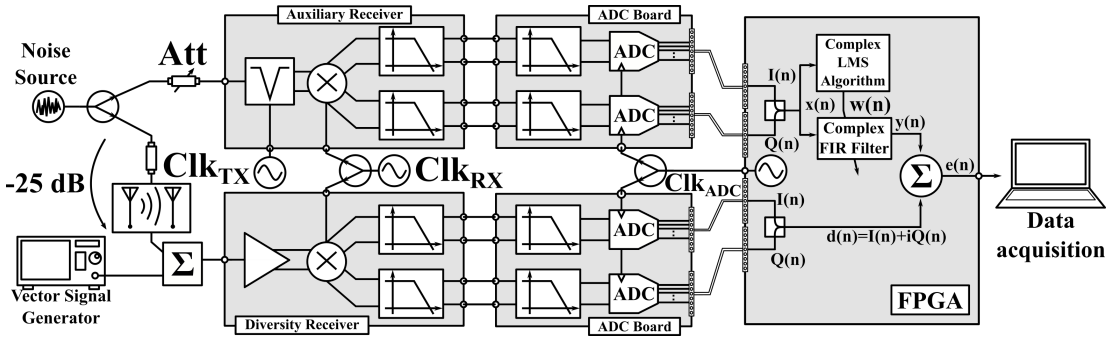

FIGURE 4.15: Complete system measurement setup ([33] ©2018 IEEE).

is present. The RX LO frequency (f_{RX}) is set to 1.2 GHz and the TX frequency (f_{TX}), driving the active BRF in the auxiliary receiver, to 1.1 GHz. In the band of interest ($\pm$10 MHz around f_{RX}), the delay line used to emulate the coupling between the antennas provides a group delay of 3.2 ns and an attenuation of 2 dB. To reproduce the nominal $ISO_{TX-RX} = 25$ dB, the remaining attenuation is obtained through RF broadband attenuators between the noise source and the RX. With a TX noise power spectral density $PSD_{TXn} = -153$ dBc/Hz, the diversity receiver NF degradation ΔNF_{RX} is first measured when the DNR is turned off. The measurement results are reported in in Fig.4.16 and reveal that, with a TX noise power spectral density referred to the RX input $PSD_{TXn,RX} = -130$ dBm/Hz, corresponding to a TX power of 23 dBm, the diversity NF is degraded by almost 13 dB, which is in good agreement with the simulated and computed value. The theory and simulations developed in Chapter 3 suggest that, with a delay in the order of 3 ns, the resulting DNR is around 30 dB, meaning that the TX noise is strongly suppressed and it is reduced below the RX noise floor. Therefore, we expect that most of the contribution to ΔNF_{RX} comes from the AUX. Both computation and simulation predict that the dynamic range of the auxiliary path should be sufficiently high to give a ΔNF_{RX} of only 1 dB when the TX is referred to a full TX signal. The measurements are reported in Fig.4.16 and follow the computed and simulated values very well. The spectra of the output baseband signals with and without the noise reduction at full TX power are shown in Fig.4.17: the TX noise power is uniformly reduced within the bandwidth restoring the RX sensitivity.

It is interesting to notice that, increasing PSD_{TXn}, the NRs in the RX and AUX side increase by the same amount, keeping their ratio (NR_{RX}/NR_{AUX}) constant. Therefore, the additional NF_{RX} degradation comes only from the residual TX noise after the cancellation, as per Eq.(3.3). Moreover, given the good DNR achievable, this is not the dominant component and its effect on the final degradation is limited. This was verified experimentally increasing the TX noise level, as shown in Fig.4.18, and noticing that the performance of the system degrades by 1 dB only when the PSD_{TXn} reaches -144 dBc/Hz. This result can be further improved increasing the LPF order or the ADC

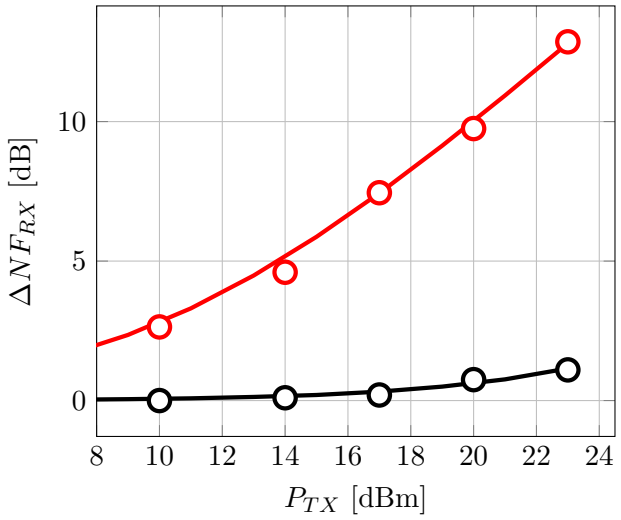

FIGURE 4.16: Simulated (continuous line) and measured (circles) NF_{RX} degradation vs transmitter power with (black) and without (red) DNR.

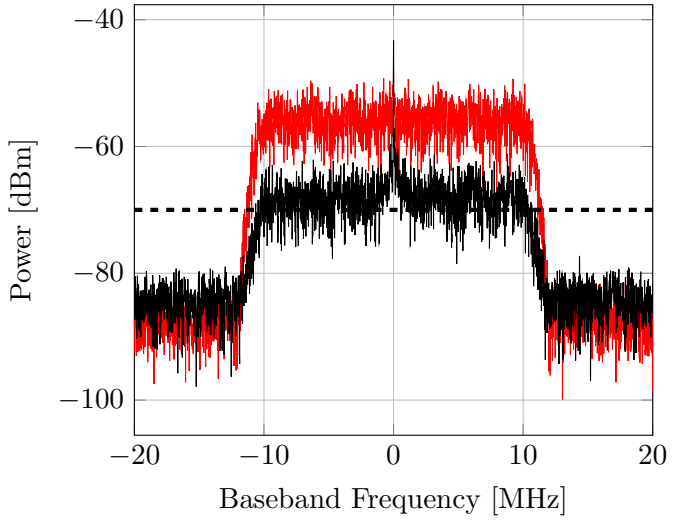

FIGURE 4.17: Measured baseband spectra with (black) and without (red) DNR with full power TX. The dashed line is the standalone RX noise floor.

sampling frequency as explained in Chapter 3. To test the convergence time of the proposed adaptation algorithm, a white noise with PSD equal to -148 dBm/Hz referred to the RX input was used. Fig.4.19 shows the time waveforms of the output baseband signals. At $t = 0$ the DNR is turned on and in few microseconds the output power is near the final value. This is more than enough to track the antenna variations, occurring on a time scale of milliseconds [27, 42]. The tracking mechanism of the algorithm was also tested modifying the $|ISO_{TX-RX}|$ value to emulate a change in the environmental condition. In Fig.4.20 the time waveform of the output signals when at $t \approx 350\,\mu s$ the coupling is changed by 3 dB are shown: also in this case, the LMS algorithm updates the filter coefficients in few microseconds, restoring the RX sensitivity.

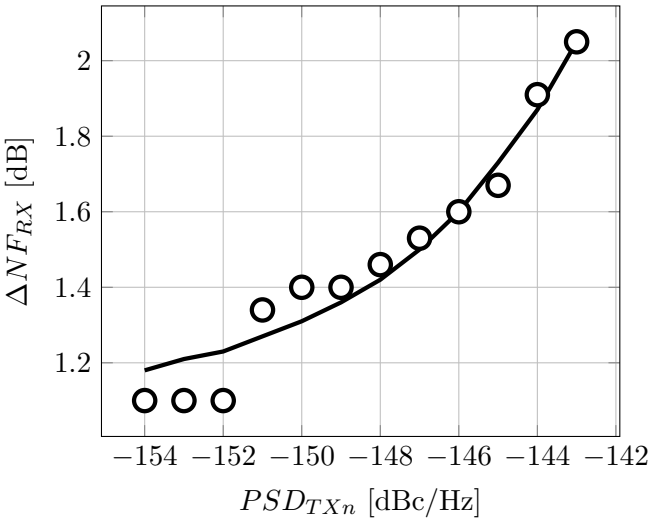

FIGURE 4.18: Simulated (continuous line) and measured (circles) NF_{RX} degradation vs transmitter noise power.

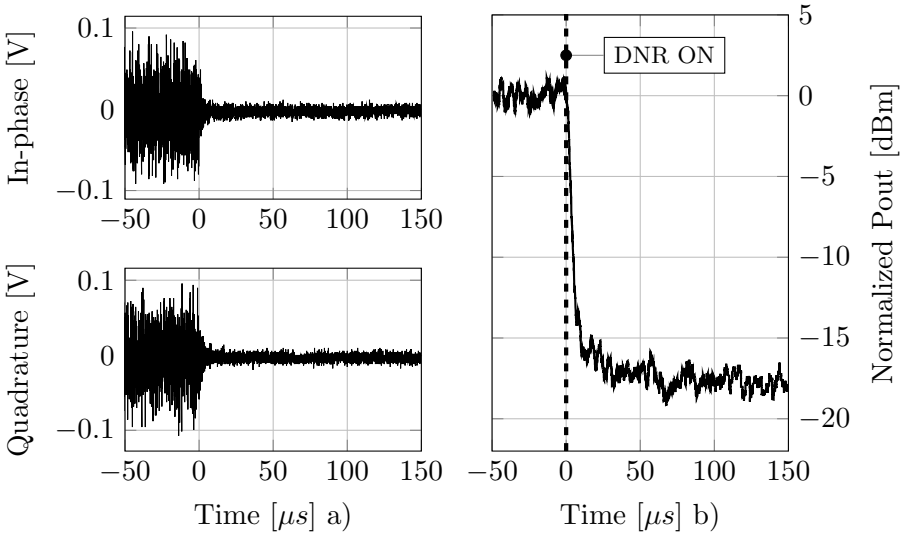

FIGURE 4.19: Baseband signals time waveforms (a) and normalized output power (b). At t=0 DNR algorithm is turned on, converging in few μs

The vector signal generator is then used to produce a 20 MHz QPSK modulated signal emulating a wanted RX signal coming into the diversity RX. Since it is completely uncorrelated with the TX noise that falls in the same band, the LMS algorithm should be able to find the correct coefficients to reduce the TX interference without degrading the wanted signal. This is experimentally demonstrated injecting a -82 dBm 20 MHz QPSK modulated signal at the RX input [3] together with a noise power spectral density of -156 dBm/Hz[4], as shown in Fig.4.15. Without the equalization process, the RX signal is almost completely covered by the TX noise and its constellation is shown in Fig.4.21a. When the algorithm is turned on, the signal can be correctly demodulated

[3]The RX noise level is -95 dBm.

[4]It correspond to an in-band TX noise power of -83 dBm.

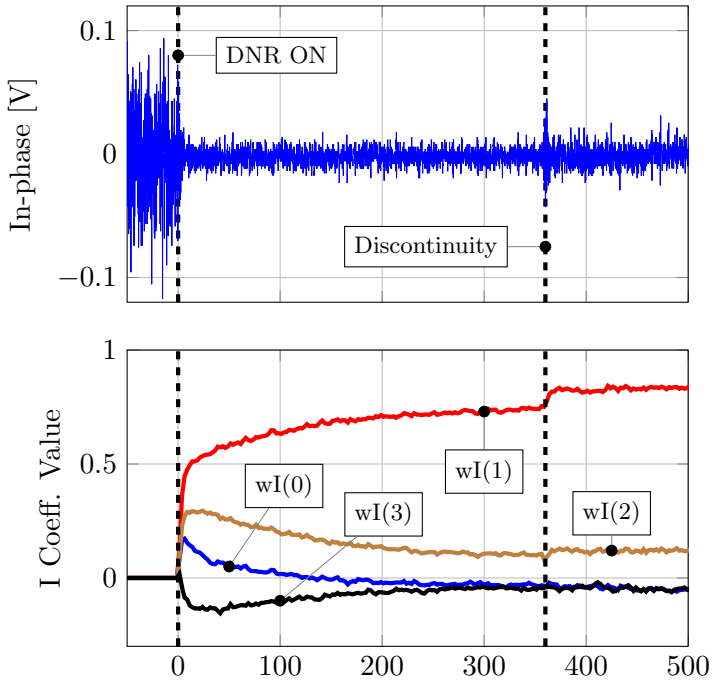

FIGURE 4.20: Time waveforms of the baseband signals and real FIR coefficients. At $t = 350\mu s$, the ISO_{TX-RX} is changed by 3 dB.

with a measured Modulation Error Ratio (MER) of 12 dB. Finally, the same test was performed with a -77 dBm 16-QAM modulated signal, as shown in Fig.4.21c) and (d), with a measured MER of 17 dB.

A challenging aspect that has not been addressed in this work is the selectivity requirement. The TX leakage reaching the RX/AUX is in the order of -20/-15 dBm after the SIC/BRF. In our implementation, only a single real pole was integrated in each receiver, which is not enough to achieve sufficient selectivity. An efficient solution to this problem is to merge the anti-alias filter into an oversampling ADC architecture. Sufficient selectivity and DR to to withstand OOB blockers as high as -20 dBm while dissipating only 8 mW has been reported in [43]. Notice that the same level of filtering that preserves sensitivity also ensures that the DNR algorithm will not be impacted by the TX signal leakage.

A comparison with other SIC receivers is reported in Table 4.1. Considering the receivers with the RF cancellers, this work achieves lower power dissipation and equal or better noise figure. When the TX noise leakage is considered, the proposed system outperforms [44], that is the only SIC receiver that reports dual-band TX leakage cancellation. Very good IB IIP3 and effective IIP3 were achieved, as shown by the improved SI-to-noise and distortion ratio (SINDR)[45]. Effective OOB IIP3, which is comparable to [18], is limited by canceller non-linearity. However, simulation results indicate that

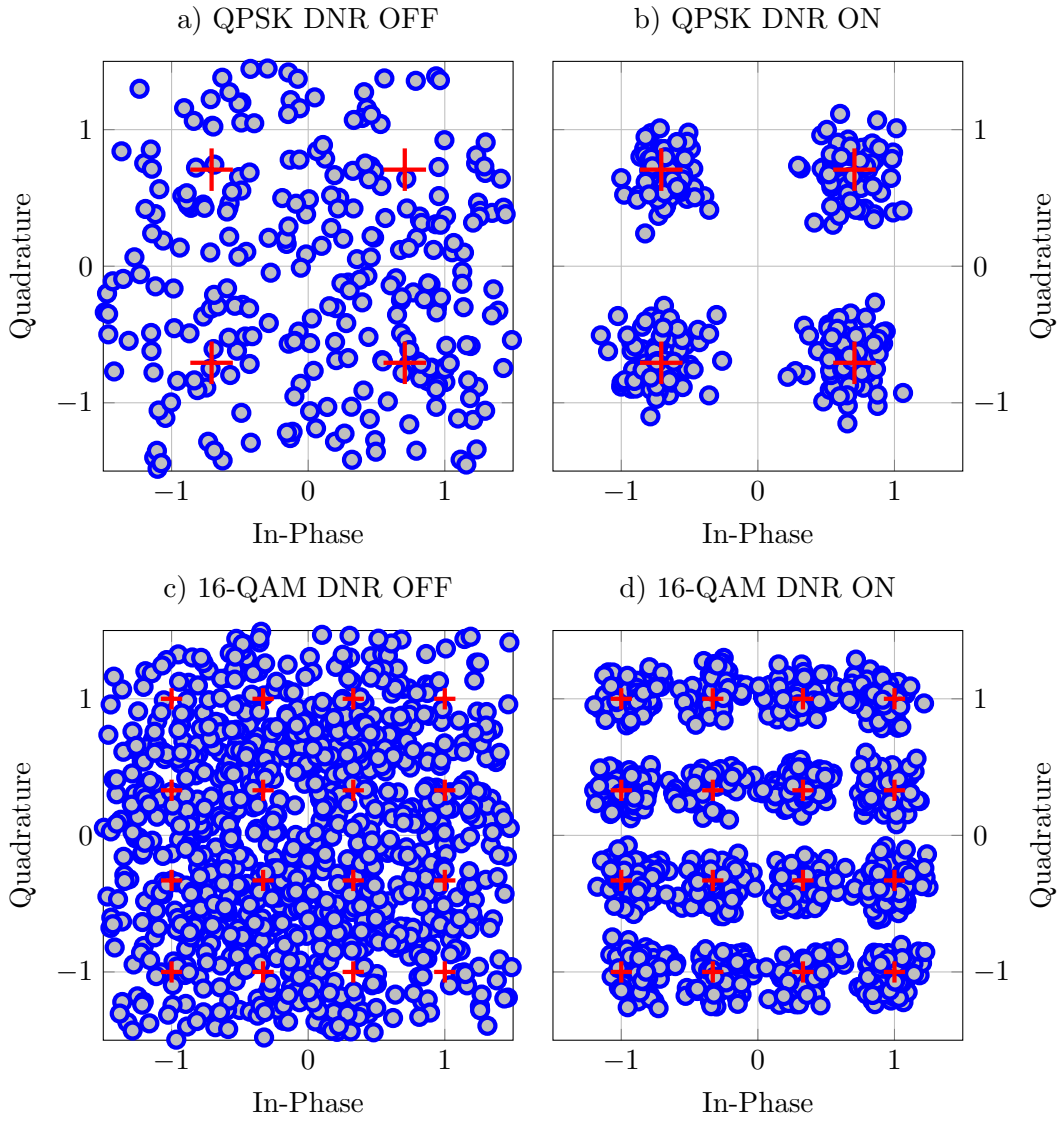

FIGURE 4.21: Measured 20 MHz QPSK and 16-QAM modulated signal constellation with and without TX noise reduction.

an improved canceller grounding scheme could boost the effective OOB IIP3 up to 35 dBm. Finally, area occupation is reduced compared the other works.

		This Work [33]		**JSCC'14 [44]**		**JSCC'15 [18]**		**JSSC'15 [45]**
Architecture		**RF SIC + Aux RX**		Active Two-Point Cancellation		Wideband SIC RF Equalization		Mixer-First RX +SIC VM
FDD/FD		**FDD**		FDD		FDD	FD	FD
Antenna Interface		**Antenna pair**		Ant. pair	1 Ant. + duplexer	1 Ant. + duplexer	Ant pair	Antenna pair
CMOS Tech.		**28 nm**		65 nm		65 nm		65 nm
Frequency [GHz]		**1-2**		0.3-1.7		0.8-1.4		0.15-3.5
RX Gain [dB]		**35**		N/R		27-42		24
NF w/o SIC [dB]		**4-5**		4.2-5.6		4.2-5.8		6.3
NF Degradation with SIC [dB]		**SIC**	**Aux.**	<0.8		0.6	1.1-1.3	4-6
		0.4-0.8	**1**					
IIP3 OOB [dBm]		**+18**		+12		+17		+22
Eff. IIP3 OOB [dBm]		**+25/+29**		+33		+25/+27		N/R
IIP3 IB [dBm]		**+9**		N/R		-20		+9
Eff. IIP3 IB [dBm]		**+25**		N/R		+2		+21.5
SINDR [dB]		**+78**		N/R		+62.5		+71.5
SI Canc.	**Canc [dB]**	**>20**		N/R	20	20	20	21
	BW [MHz]	**15**		N/R	1-7	24	25	16
Ext. Iso TX-RX	**Mag [dB]**	**25**		30	41-51	30	35	25
	Del [ns]	**3**		2-4	20	<11	5-9	4
Max IB TX Leak. [dBm]		**-5**		N/R		-8		+1.5
Max TX Power [dBm]		**+23**		N/R		N/R		N/R
TX Noise Reduction [dB]		**29**		13		N/R	N/A	N/A
Max OOB TX Leak. [dBm]		**0**		+2		-4		N/A
Power [mW]	**RX**	**32-40**		74.6-83		63-69		22-46
	Canc.	**SIC**	**Aux.**	13-72		91/path		10
		0	**24-64**					
Area [mm^2]		**0.63**		1.2		4.8		2

TABLE 4.1: Performance comparison with the state of the art ([33] ©2018 IEEE).

Chapter 5

Conclusions

The 4G LTE standard sets hard constrains on the RX capability to receive a weak signal in presence of strong external interferers. To fulfill these requirements, in the typical implementation of a mobile communication system SAW-based duplexers and filters are used to filter out unwanted out-of-band emissions and interferers. However, their off-chip bulky structure, lack of tunability and high cost are in contrast with the demand of flexibility of modern standard. Removing them means that not only interferers coming from external environment reach unfiltered the receiver input, but also that, in Frequency Division Duplexing (FDD) systems, a strong TX leakage can degrade the receiver performance . While the main TX modulated signal degrades the RX sensitivity due to the limited RX linearity and reciprocal mixing effects, TX broadband noise directly falls into the RX band. Isolation in the order of 15-25 dB with a group delay of 2-3 ns is experimentally measured between two Planar Inverted F-Antennas (PIFAs). With this setup, conventional Self-Interference cancelling techniques fail to cover large bandwidths, limiting the cancellation over only a single channel. In the proposed solution, a highly linear diversity receiver is aided by a passive RF Self-Interference Canceller (SIC) that reduces the main TX signal leakage power at the receiver input. The passive SIC works as a vector modulator sensing the TX signal at the PA output and injecting its copy properly attenuated and phase shifted at the RX input. Due to its broadband working principle, it is effective only over the TX channel, leaving the TX broadband noise in the RX band. For this reason, an auxiliary receiver followed by a dedicated Digital Signal Processing (DSP) is implemented to reduce the TX noise leakage power through the process called Digital Noise Reduction (DNR). To increase the dynamic range of the auxiliary path, an N-Path filter is embedded in the first stage, reducing the main TX signal power and relaxing the requirements of the auxiliary LO and baseband stage. A digital Finite Impulse Response (FIR) filter equalizes the TX noise at the output of the two receivers and subtract the AUX output from the RX

one thus reducing the TX noise leakage power. A Least-Means Square (LMS) algorithm updates the FIR coefficients over time avoiding RX performance degradation due to changes in the environmental conditions.

The two receivers were fabricated in 28 nm TSMC CMOS technology while the DNR algorithm was implemented on FPGA for real-time testing. The standalone diversity receiver has a Noise Figure (NF) of 4-5 dB and an out-of-band IIP3 of 18 dBm. The RF SIC, reducing the TX leakage power at the receiver input, is able to boost the receiver IIP3 to 25-29 dBm depending on the frequency spacing and with a proper grounding scheme the IIP3 could have been increased up to 35 dBm, meeting the LTE requirements with 25 dB of isolation between the antennas. The degradation of the NF introduced by the SIC is around 0.8 dB depending on the coupling phase. Due to the high dynamic range of the auxiliary path, the DNR algorithm is able to reduce by more than 29 dB the TX noise degrading only by 1 dB the receiver NF when the TX is working at full power (23 dBm). The strong TX noise reduction provided by the auxiliary path allows also to relax the TX broadband noise specification: in fact, with a TX noise power spectral density of -144 dBc/Hz, the RX NF is degraded by only 1.8 dB.

Appendix A

Group Delay Quality Factor

The transfer function of a generic second-order bandpass filter can be written as:

$$H(S) = k\frac{s}{s^2/\omega_0^2 + s/\omega_0 Q + 1} \tag{A.1}$$

where ω_0 is the resonance frequency, k is the gain and Q is the filter quality factor. Knowing that $s = j\omega$, the phase can be easily computed as:

$$\Phi = \frac{phi}{4} - atan\frac{\omega/\omega_0 Q}{1 - \omega^2/\omega_0^2}. \tag{A.2}$$

Since the group delay (τ) is defined as minus the derivative of the phase with respect to the frequency, from Eq.(A.2) it can be computed as:

$$\tau = \frac{1}{\omega_0 Q} \cdot \frac{1 + \frac{\omega^2}{\omega_0^2}}{1 - \left(1 - \frac{1}{2Q^2}\right)\frac{2\omega^2}{\omega_0^2} + \frac{\omega^4}{\omega_0^4}} \tag{A.3}$$

Since the cancellation is performed only over a limited frequency range around the resonance frequency, the equation can be further simplified considering $\omega \approx \omega_0$. Under this assumption, the group delay τ_0 can be written as:

$$\tau_0 = \frac{2Q}{\omega_0}. \tag{A.4}$$

Eq.(A.4) provides an easy relationship between the group delay and the quality factor.

Appendix B

N-Path Filters

B.1 Introduction

The idea of the N-Path filters was first proposed in 1960 [46] but only with modern CMOS technology the interest grows due to the fact that their operating frequency increases from kHz to GHz. The main idea is that a filter in baseband can be translated to high frequency by means of frequency mixers. Fig.B.1 and Fig.B.2 show two different block diagram of ideal N-Path filters : a generic filter with transfer function H(f) is placed in between two mixers clocked at f_{LO} frequency. Lets consider the first scenario (Fig.B.1), where H(f) has a low pass (LP) shape. If a sinusoidal signal is fed at the input of the system at frequency f_{in} which is equal (or near) the LO frequency (blue tone in figure), it is down-converted by the first mixer around DC, goes unfiltered through the LP filter and finally is up-converted by the second mixer at f_{in}. On the opposite, if f_{in} is far from the LO frequency (red signal in figure), after the first down-conversion the sinusoidal signal is filtered by the LP filter and then up-converted by the second mixer. This means that if the RF frequency response of the complete chain is considered, a

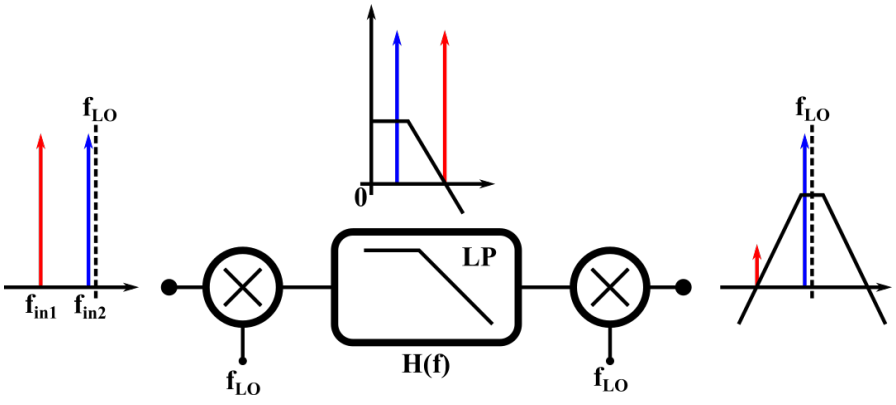

FIGURE B.1: Block diagram of ideal band-pass N-Path filter.

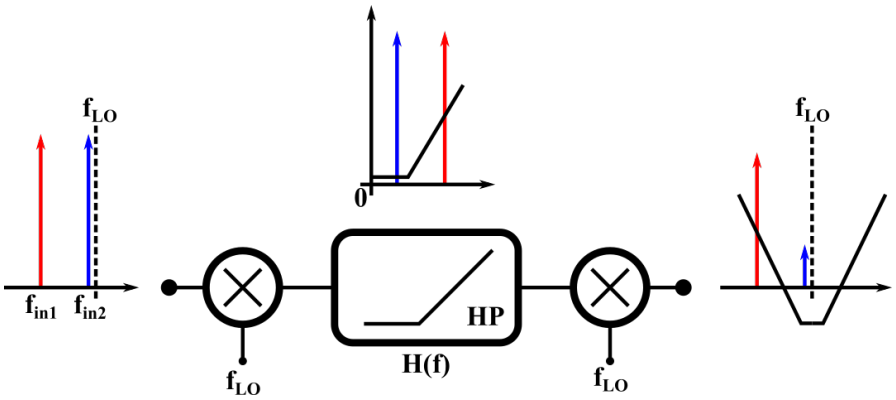

FIGURE B.2: Block diagram of ideal band-stop/notch N-Path filter.

band pass shape is obtained through the use of a simple LP filter. In a similar way, the second scenario where H(f) has an high pass (HP) shape can be analyzed (Fig.B.2). In this case, the signal is filtered only when its frequency is near the LO one, obtaining a complete transfer function with a notch at the LO frequency. From this simplified analysis, few points can be intuitively understand:

- the center frequency of the band-pass/notch filter is determined by the LO frequency of the mixers, making them easily tunable;
- the RF bandwidth is determined by the baseband filter one and, since the baseband cut-off frequency is typically much smaller than the LO one, the quality factor of the filter is high.

The typical implementation of the band-pass N-Path filter is shown in Fig.B.3a[47] where the baseband LP filters are implemented with RC networks and the mixers through NMOS switches (i.e. passive mixers). Defining with N the number of parallel path, it is important to notice that each switch is driven by one of the N non-overalpping phases of the clock signal (Fig.B.3e). The filter can be arranged in a slightly different way simplifying its structure: the resistors can be moved outside the switching section because they are memory-less elements and since only one path is active at time, only one resistor can be used. Another simplification can be applied to the switches: if the two set of switches (SW_A and SW_B in Fig.B.3a) are driven by the same clock phases, the function of the second set can be implemented by using only the first one. Therefore, the final circuit is the one shown in Fig.B.3b. Obviously, also the band-stop N-Path filter can be implemented and it is shown in Fig.B.3c[7]. Following the same procedure applied before, this implementation can be simplified obtaining the one in Fig.B.3d. The main difference between the two is the way the output signal is sensed: in the band pass case, the output voltage is the voltage drop across the capacitors while in the other case

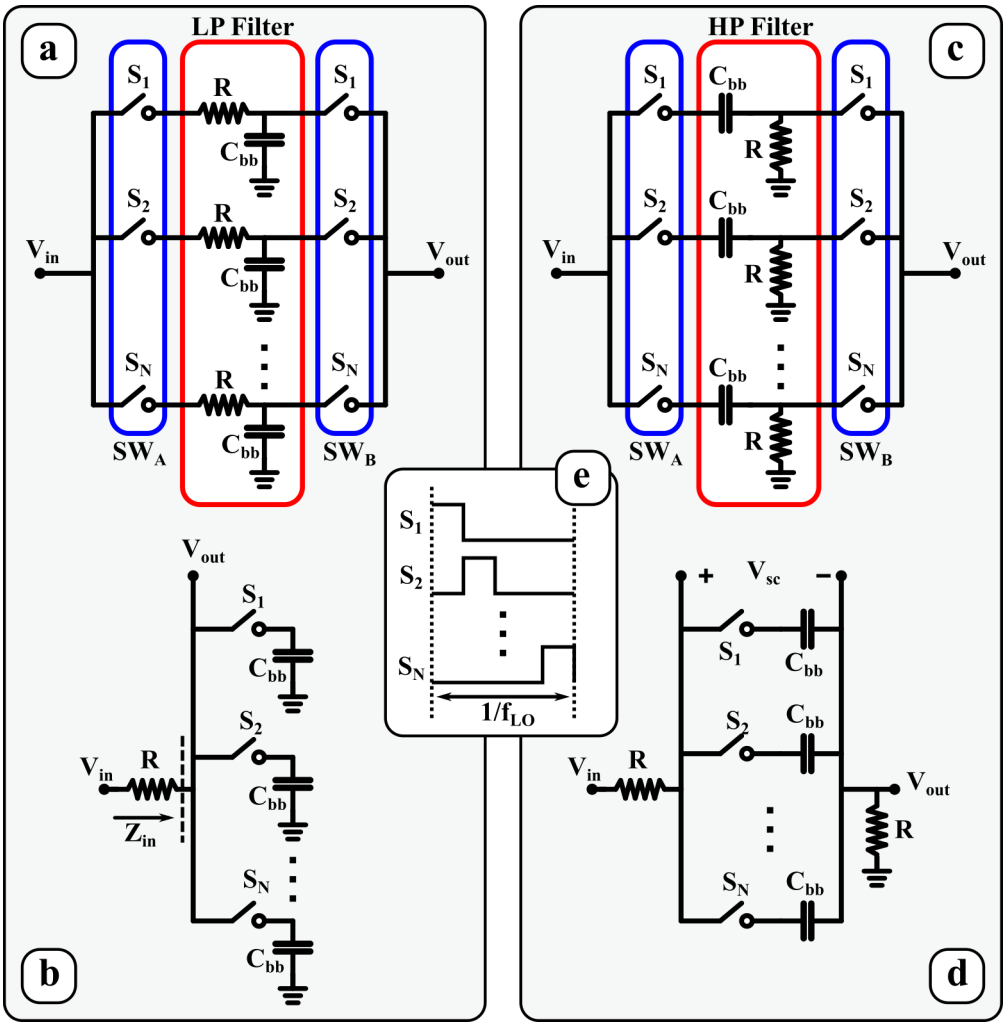

FIGURE B.3: Band-pass (a and b) and band-stop (c e d) N-Path filter implementation through RC network and passive mixers. Clock phases driving the N-Path switches (e).

the output voltage is the current that flows through the baseband capacitors multiplied by the value of the resistor R.

From this explanation, the effect of the number of phases N is not clear. To clarify this point, lets consider the schematic of band-pass filter in Fig.B.3b. If a sinusoidal signal at frequency $f_{in} = f_{LO}$ is applied at the input of the filter, each baseband capacitor sees the same portion of the input signal every time it is turned on. Since the switching frequency is much larger than RC cutoff frequency, the voltage on the capacitor is the average (i.e. integral) of the input signal in the time interval the dedicated switch is turned on[1]. Therefore, the output voltage is the staircase approximation of the input signal (Fig.B.4): the higher the number of phases, the better is the approximation. On the opposite, when the input signal frequency is far from the LO one[2], each baseband capacitor sees a different portion of the signal every time is turned on, leading to an

[1] After initial transient.
[2] Except for the harmonic frequencies.

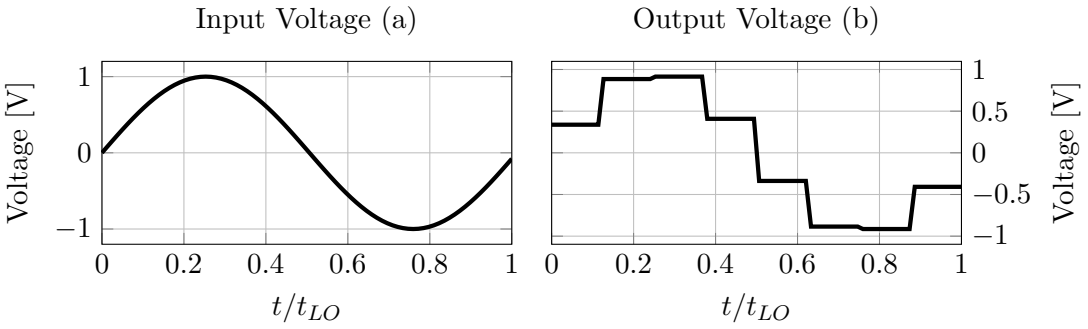

FIGURE B.4: Band-Pass N-Path filter input (a) and output (b) time waveform with $f_{in} \approx f_{LO} = 1/t_{LO}$ over a single clock cycle.

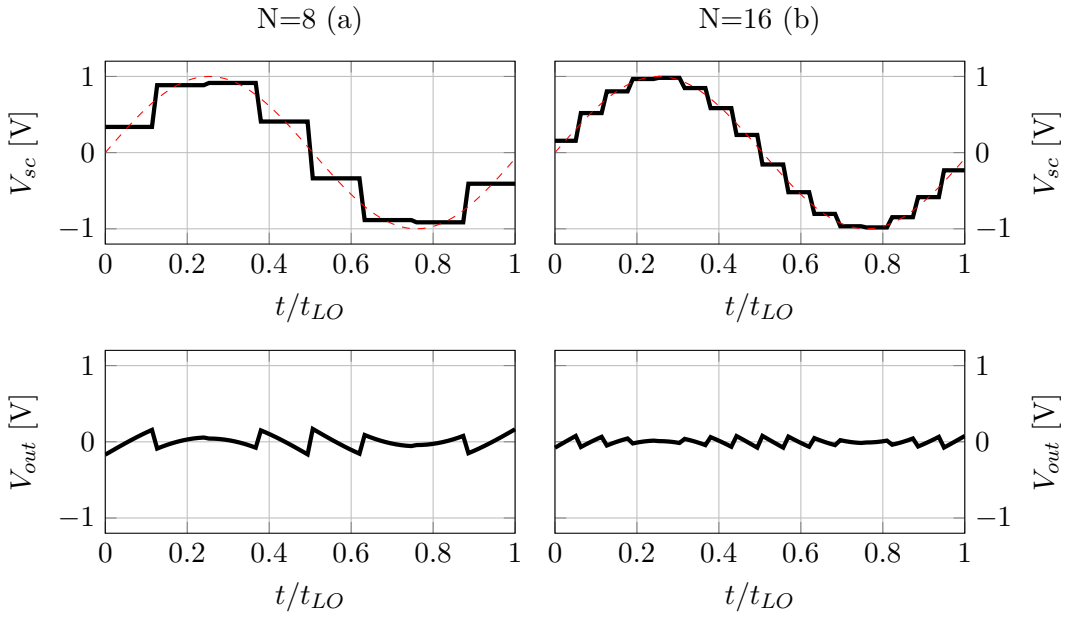

FIGURE B.5: Band-Pass N-Path filter time waveforms with $f_{in} \approx f_{LO} = 1/t_{LO}$ over a single clock cycle in two different cases: a)N=8 and b) N=16.

average equal to zero (i.e. no voltage drop on the baseband capacitors) and to a very low output signal. The same reasoning can be applied to the band-stop N-Path filter with a main difference: this time the output voltage is the difference between the input voltage and the voltage drop on the baseband capacitors ($V_{out} = V_{in} - V_{sc}$ from Fig.B.3). In Fig.B.5 the output signal is shown in the case the input frequency is near the LO one: V_{sc} is the staircase approximation of the input signal while the output signal is strongly attenuated. Fig.B.5 shows the difference between the time waveforms when N=8 and when N=16: the higher the number of phases, the better is the staircase approximation of the input signal and the lower is output voltage (i.e. the difference between the input signal and its sampled version).

Fig.B.6 shows the frequency response of the N-Path filter in band-pass and band-stop configurations. It can be noticed that in addition to the wanted frequency response

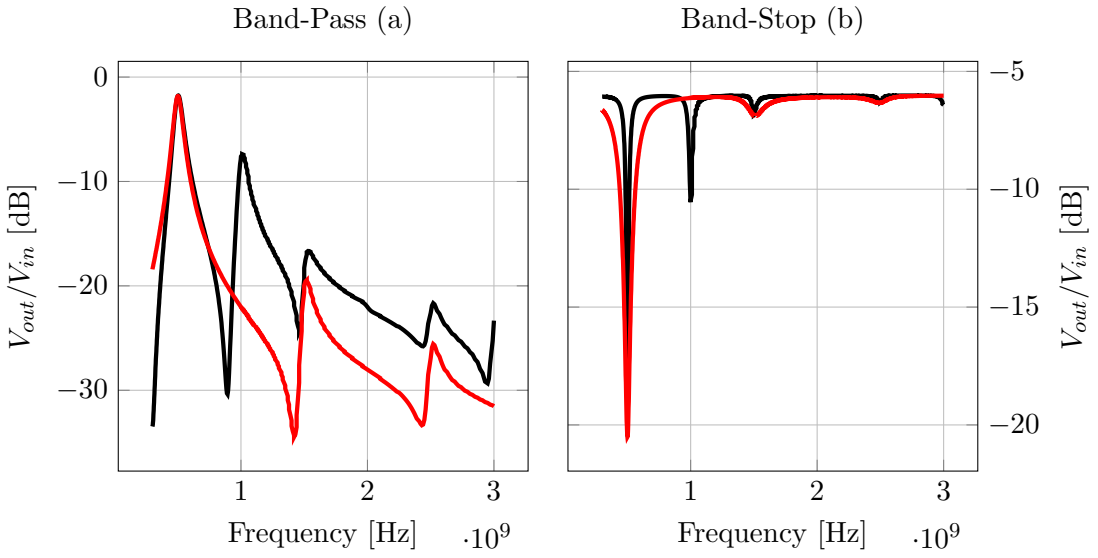

FIGURE B.6: N-Path filter transfer function in (a) band-pass and (b) band-stop configuration for single-ended (black) and differential (red) implementations with $f_{LO} = 0.5$ GHz.

around the first harmonic, the filter presents a band-pass/stop behavior also around the other harmonics. This can be intuitively understand from the fact that if a signal at nf_{LO} (with n=1,2,...) is fed at the input of the filter, each baseband capacitor sees the same portion of the signal each time is turned on in a similar way to the case shown in Fig.B.4 and Fig.B.5. The advantage of a differential implementation is that only the odd order harmonics are presents while the even are suppressed (red curves in Fig.B.6).

B.2 Equivalent RLC Model

In [47] and [7] the mathematical analysis of both implementation is proposed. Considering the band-pass N-Path filter[3] the filter transfer function of the schematico shown in Fig.B.3b is:

$$H_0(f) = \frac{V_{out}(f)}{V_{in}(f)} = \frac{N}{1+jf/f_{rc}} \times \Big(D + \frac{1+exp(j\pi(1-2D)f/f_{LO})}{2\pi f_{rc}/f_{LO}} \times \Big(-\frac{exp(j2\pi Df/f_{LO}) - exp(-2\pi Df_{rc}/f_{LO})}{exp(j\pi f/f_{LO}) + exp(-2\pi Df_{rc}/f_{LO})} \cdot \frac{1}{1+jf/f_{rc}}\Big)\Big) + (1-ND) \quad \text{(B.1)}$$

[3]The computation regarding the band-stop implementation is similar and comes to the same RLC equivalent model.

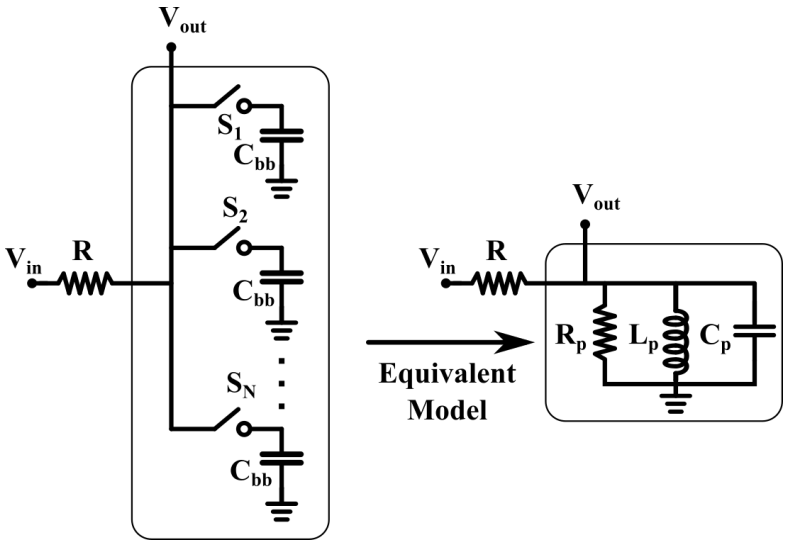

FIGURE B.7: Equivalent N-Path filter model made of a parallel RLC network.

where D is the duty cycle, N is the number of phases, f_{LO} the clock frequency and $f_{rc} = 1/\pi RC_{bb}$. From this complicated expression it is difficult to approach the design of an N-Path filter. However, as shown in Fig.B.7, a much simpler model made of a parallel RLC network was developed [47]. To compute it, lets start from the Eq.(B.1) considering only the frequency response around the harmonics:

$$H_0(nf_{LO}) = \frac{N}{1+\frac{jnf_{LO}}{f_{rc}}} \cdot \left(D + \frac{1+e^{\frac{j\pi(1-2D)nf_{LO}}{f_{LO}}}}{2\pi f_{rc}/f_{LO}} \times \right.$$
$$\left. \times \left(-\frac{e^{\frac{j2\pi Dnf_{LO}}{f_{LO}}} - e^{-2\pi D\frac{f_{rc}}{f_{LO}}}}{e^{\frac{j\pi nf_{LO}}{f_{LO}}} - e^{-2\pi D\frac{f_{rc}}{f_{LO}}}} \cdot \frac{1}{1+\frac{jnf_{LO}}{f_{rc}}} \right) \right) + (1-ND). \quad \text{(B.2)}$$

where n=[1,2,3,...]. Under the assumption that $f_{rc} \ll f_{LO}$ and considering only odd n values[4], the Eq.(B.2) can be further simplified and becomes:

$$H_0(nf_{LO}) = \frac{2N(1-cos(2\pi nD))}{4(\pi n)^2 D} + 1 - ND. \quad \text{(B.3)}$$

With the additional assumption of D=1/N, the last equation becomes:

$$H_0(nf_{LO}) \approx \text{sinc}^2(n/N). \quad \text{(B.4)}$$

This equation defines the harmonic selectivity of the N-Path filter as a function of the number of phases. In other words, it defines the peak gain at the harmonic frequencies of Fig.B.6a. The transfer function can be computed also considering the impedance of the switched portion of the circuit (Z_{in} in Fig.B.3b). The output voltage can be computed

[4]This assumption is true in the differential implementation.

as the voltage divider between R and Z_{in}, obtaining:

$$H_0(nf_{LO}) = \frac{Z_{in}(nf_{LO})}{Z_{in}(nf_{LO}) + R}. \tag{B.5}$$

Rewriting the equation and considering only the first harmonic (n=1) that is where we are interested in developing the simplified model, the N-Path impedance is:

$$Z_{in}(f_{LO}) = \frac{H_0(f_{LO})}{1 - H_0(f_{LO})}. \tag{B.6}$$

Replacing $H_0(f_{LO})$ with Eq.(B.3) the impedance at the LO frequency is [47]:

$$Z_{in}(f_{LO}) = \frac{N\sin^2(\pi D) + (1 - ND)D\pi^2}{N((D\pi)^2 - \sin^2(\pi D))} \cdot R = R_p \tag{B.7}$$

The interesting result is that the impedance of the N-Path filter at the LO frequency is purely resistive and it depends on the number of phases N, on the duty cycle D and on the driving impedance R. The parallel resistor R_p is the first element of the equivalent RLC parallel network that models the N-Path filter around the LO frequency (Fig.B.7). To find the other two components, lets consider the transfer function of the equivalent RLC model of Fig.B.7:

$$H_{RLC}(s) = \frac{s/RC_p}{s^2 + (R_p + R)/(R_pRC_p)s + 1/L_pC_p}. \tag{B.8}$$

Setting the denominator equal to zero, the poles are:

$$s_{1,2} = -\frac{R_p + R}{2R_pRC_p} \pm j\frac{1}{2}\sqrt{-\left(\frac{R_p + R}{R_PRC_p}\right) + \frac{4}{L_pC_p}}. \tag{B.9}$$

Equating in the same way the denominator of Eq.(B.1) to zero, the poles of the N-Path filter transfer function can be found as:

$$s = -4\pi Df_{rc} + j(2k + 1)\pi, \qquad k = 0, \pm1, \pm2, ... \tag{B.10}$$

The C_p and L_p values can be computed equating the poles of the model with the one of Eq.(B.10). Considering only the real parts, the equation becomes:

$$-\frac{Rp + R}{2R_pRC_p} = -4\pi Df_{rc}. \tag{B.11}$$

Therefore, the value of the parallel capacitor C_p is [47]:

$$C_p = \frac{R_p + R}{8\pi DR_pRf_{rc}} = \frac{\pi^2}{m(N\sin^2(\pi D) + (1 - ND)D\pi^2)} \cdot C_{bb} \tag{B.12}$$

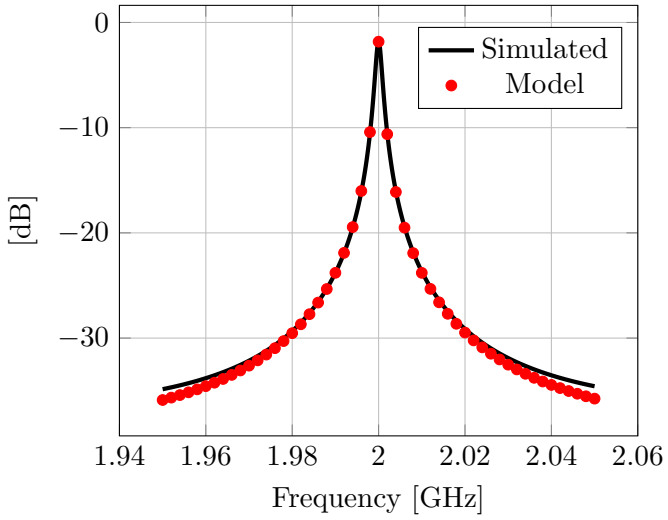

FIGURE B.8: N-Path filter transfer function versus frequency. The circuit parameter used for simulation are: $C_{bb} = 50\,fF$, $R = 1\,k\Omega$, $R_{sw} = 1\,\Omega$, $N = 4$ and $f_S = 2$ GHz. A duty cycle equal to 1/N is used.

where m=2 for the single-ended implementation and 8 for the differential. Also in this case, the value of the parallel capacitor depends on the number of phases, on the duty cycle D and on the value of the baseband capacitor C_{bb}. The last step is to find the L_p value. The easiest way is to make the two resonance frequencies equal solving the equation:

$$\frac{1}{\sqrt{L_p C_p}} = \sqrt{(4\pi D f_{rc})^2 + (2\pi f_{LO})^2}. \tag{B.13}$$

The value of L_p is [47]:

$$L_p = \frac{1}{4\pi^2 C_p (4(D f_{rc})^2 + f_{LO}^2} \approx \frac{1}{(2\pi f_{LO})^2 C_p}. \tag{B.14}$$

From these equations, it can be noticed that the N-Path filter works as an RLC parallel network with a bandwidth that is independent from the LO frequency[5]. In particular, the bandwidth is:

$$BW = \frac{1}{2\pi (R_p || R) C_p} = 4 f_{rc}/N \tag{B.15}$$

and the quality factor Q is:

$$Q = \frac{f_{LO}}{BW} = \frac{N f_{LO}}{4 f_{rc}} \tag{B.16}$$

In conclusion, a comparison between the N-Path filter and the model frequency responses is proposed in Fig.B.8: the model well approximates the filter transfer function around the LO frequency.

[5]It is equivalent to an RLC parallel network with tunable inductor L.

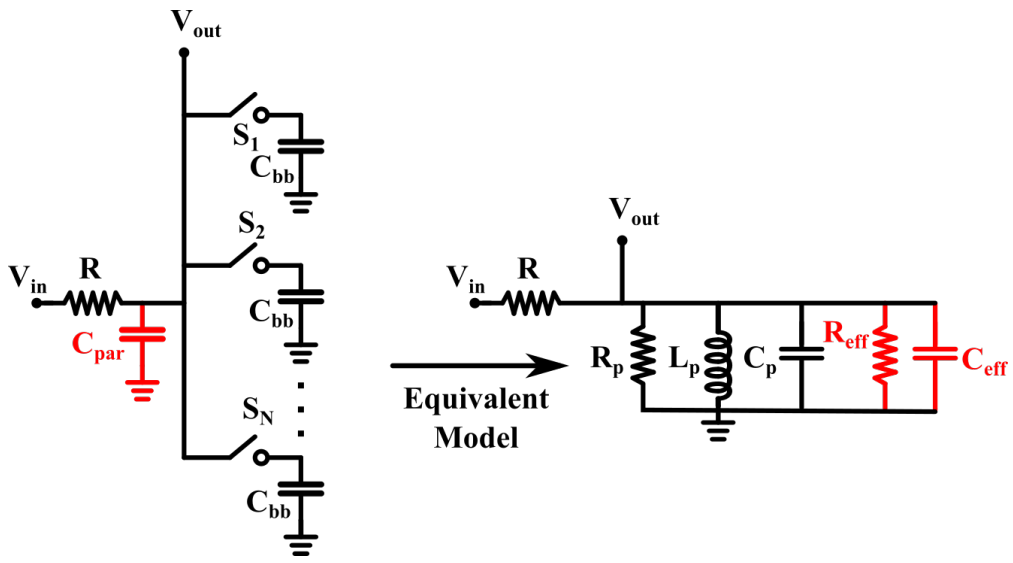

FIGURE B.9: Equivalent RLC model with R_{eff} and C_{eff} modeling the effect of parasitic capacitor C_{par}.

B.3 Parasitic Capacitance Effect

One of the main assumption behind N-Path filter theory is that only one path is active at time. Even if the clock driving the switches consists of N non-overlapping phases, a parasitic capacitor as the one shown in Fig.B.9 degrades the system performance. This capacitor acts as a connection between the paths of the filter sharing its charge between the different baseband capacitors. Its effect can be modeled as a RC network added in parallel to the equivalent model computed in the previous section. The theory behind this model is reported below.

A sinusoidal signal of the type $V_{RF}\cos(\omega_{RF}t)$ is applied at the input of the filter, where ω_{RF} is the signal angular frequency and V_{RF} is its amplitude. The signal can be rewritten as:

$$\begin{aligned} V_{RF}\cos(\omega_{RF}t) &= \frac{V_{RF}}{2}\big(\cos(\omega_{RF}t) + i\sin(\omega_{RF}t) + \cos(\omega_{RF}t) - i\sin(\omega_{RF}t)\big) = \\ &= \frac{V_{RF}}{2}e^{j\omega_{RF}t} + \frac{V_{RF}^*}{2}e^{-j\omega_{RF}t}. \end{aligned} \tag{B.17}$$

Taking into account only the transfer function around the first harmonic, each switch applies to the RF signal the function[6]:

$$H_{sw}(i) = \frac{1}{N}\text{sinc}(1/N)e^{j\left(\omega_{LO}t + \frac{2\pi(i-1)}{N}\right)}, \qquad i = [1, N] \tag{B.18}$$

where i is the path index and the second term in the exponential is added to take into account that each switch is ON in a different phase of each period. Therefore, the voltage

[6] A duty cycle equal to 1/N is assumed to simplify the computation.

on each baseband capacitors C_{BB} is:

$$\begin{aligned} V_b(i) &= \frac{V_{RF}}{2}\left(e^{j\omega_{RF}t} + e^{-j\omega_{RF}t}\right)\cdot e^{j\left(\omega_{LO}t + \frac{2\pi(i-1)}{N}\right)} \\ &= V_b\left(e^{j(\omega_{RF}+\omega_{LO})t} + e^{-j(\omega_{RF}+\omega_{LO})t}\right)e^{\frac{2\pi(i-1)}{N}} \end{aligned} \tag{B.19}$$

where $V_b = V_{RF}\frac{1}{N}\text{sinc}(1/N)$. Considering only a small range around the switching frequency ($\omega_{RF} \approx \omega_{LO}$), the downconverted voltage on the baseband capacitors is [38]:

$$V_b(i) = V_b e^{j\frac{2\pi(i-1)}{N}} \qquad i = [1, N]. \tag{B.20}$$

Knowing that from the first to the Nth phase the parasitic capacitor is charged from V_b to $V_b e^{-j\frac{2\pi}{N}}$, the equivalent baseband current[7] flowing through C_{par} can be computed as:

$$\begin{aligned} I_{bb,Cpar} &= \frac{\Delta Q}{T_S} = C_{par} f_S V_b\left(1 - e^{-j\frac{2\pi}{N}}\right) = \\ &= C_{par} f_S V_b\big(1 - \cos(2\pi/N) + j\sin(2\pi/N)\big) =^{\cdot} \\ &= C_{par} f_S V_b\big(2\sin^2(\pi/N) + j\sin(2\pi/N)\big) \end{aligned} \tag{B.21}$$

The last equation underlines that the equivalent baseband current flowing into the parasitic capacitor has a real and imaginary components. The equivalent admittance shown by C_{par} can be written in a general form as:

$$Y_{bb} = \frac{I_{bb}}{V_b} = \frac{1}{R_{bb}} + jB_{bb}. \tag{B.22}$$

Equating Eq.(B.21) and Eq.(B.22), the equivalent admittance of the parasitic capacitor in baseband can be found as:

$$\begin{aligned} \frac{1}{R_b b} &= 2C_{par} f_S \sin^2(\pi/N) \\ B_{bb} &= C_{par} f_S \sin(2\pi/N) \end{aligned} \tag{B.23}$$

From [38], the impedance shown at baseband frequencies can be referred to the RF N-Path model multiplying each impedance by[8] $\text{sinc}^2(1/N)/N$, obtaining:

$$\begin{aligned} R_{eff} &= \frac{R_{bb}\text{sinc}^2(1/N)}{N} = \frac{N}{2C_{par} f_S} \\ C_{eff} &= \frac{NB_{bb}}{2\pi f_S \text{sinc}^2(1/N)} = \frac{NC_{par}\sin(2\pi/N)}{2\pi\text{sinc}^2(1/N)} \end{aligned} \tag{B.24}$$

[7]The term *equivalent baseband current* refers to the current that flows in the capacitors after being down-converted by the mixer switches.

[8]The division by N is due to the fact that each baseband capacitor is active 1/Nth of the time.

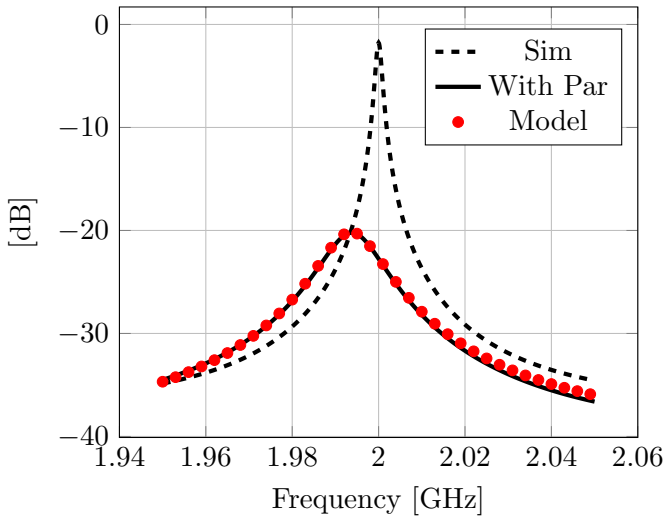

FIGURE B.10: N-Path filter transfer function versus frequency with (continuous line) and without (dashed line) $C_{par} = 1$ pF. The model (red circles) well approximates the effect of the parasitic capacitance.

R_{eff} and C_{eff} model the effect of the parasitic capacitance C_{par} in the equivalent RLC N-Path model and can be added to it as shown in Fig.B.9. It is easy to see that C_{par} introduces two different effects:

- a downshift in the resonant frequency modelled with C_{eff};
- a reduction in the peak amplitude modelled with R_{eff}.

Fig.B.10 shows the effect of the parasitic capacitance on the filter transfer function.

Defining the ideal resonance frequency of the RLC tank as $f_{res,ideal}$[9] and the shifted resonance frequency due to C_{eff} as $f_{res,par}$, the difference between them as a function of C_{par} can be computed. These two can be related as:

$$\frac{1}{L_p C_p} = \frac{\alpha}{L_p(C_p + C_eff)} \tag{B.25}$$

where $\alpha = f_{res,ideal}/f_{res,par}$. Therefore, their ratio is:

$$\alpha = \frac{C_p + C_{eff}}{C_p} = 1 + \frac{C_{par}\sin(2\pi/N)}{2\pi C_{bb}}. \tag{B.26}$$

Finally, the difference between the two frequencies (Δf in Fig.B.11) is:

$$\Delta f = f_{res,ideal} - f_{res,par} = f_S\left(\frac{\alpha - 1}{\alpha}\right) = \frac{f_S C_{par}\sin(2\pi/N)}{2\pi C_{bb}}. \tag{B.27}$$

From the last equation, some considerations can be done about Δf:

[9] Notice that $f_{res,ideal}$ is equal to the switching frequency f_S when no parasitics are present.

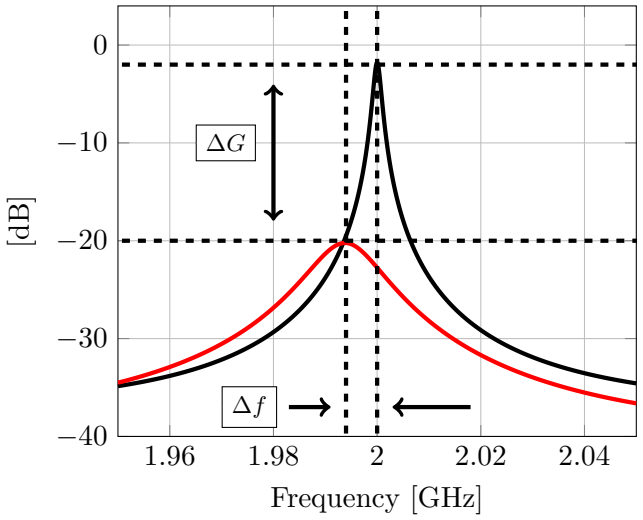

FIGURE B.11

- it increases with the C_{par};
- it decreases as the size of the baseband capacitor increases;
- it increases linearly with the switching frequency.

The same procedure can be applied to compute the gain degradation due to R_{eff}. A gain difference (ΔG in Fig.B.11) is defined as:

$$\Delta G = \frac{R_p}{R_p + R} \cdot \frac{R_p || R_{eff} + R}{R_p || R_{eff}} \tag{B.28}$$

which can be simplified as:

$$\Delta G = 1 + 2RNC_{par}f_S \sin^2(\pi/N). \tag{B.29}$$

From Eq.(B.29), some considerations can be done about ΔG too:

- it degrades when the sampling frequency increases;
- it degrades when the number of phases increases[10];
- it depends linearly on the driving impedance R.

[10]Notice that the gain increases with N, therefore increasing N does not necessary means that the gain is decreasing.

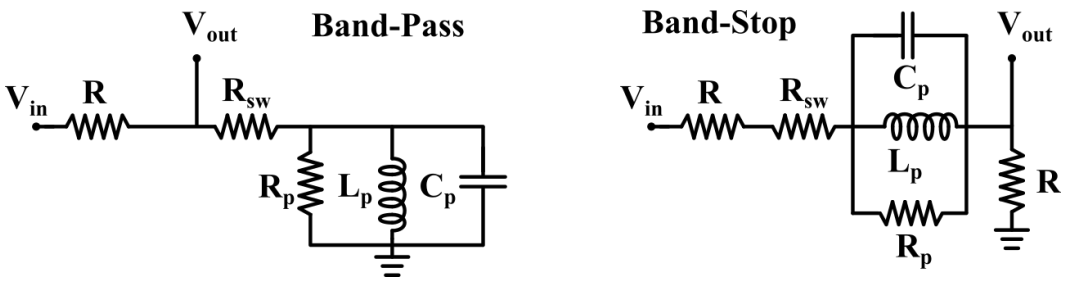

FIGURE B.12: Equivalent RLC model with switch resistance R_{sw}.

B.4 Switch Resistance Effect

Up to now, the switches have been considered ideal (i.e. zero on resistance). In reality, each switch has its own on resistance that can affect the filter response. Since there is always only one active path, only one on resistance is involved in each time instant, allowing to move it in front of the whole filter. To analyze the effect of this non-ideality, it is easier to start from the equivalent models of the filters, adding the switch resistance R_{sw} in series to the parallel RLC equivalent circuit.

The N-Path BP equivalent model with the switch resistance is shown in Fig.B.12. At the LC resonant frequency (i.e. the f_{LO} frequency), the filter transfer function is:

$$\frac{V_{out}}{V_{in}}(f_{LO}) = \frac{R_{sw} + R_p}{R_{sw} + R_p + R} \approx \frac{R_p}{R_p + R} \tag{B.30}$$

under the assumption that $R_p \gg R_{sw}$. This means that its effect at the LO frequency in a band pass filter is negligible. On the contrary, far from the LO frequency, the impedance of the parallel RLC is negligible and the filter transfer function becomes:

$$\frac{V_{out}}{V_{in}}(f \neq f_{LO}) = \frac{R_{sw}}{R + R_{sw}}. \tag{B.31}$$

In this frequency range the switch on-resistance defines the maximum rejection of the band-pass filter, as shown in Fig.B.13a.

For what concern the band-stop N-Path filter, at the resonant frequency the transfer function becomes:

$$\frac{V_{out}}{V_{in}}(f_{LO}) = \frac{R}{2R + R_{sw} + R_p} \tag{B.32}$$

Defining from Eq.(B.7) the factor β as:

$$\beta = \frac{N \sin^2(\pi D) + (1 - ND) D\pi^2}{N((D\pi)^2 - \sin^2(\pi D))} \tag{B.33}$$

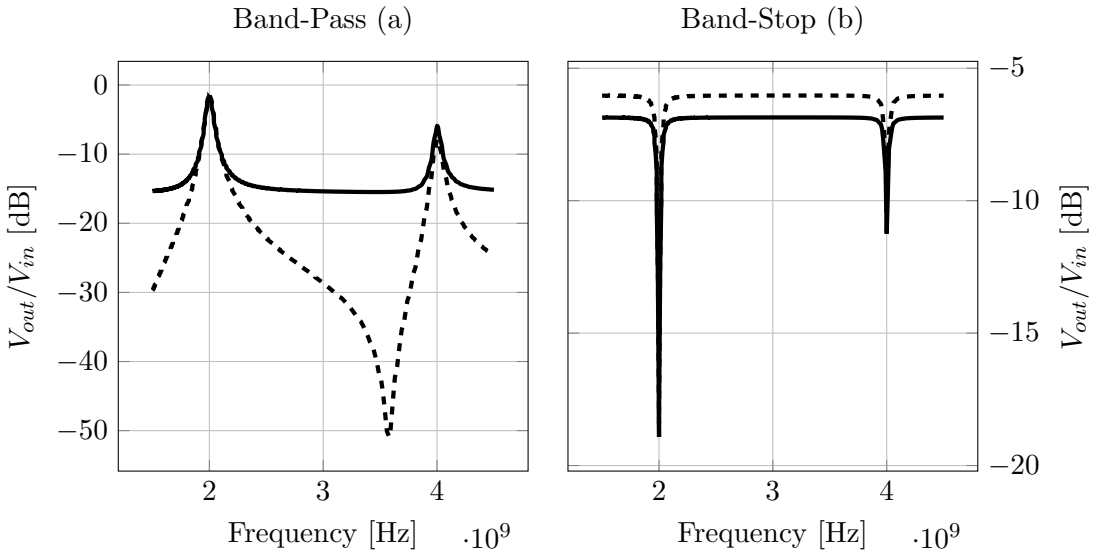

FIGURE B.13: N-Path filter transfer function in (a) band-pass and (b) band-stop configuration with (continuous line) and without (dashed line) switch resistance with $f_{LO} = 2$ GHz.

the resistance R_p is simply the product between this factor and the driving impedance:

$$R_p = \beta(2R + R_{sw}). \tag{B.34}$$

Therefore, Eq.(B.32) is:

$$\frac{V_{out}}{V_{in}}(f_{LO}) = \frac{R}{(1+\beta)(2R + R_{sw})}. \tag{B.35}$$

As before, lets compute the impedance far from the resonance frequency:

$$\frac{V_{out}}{V_{in}}(f \neq f_{LO}) = \frac{R}{2R + R_{sw}}. \tag{B.36}$$

The rejection of the filter can be computed as:

$$Rej = \frac{\frac{V_{out}}{V_{in}}(f \neq f_{LO})}{\frac{V_{out}}{V_{in}}(f_{LO})} = 1 + \beta \tag{B.37}$$

that is a function only of the number of phases and is independent from the switch on-resistance value. Since the minimum value is reduced but the rejection is not affected, the effect of the switch resistance on the band-stop N-Path filter is to shift down the whole frequency response, as shown in Fig.B.13b.

Appendix C

System Schematics

In this Appendix, the complete circuit schematic of the diversity and auxiliary receivers are reported.

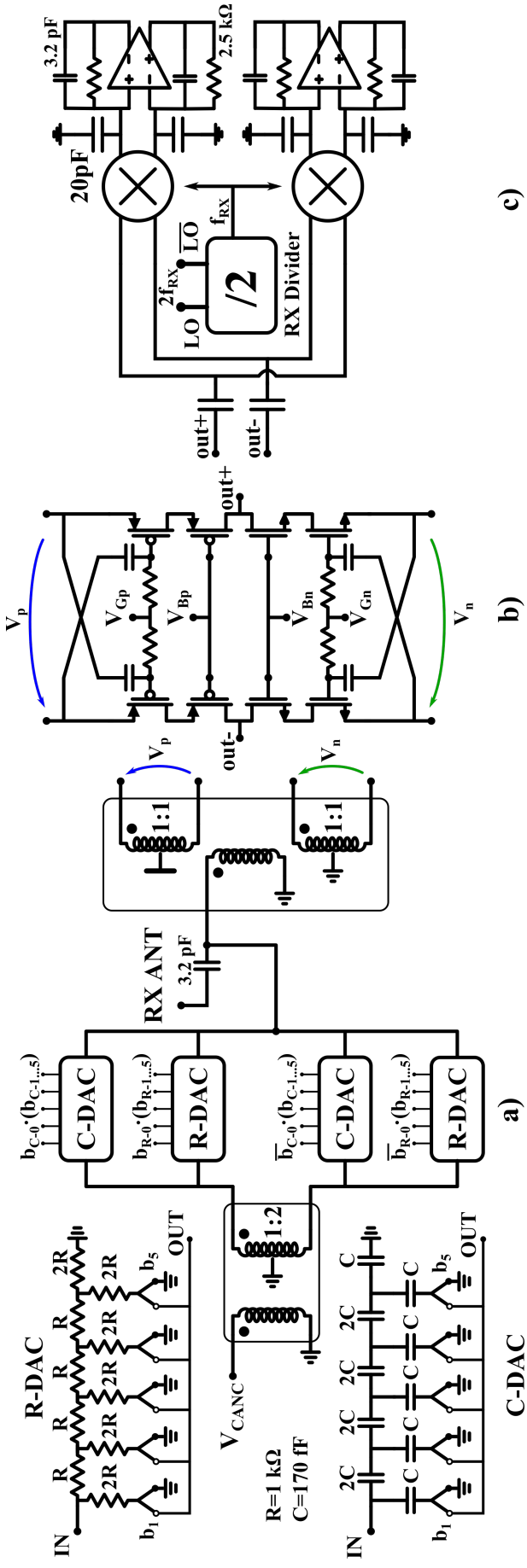

FIGURE C.1: Complete RX schematic with (a) SIC, (b) LNTA and (c) four-phases passive mixers and baseband stages ([33]©2018 IEEE).

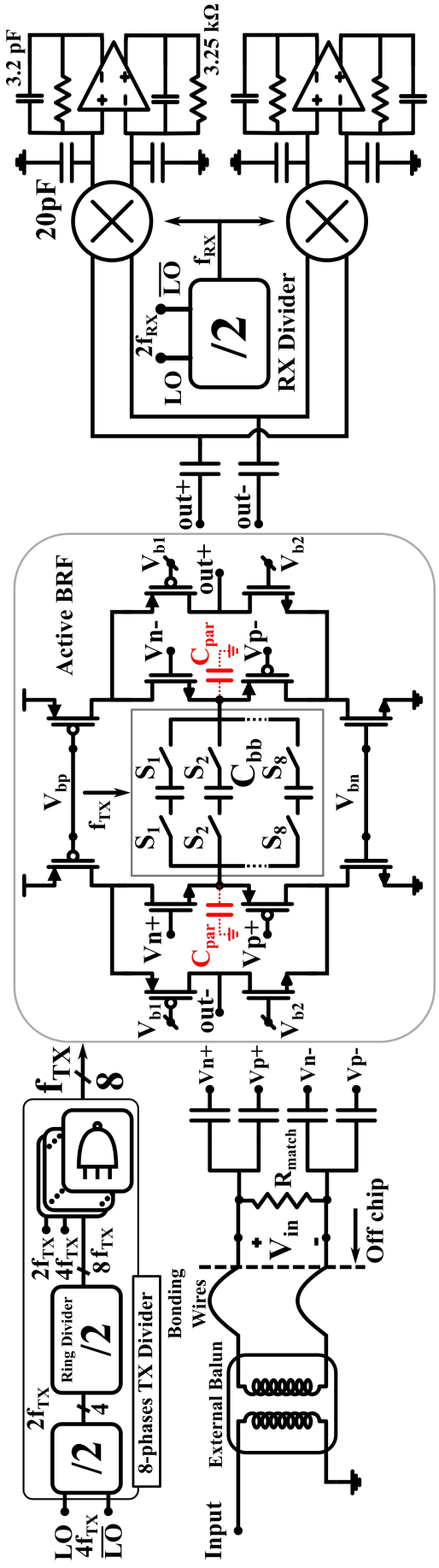

FIGURE C.2: Complete auxiliary path schematic ([33]©2018 IEEE).

Bibliography

[1] J. Winters, J. Salz, and R. Gitlin, "The capacity of wireless communication systems can be substantially increased by the use of antenna diversity," in *1st International Conference on Universal Personal Communications - ICUPC*, IEEE, 1992.

[2] TS 36.101 version 14.5.0, Release 14, "Evolved Universal Terrestrial Radio Access (E-UTRA); User Equipment (UE) Radio Transmission and Reception," tech. rep., 3GPP, 2017.

[3] B. Razavi, *RF Microelectronics*. Pearson Education (US), 2011.

[4] Stefania Sesia, Issam Toufik, Matthew Baker, *LTE, The UMTS Long Term Evolution: From Theory to Practice*. Wiley, 2009.

[5] C. kai Luo, P. S. Gudem, and J. F. Buckwalter, "A 0.4 6 GHz 17 dBm B1dB 36 dBm IIP3 Channel-Selecting Low-Noise Amplifier for SAW-Less 3G/4G FDD Diversity Receivers," *IEEE Transactions on Microwave Theory and Techniques*, vol. 64, pp. 1110–1121, apr 2016.

[6] C. kai Luo, P. S. Gudem, and J. F. Buckwalter, "A 0.2–3.6-GHz 10-dBm B1dB 29-dBm IIP3 Tunable Filter for Transmit Leakage Suppression in SAW-Less 3G/4G FDD Receivers," *IEEE Transactions on Microwave Theory and Techniques*, vol. 63, pp. 3514–3524, oct 2015.

[7] A. Ghaffari, E. A. M. Klumperink, and B. Nauta, "Tunable N-Path Notch Filters for Blocker Suppression: Modeling and Verification," *IEEE Journal of Solid-State Circuits*, vol. 48, pp. 1370–1382, jun 2013.

[8] M. N. Hasan, Q. J. Gu, and X. Liu, "Tunable Blocker-Tolerant On-Chip Radio-Frequency Front-End Filter With Dual Adaptive Transmission Zeros for Software-Defined Radio Applications," *IEEE Transactions on Microwave Theory and Techniques*, vol. 64, pp. 4419–4433, dec 2016.

[9] J. W. Park and B. Razavi, "Channel Selection at RF Using Miller Bandpass Filters," *IEEE Journal of Solid-State Circuits*, vol. 49, pp. 3063–3078, dec 2014.

[10] M. Darvishi, R. van der Zee, and B. Nauta, "Design of Active N-Path Filters," *IEEE Journal of Solid-State Circuits*, vol. 48, pp. 2962–2976, dec 2013.

[11] H. Hedayati, V. Aparin, and K. Entesari, "A +22dBm IIP3 and 3.5dB NF wideband receiver with RF and baseband blocker filtering techniques," in *2014 Symposium on VLSI Circuits Digest of Technical Papers*, IEEE, jun 2014.

[12] H. Hedayati, W.-F. A. Lau, N. Kim, V. Aparin, and K. Entesari, "A 1.8 dB NF blocker-filtering noise-canceling wideband receiver with shared TIA in 40nm CMOS," in *2014 IEEE Radio Frequency Integrated Circuits Symposium*, IEEE, jun 2014.

[13] Y. Lien, E. Klumperink, B. Tenbroek, J. Strange, and B. Nauta, "24.3 A high-linearity CMOS receiver achieving +44dBm IIP3 and +13dBm B1dB for SAW-less LTE radio," in *2017 IEEE International Solid-State Circuits Conference (ISSCC)*, IEEE, feb 2017.

[14] G. Qi, B. van Liempd, P.-I. Mak, R. P. Martins, and J. Craninckx, "A 0.7 to 1 GHz switched-LC N-Path LNA resilient to FDD-LTE self-interference at $\geq$40 MHz offset," in *2017 IEEE Radio Frequency Integrated Circuits Symposium (RFIC)*, IEEE, jun 2017.

[15] T. Zhang, A. R. Suvarna, V. Bhagavatula, and J. C. Rudell, "An Integrated CMOS Passive Self-Interference Mitigation Technique for FDD Radios," *IEEE Journal of Solid-State Circuits*, vol. 50, pp. 1176–1188, may 2015.

[16] H. Kim, S. Woo, S. Jung, and K.-H. Lee, "A CMOS Transmitter Leakage Canceller for WCDMA Applications," *IEEE Transactions on Microwave Theory and Techniques*, vol. 61, pp. 3373–3380, sep 2013.

[17] S. Tijani and D. Manstretta, "A SAW-less receiver front-end with low power active self-interference canceler," in *2015 IEEE International Conference on Electronics, Circuits, and Systems (ICECS)*, IEEE, dec 2015.

[18] J. Zhou, T.-H. Chuang, T. Dinc, and H. Krishnaswamy, "An Integrated Wideband Self-Interference Cancellation in the RF Domain for FDD and Full-Duplex Wireless," *IEEE Journal of Solid-State Circuits*, vol. 50, pp. 3015–3031, dec 2015.

[19] L. Calderin, S. Ramakrishnan, A. Puglielli, E. Alon, B. Nikolic, and A. M. Niknejad, "Analysis and Design of Integrated Active Cancellation Transceiver for Frequency Division Duplex Systems," *IEEE Journal of Solid-State Circuits*, vol. 52, pp. 2038–2054, aug 2017.

[20] T. Zhang, A. Najafi, C. Su, and J. C. Rudell, " A 1.7-to-2.2GHz full-duplex transceiver system with >50dB self-interference cancellation over 42MHz bandwidth," in *2017 IEEE International Solid-State Circuits Conference (ISSCC)*, IEEE, feb 2017.

[21] T. Zhang, C. Su, A. Najafi, and J. C. Rudell, "Wideband Dual-Injection Path Self-Interference Cancellation Architecture for Full-Duplex Transceivers," *IEEE Journal of Solid-State Circuits*, vol. 53, pp. 1563–1576, jun 2018.

[22] S. H. Abdelhalem, P. S. Gudem, and L. E. Larson, "Tunable CMOS Integrated Duplexer With Antenna Impedance Tracking and High Isolation in the Transmit and Receive Bands," *IEEE Transactions on Microwave Theory and Techniques*, vol. 62, pp. 2092–2104, sep 2014.

[23] M. Mikhemar, H. Darabi, and A. Abidi, "A tunable integrated duplexer with 50dB isolation in 40nm CMOS," in *2009 IEEE International Solid-State Circuits Conference - Digest of Technical Papers*, IEEE, feb 2009.

[24] I. Fabiano, M. Ramella, D. Manstretta, and R. Castello, "A 25-dBm IIP3 1.7-2.1 GHz FDD Receiver Front End With Integrated Hybrid Transformer in 28-nm CMOS," *IEEE Transactions on Microwave Theory and Techniques*, vol. 65, pp. 4677–4688, nov 2017.

[25] B. van Liempd, B. Hershberg, B. Debaillie, P. Wambacq, and J. Craninckx, "An electrical-balance duplexer for in-band full-duplex with <-85dBm in-band distortion at +10dBm TX-power," in *ESSCIRC Conference 2015 - 41st European Solid-State Circuits Conference (ESSCIRC)*, IEEE, sep 2015.

[26] B. van Liempd, B. Hershberg, S. Ariumi, K. Raczkowski, K.-F. Bink, U. Karthaus, E. Martens, P. Wambacq, and J. Craninckx, "A +70-dBm IIP3 Electrical-Balance Duplexer for Highly Integrated Tunable Front-Ends," *IEEE Transactions on Microwave Theory and Techniques*, vol. 64, pp. 4274–4286, dec 2016.

[27] G. Castellano, D. Montanari, D. D. Caro, D. Manstretta, and A. G. M. Strollo, "An Efficient Digital Background Control for Hybrid Transformer-Based Receivers," *IEEE Transactions on Circuits and Systems I: Regular Papers*, vol. 64, pp. 3068–3080, dec 2017.

[28] E. Roverato, M. Kosunen, K. Cornelissens, S. Vatti, P. Stynen, K. Bertrand, T. Korhonen, H. Samsom, P. Vandenameele, and J. Ryynanen, "All-Digital LTE SAW-Less Transmitter With DSP-Based Programming of RX-Band Noise," *IEEE Journal of Solid-State Circuits*, vol. 52, pp. 3434–3445, dec 2017.

[29] E. Roverato, M. Kosunen, J. Lemberg, K. Stadius, and J. Ryynanen, "RX-Band Noise Reduction in All-Digital Transmitters With Configurable Spectral Shaping of Quantization and Mismatch Errors," *IEEE Transactions on Circuits and Systems I: Regular Papers*, vol. 61, pp. 3256–3265, nov 2014.

[30] R. Bhat, J. Zhou, and H. Krishnaswamy, "Wideband Mixed-Domain Multi-Tap Finite-Impulse Response Filtering of Out-of-Band Noise Floor in Watt-Class Digital Transmitters," *IEEE Journal of Solid-State Circuits*, vol. 52, pp. 3405–3420, dec 2017.

[31] D. Montanari, L. Silvestri, M. Bozzi, and D. Manstretta, "Antenna coupling and self-interference cancellation bandwidth in SAW-less diversity receivers," in *2016 46th European Microwave Conference (EuMC)*, IEEE, oct 2016.

[32] C. Rowell and R. Murch, "A capacitively loaded PIFA for compact mobile telephone handsets," *IEEE Transactions on Antennas and Propagation*, vol. 45, pp. 837–842, may 1997.

[33] D. Montanari, G. Castellano, E. Kargaran, G. Pini, S. Tijani, D. D. Caro, A. G. M. Strollo, D. Manstretta, and R. Castello, "An FDD Wireless Diversity Receiver With Transmitter Leakage Cancellation in Transmit and Receive Bands," *IEEE Journal of Solid-State Circuits*, vol. 53, pp. 1945–1959, jul 2018.

[34] G. Pini, D. Manstretta, and R. Castello, "Analysis and Design of a 20-MHz Bandwidth, 50.5-dBm OOB-IIP3, and 5.4-mW TIA for SAW-Less Receivers," *IEEE Journal of Solid-State Circuits*, vol. 53, pp. 1468–1480, may 2018.

[35] T. Zhang, Y. Chen, C. Huang, and J. C. Rudell, "A low-noise reconfigurable full-duplex front-end with self-interference cancellation and harmonic-rejection power amplifier for low power radio applications," in *ESSCIRC 2017 - 43rd IEEE European Solid State Circuits Conference*, IEEE, sep 2017.

[36] N. Codega, P. Rossi, A. Pirola, A. Liscidini, and R. Castello, "A Current-Mode, Low Out-of-Band Noise LTE Transmitter With a Class-A/B Power Mixer," *IEEE Journal of Solid-State Circuits*, vol. 49, pp. 1627–1638, jul 2014.

[37] M. Ramella, I. Fabiano, D. Manstretta, and R. Castello, "A 1.7-2.1GHz +23dBm TX power compatible blocker tolerant FDD receiver with integrated duplexer in 28nm CMOS," in *2015 IEEE Asian Solid-State Circuits Conference (A-SSCC)*, IEEE, nov 2015.

[38] M. Darvishi, *Active N-path Filters: Theory and Design.* PhD thesis, University of Twente, 2013.

[39] S. O. Haykin, *Adaptive Filter Theory (5th Edition)*. Pearson, 2013.

[40] T. Tapen, Z. Boynton, H. Yuksel, A. Apsel, and A. Molnar, "The Impact of LO Phase Noise in N-Path Filters," *IEEE Transactions on Circuits and Systems I: Regular Papers*, vol. 65, pp. 1481–1494, may 2018.

[41] M. Garampazzi, P. M. Mendes, N. Codega, D. Manstretta, and R. Castello, "Analysis and Design of a 195.6 dBc/Hz Peak FoM P-N Class-B Oscillator With Transformer-Based Tail Filtering," *IEEE Journal of Solid-State Circuits*, vol. 50, pp. 1657–1668, jul 2015.

[42] L. Laughlin, M. A. Beach, K. A. Morris, and J. L. Haine, "Electrical balance duplexing for small form factor realization of in-band full duplex," *IEEE Communications Magazine*, vol. 53, pp. 102–110, may 2015.

[43] X. Liu, A. Nejdel, M. Palm, L. Sundstrom, M. Tormanen, H. Sjoland, and P. Andreani, "A 65 nm CMOS Wideband Radio Receiver With $\Delta\Sigma$-Based A/D-Converting Channel-Select Filters," *IEEE Journal of Solid-State Circuits*, vol. 51, pp. 1566–1578, jul 2016.

[44] J. Zhou, A. Chakrabarti, P. R. Kinget, and H. Krishnaswamy, "Low-Noise Active Cancellation of Transmitter Leakage and Transmitter Noise in Broadband Wireless Receivers for FDD/Co-Existence," *IEEE Journal of Solid-State Circuits*, vol. 49, pp. 3046–3062, dec 2014.

[45] D.-J. van den Broek, E. A. M. Klumperink, and B. Nauta, "An In-Band Full-Duplex Radio Receiver With a Passive Vector Modulator Downmixer for Self-Interference Cancellation," *IEEE Journal of Solid-State Circuits*, vol. 50, pp. 3003–3014, dec 2015.

[46] L. E. Franks and I. W. Sandberg, "An Alternative Approach to the Realization of Network Transfer Functions: The N-Path Filter," *Bell System Technical Journal*, vol. 39, pp. 1321–1350, sep 1960.

[47] A Ghaffari and E A M Klumperink and M C M Soer and B Nauta, "Tunable High-Q N-Path Band-Pass Filters: Modeling and Verification," *IEEE Journal of Solid-State Circuits*, vol. 46, pp. 998–1010, may 2011.